Towards High-Energy Rechargeable Magnesium Batteries and Battery Analytics for Electric Aviation

Robert C. Massé

A dissertation

submitted in partial fulfillment of the

requirements for the degree of

Doctor of Philosophy

University of Washington

2021

Reading Committee:

Guozhong Cao, Chair

Dwayne Arola

Jihui Yang

Program Authorized to Offer Degree:

Materials Science and Engineering Department

University of Washington

Abstract

Towards High-Energy Rechargeable Magnesium Batteries
and
Battery Analytics for Electric Aviation

Robert C. Massé

Chair of the Supervisory Committee:

Guozhong Cao

Materials Science and Engineering Department

Since its commercialization in 1991, the rechargeable Li-ion battery has revolutionized how we live, work, and communicate. Further, rapidly declining costs have enabled the ongoing electrification of heavy industry, from automotive to power utilities and even aviation. Despite these important advances, reaching the targets required to minimize the effects of climate change requires improvements to battery technology across all levels of research and development – from basic materials chemistry to optimizations in manufacturing and operations in the field.

This work represents a cross-cutting effort that spans the breadth of this range. In the experimental portion, the fundamental electrochemistry of magnesium was studied in the context of developing new positive and negative electrode materials for magnesium batteries. In particular, we show how considering the system as two interfaces (cathode-electrolyte and

anode-electrolyte) rather than three components (cathode, anode, and electrolyte) helps explain some of the nuances of magnesium compared to lithium electrochemistry. In the second part of this work, we address applied problems in the growing field of battery data science and analytics. We develop software tools and models for industry-relevant problems in basic battery data management, cell lifetime forecasting and validation, and specific applications in electric aviation.

Magnesium batteries represent a compelling candidate for the next generation of battery chemistries. It offers the prospect of safer operation at lower costs to manufacture and ~60% greater energy density compared to Li-ion batteries. However, many problems at the anode-electrolyte and cathode-electrolyte interfaces need to be resolved. Many electrolytes passivate magnesium metal and are oxidized at the cathode, and the nature of the kinetics (both reaction and diffusion) is unclear. In the two main prongs of this section of this work we propose 1) a coating that provides kinetic stability to the anode, and 2) an electrochemical protocol for studying magnesium cathode materials with greater clarity and reliability. Together we believe these approaches may be married to each other to develop a robust, high-energy magnesium battery based on a magnesium metal anode and a metal oxide cathode.

We also explore battery data science as it applies to the new electric aviation industry. There are three main contributions. First, we report a user-friendly software environment for battery data science. It is designed to streamline data management, data cleaning, and data analysis to help bridge the gap between the domain expertise of most battery scientists and the tools needed as the field becomes increasingly data intensive. Second, we use a neural network model to extend state-of-the-art cell cycle life predictions to include a wider range of datasets and testing conditions, such as C-rate, cell chemistry, and temperature. Third, we train an outlier detection

algorithm to rapidly identify weak cell blocks in an electric aircraft battery pack. This is significant in that identifying weak cells helps determine the remaining useful life in a battery system, which is of utmost importance for flight operators. Each of these constitute pieces of an effort that is oriented toward developing standard operating procedures for battery safety, performance, and maintenance for electric aviation.

Table of Contents

List of Figures

List of Tables

Chapter 1. Introduction

1.1. The Need for Energy Storage

Energy storage is the bottleneck that limits technologies at all scales. From biomedical implants[1] and portable electronics[2] to electric vehicles[3–5] and grid-scale storage of renewables,[6–8] battery storage is often the biggest cost and design limitation.

Future battery advances and economies of scale will help scrub CO_2 emissions from transportation and the grid. Economical energy storage lets battery-powered electric vehicles replace internal combustion engines in the transportation sector, which now accounts for the plurality of CO_2 emissions in the USA (~34% through March 2016).[9] Despite concerns about coal powering electric vehicles,[10,11] better batteries will in fact compound the environmental benefits as storage helps renewables supplant coal and other fossil-fuel power plants.[12,13]

For grid-scale applications, the benefits of adding storage are many and well documented.[14,15] Beyond increased penetration of intermittent renewable generation, batteries' fast response times (seconds) and relatively long discharge time (hours) make them viable for applications across many time scales.[16] Storage helps with frequency regulation, which balances generation and load in real-time and increases grid reliability.[17] On the scale of minutes and hours, storage also supplies previously stored power during times of high demand and mitigates the need for additional installed capacity on the grid. Over the long term, reducing the load allows utilities to avoid the cost of new substations and transmission lines.[18] Not all applications are mutually compatible,[14] but they can still be combined to match the needs of different actors and locations and fundamentally transform the grid.[19–22]

The relevant metric for life-cycle analyses of these larger-scale applications is the cost. The demands on energy, power, lifetime and safety characteristics will vary between storage applications, but the battery system will not be installed in the absence of a strong value

proposition. A sophisticated technoeconomic analysis has many considerations to address.[23–27] However, as a reasonable approximation, the levelized cost of electricity (*LCOE*, in $/kWh-cycle) is as follows:[28]

$$LCOE = \frac{C}{E \cdot n \cdot \eta} \tag{1}$$

Here, C is the total cost of the storage system, including both capital and operating costs, per unit mass (or volume), E is the energy density per unit mass (or volume) of the device at the pack level, n is the lifetime of the battery measured in cycles and η is the roundtrip energy efficiency. This formula clarifies the main goals of battery scientists and engineers. Cost is minimized with design choices that favor abundant materials and scalable processing techniques. Energy density increases with higher-voltage and -capacity materials, and more efficient cell architectures. Incident-free long life is achieved with materials that are mechanically, thermally and electrochemically stable, and aided by battery management systems. The overall energy efficiency is determined by both the behavior of the redox-active material and the power electronics of the battery pack itself. Finding acceptable tradeoffs between energy, power, cost, and safety is the herculean challenge for the battery community.[29]

1.2. Battery Fundamentals

Batteries convert chemical potential energy into usable electrical energy. A battery has three main components: the positive electrode (cathode), the negative electrode (anode) and the electrolyte in between (Figure 1). The battery is charged or used to provide power when the electrodes are connected via an external circuit. The electrolyte is an electronically insulating but ionically conductive medium. It transports the reactant between the two electrodes without short circuiting the battery. Many different configurations are possible using these three building blocks.

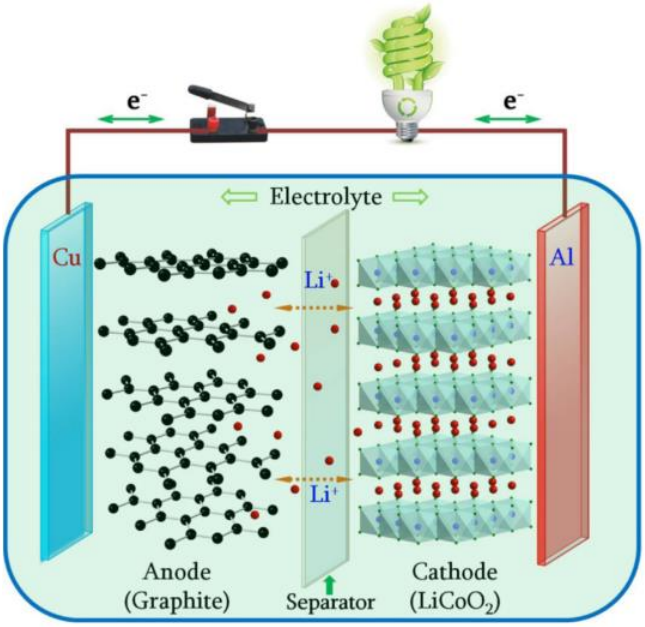

Figure 1. Schematic representation of a Li-ion battery with a layered cobalt oxide cathode and graphitic carbon anode as active materials. Adapted from Ref. [30].

In Li-ion batteries, the electrodes are often porous composites that contain some combination of the electroactive material and a carbon additive (to boost electronic conductivity in the electrode) connected with a polymer binder. Slurries of these composites are coated onto copper or aluminum foil substrates to provide physical support during processing and provide an electronically conductive pathway to the external circuit. The choice of metal is determined by economics and electrochemical stability in the highly oxidizing (reducing) environment near the cathode (anode). The electrolyte is typically an organic carbonate solvent containing a lithium salt, most commonly $LiPF_6$. A mixture of different carbonates is needed to achieve the appropriate combination of properties (low viscosity, high boiling point, etc.), and additives like vinyl carbonate are used to improve long-term cycling performance.[31,32] A polymer membrane separator insulates the two electrodes from each other when they are sandwiched together during assembly.[33]

Discharge corresponds to reduction of the electroactive species of the cathode material and intercalation of Li^+ into available sites in the host lattice. The driving force for intercalation during discharge is the spontaneous redox reaction at the electrode surface. Electroneutrality is maintained by the flow of electrons from the negatively charged anode to the positive cathode via the external circuit. When the battery is recharged, an external load reverses the flow of ions and electrons back into the negative electrode. The astute electrochemist will notice that reversing the reaction means that the positive electrode is now the anode and the negative electrode is the cathode, but battery researchers will often call the positive electrode the cathode regardless of the mode of operation.

Despite tremendous R&D efforts and investments,[34] most battery progress has been made at the manufacturing level. For Li-ion batteries, only five practical cathode materials and two anode materials have been commercialized to date (

Table **1**).[35]

Table 1. Rechargeable Li-ion battery intercalation electrode materials. Adapted from ref. [35–38].

	Material	Structure	Average Voltage (V vs. Li)	Practical Capacity (mAh g^{-1})	Date First Reported	Reference
Cathodes	$LiCoO_2$	Layered	~3.9	~140	1980	[39]
	$LiMn_2O_4$	Spinel	~4.1	~120	1983	[40]
	$LiFePO_4$	Olivine	~3.45	~160	1997	[41]
	$LiNi_{1/3}Mn_{1/3}Co_{1/3}O_2$	Layered	~3.8	~200	2001	[42]

	$LiNi_{0.8}Co_{0.15}Al_{0.05}O_2$	Layered	~3.8	~200	2003	[43]
Anodes	Graphite (LiC_6)	Layered	~0.1	~360	1983	[44]
	$Li_4Ti_5O_{12}$	Spinel	~1.5	~175	1994	[45]

In the absence of a transformational breakthrough, Li-ion technology was not projected to exceed ~300 Wh kg^{-1}.[46] Recently, CATL has been able to drive up the energy density to 304 Wh kg^{-1} with a pouch cell configuration using NMC 811 (that is, a cathode with 80% nickel and 10% of manganese and cobalt as the active material) and adding up to ~10% silicon into the graphite anode,[47] but the industry is still reaching the limits of conventional advanced Li-ion technology. Faced with diminishing returns on Li-ion materials research, alternative alkali intercalation chemistries have received renewed attention.[48–50] Sodium ion batteries are the most mature out of the set of sodium, magnesium, potassium, or calcium batteries.[51] The main advantages of Na-ion batteries are similar (but not identical) electrochemistry and very low cost compared to Li-ion batteries. However, the energy density is generally comparable or lower than Li-ion, plus the larger Na^+ tends to do more damage to the host lattice during long-term cycling.[50]

1.3. Magnesium Batteries and Challenges

Multivalent intercalation batteries are another compelling route to higher energy densities, and one of the main thrusts of the Joint Center for Energy Storage Research (JCESR).[34] The divalent alkaline earth metals magnesium compares favorably with lithium and sodium in a few key dimensions (Table 2).[48,49] Research on magnesium batteries is still in the exploratory phase,

although interest is rapidly increasing. In spite of pioneering work by Gregory *et al.*[52] studies on magnesium batteries were sparse, especially after the commercialization of Li-ion batteries in the early 1990's. Aurbach *et al.* have since contributed several important breakthroughs, and in 2000 demonstrated a full cell magnesium battery that was capable of thousands of cycles.[53–55]

The most promising advantage for magnesium was that the metal plated without forming dendrites.[56–58] This entirely circumvents the fatal dendrite problem in lithium metal, meaning magnesium could safely be used as an extremely high-capacity battery anode.

Handling, machining, and disposal are easier for magnesium since it does not react as violently with air or water. High earth abundance also makes magnesium less expensive than lithium materials in the hypothetical magnesium battery supply chain. In addition, its ionic radius is comparable to lithium, meaning no additional mechanical strain is placed on the host lattice during insertion and removal (unlike sodium, for example). Considering these factors, we can envision a net gain in energy density at a reduced cost to operate and manufacture.

Table 2. Comparison of characteristics and electrochemical properties of prospective alkaline (earth)-ion batteries.[38,50]

Parameters	Valance	Cationic radius (Å)	Atomic weight (g mol^{-1})	E (V vs. SHE)	Specific capacity (mAh g^{-1})	Volumetric capacity (mAh cm^{-3})
Lithium	+1	0.76	6.94	-3.04	3862	2062
Sodium	+1	1.02	22.99	-2.71	1166	1128
Magnesium	+2	0.72	24.31	-2.37	2205	3833

Despite the advantages listed above, magnesium batteries have many challenges to overcome. The difference chemical and electrochemical properties of magnesium relative to lithium leads to failure modes that are both more numerous and more complicated compared well-understood lithium-ion batteries. These include low voltage stability of electrolytes at the

positive electrode, inefficient plating and stripping of magnesium at the negative electrode, and other incompatibilities between different cell components such as corrosion of stainless steel and total passivation of magnesium metal in most electrolytes.[50] To make matters worse, it has recently been found that magnesium will in fact form dendrites under conditions where the rate of deposition is sufficiently high and self-diffusion is low.[59] As such, magnesium is not a "platform technology" like Li-ion (where different cathodes, electrolytes, and anodes can be swapped interchangeably without compromising performance), and the electrochemistry of magnesium does not benefit from much direct carry-over from Li-ion research. We believe this has generated misunderstandings that this work attempts to overcome.

Instead of focusing on 1) the anode, 2) the electrolyte, and 3) the cathode individually, we propose here that analyzing the 1) anode-electrolyte and 2) cathode-electrolyte interfaces is crucial for understanding magnesium battery performance. Thinking more holistically about the interfaces generates more significant insights to address the two biggest problems for magnesium batteries: passivation of the anode and the dearth of high-energy cathodes.

1.5. Battery Data Science and Challenges

As batteries become increasingly integral to energy and mobility, they are deployed in more and more demanding use cases. Previously, planned obsolescence meant that batteries could get away with being "good enough" for earlier generations of consumer electronics. However, understanding health and performance is no longer an afterthought. Achieving long safe operating lifetimes is mission critical for the business models of up-and-coming materials startups, cell OEMs, and downstream customers building packs for automotive and other demanding environments with long-lived use cases.

Reliable data is a necessity for engineers and management to make informed decisions during battery product development, operations, or maintenance at any point in the battery value

chain (Figure 2). Unfortunately, this is confounded by the wide variety of data that is generated, from electrochemical properties to real-world performance in cells or modules or pack-level applications. Unlike other solid-state electronics, such as solar cells or integrated circuits, batteries are dynamic nonlinear systems. Their performance varies with cell chemistry, temperature, humidity, formation protocol, duty cycle, battery management system, and other variables that may be hidden from the battery operator. Nevertheless, cell OEMs only supply specification sheets that show battery performance under a narrow set of idealized lab test conditions. This leaves systems integrators and operators with significant risk exposure when the battery is ultimately deployed "in the wild." Several high-profile cases of battery failure have made headlines, most recently the 2021 recall of the Chevy Bolt, which cost General Motors and its cell supplier LG Energy Solutions an estimated $2 billion.[60] The fact that two of the most experienced automotive and battery cell manufacturers still have unsolved quality assurance problems is a testament to the urgency and difficulty of this challenge.

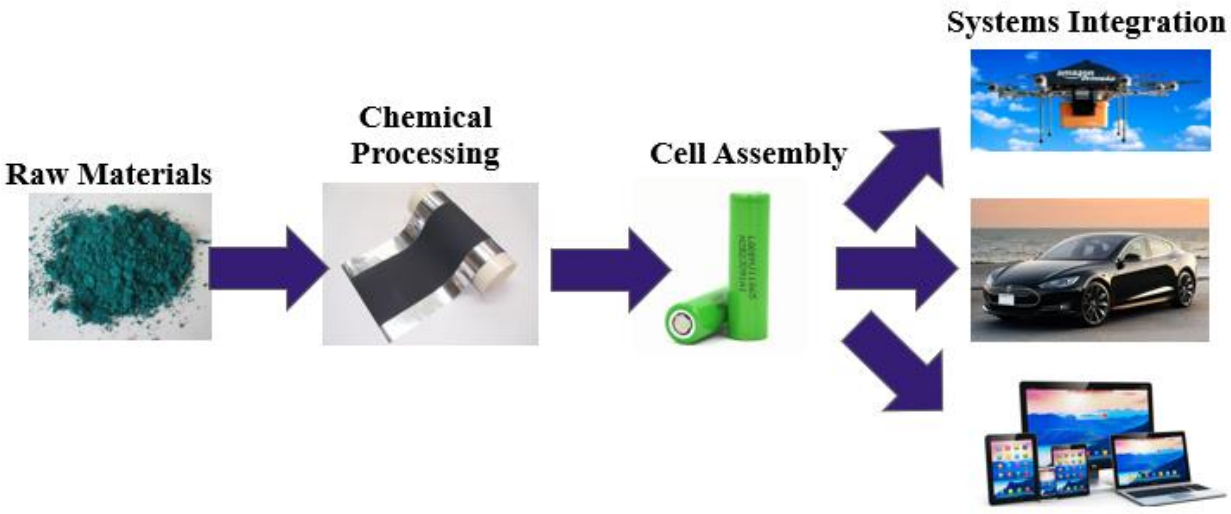

Figure 2. The battery value chain spans mining of raw chemical materials, processing and refining, cell manufacturing, and integration into packs for end-use applications.

An introduction to battery data science and machine learning as it applies to electric aviation is provided in Chapter 5. Afterward, we discuss progress made in three distinct tracks.

In Chapter 6 we report a user-friendly environment for battery data science. There is a wide gap between the tools and training for battery scientists and their increasingly data-intensive jobs. Especially for experimentalists without experience with battery modelling or simulation software, engineers are often used to fragile legacy software for routine data analysis tasks. On top of this, there is a dearth of common standards and data practices, owing to the wide range of R&D goals, heterogenous data streams, and domains of expertise from one company or research group to another.[61] The platform is designed to add new tools to the battery engineer's toolkit by collating disparate data and metadata sources into a standardized format for post-processing. Here the goal is to streamline data cleaning and provide an environment that services the pluralistic needs of the battery community. This includes basic data visualization for monitoring and analysis, a Python API for modelling and machine learning, and dashboards for high-level project management.

In Chapter 7, we report progress on cell-level lifetime forecasting using a neural network (NN) machine learning model. This data-driven approach has several significant features. First, it extends state-of-the-art battery lifetime prediction models to encompass a wider range of temperatures, C-rates, and chemistries. This makes it suitable for the task of cell validation and acceptance testing, allowing the customers of cell OEMs to validate new cells faster and improve quality control processes. The NN architecture is designed to accommodate both new datasets and new features, meaning that it will improve with time as more datasets are made publicly available and as new domain-specific diagnostic features are discovered and engineered. Additionally, we show that data from different labs and different chemistries (namely NCA,

LCO, and NMC) all perform well, which suggests that a common degradation mode is shared across all three chemistries – loss of active lithium on the graphitic anode side of the cell. Future work is ongoing to incorporate uncertainty quantification into this model. This will allow us to not only make our models more scientifically rigorous but also give decision makers the ability to make rational tradeoffs between e.g. maximizing the accuracy of the prediction and minimizing the testing time required to reach a product decision.

In Chapter 8 we report on preliminary results towards online fuel-gauging for electric aircraft. Specifically, an algorithm for identifying weak cell blocks in a battery pack is developed. Since overall battery system performance is limited to the weakest cells in the battery pack, finding and tracking these cells is an important first step in developing standard operating procedures for fuel gauging that will meet Federal Aviation Administration (FAA) requirements. The outlier detection algorithm developed takes the first five minutes of flight test data and identifies the weakest cell blocks with 89% accuracy.

Finally in Chapter 9, we conclude by outlining future work towards developing standard operating procedures for battery safety, performance, and maintenance for electric aviation. Overall conclusions for this thesis are summarized in Chapter 10.

Chapter 2. Kinetic Surface Control for Improved Magnesium-Electrolyte Interfaces for Magnesium-ion Batteries

2.1. Introduction

Magnesium metal anodes are incompatible with many electrolytes. Conventional electrolytes (e.g. $Mg(ClO_4)_2$ dissolved in organic solvents) are reduced by Mg and form insoluble passivation layers on the Mg metal surface.[62,63] Unlike the solid-electrolyte interphase (SEI) layer in Li-ion batteries, the Mg passivation layer blocks transport of both ions and electrons and makes the electrochemical deposition/stripping of Mg impossible.[55,64] On the other hand, the electrolytes that allow for reversible plating and stripping of Mg at the metal anode surface (Grignard reagents and other organohaloaluminate electrolytes) suffer from poor stability at voltages beyond ~2V (hereafter reported versus the Mg/Mg^{2+} redox couple unless otherwise indicated).[53,65–69] More recently, a class of electrolytes with stabilities beyond 3 V and reversible plating and stripping have been developed, but require complicated organic syntheses.[70–73]

The anode-electrolyte interface governs the performance and longevity of the cell and has been the subject of many studies.[62,74–79] As early as 2003, it was believed that a stable "passivation layer" develops on fresh magnesium metal foil submerged in solutions of THF and $Mg(AlEtBuCl_2)_2$ – an electrolyte that supports Mg stripping and plating.[80] The authors suggest the layer contained physically adsorbed molecules rather than ionic species on the Mg surface. More recently, the influence of adsorbed Mg_x-Cl_y species were identified as key electrolyte components that benefit reversible plating of magnesium because of their preferential adsorption and low energies required to remove chloride ligands from Mg^{2+}.[81,82] In fact, adding $MgCl_2$ greatly improves the performance of electrolytes by shifting the equilibrium concentration of the Mg_x-Cl_y species and greatly reducing the overpotential for stripping and plating.[83–85] However, this strategy is limited for two reasons. The volatile solvent has safety limitations because of its

low boiling point (66°C for THF), while chloride-containing electrolytes are corrosive towards common battery components such as stainless steel.[55,86,87]

While commercially practical electrolytes may not be a reality yet, researchers have made good progress increasing the thermodynamic stability of the electrolyte in the last twenty years.[88–90] Notably, a recent trend to reduce chlorine content in electrolytes has enabled the discovery of noncorrosive electrolytes with good conductivity (>1 mS cm^{-1}), relatively efficient Mg dissolution/deposition (>98% Coulombic efficiency) and anodic stability well beyond 3 V.[72,91,92] However, these novel electrolytes often require complicated procedures and dangerous chemicals that are best left to synthetic organometallic chemists.[93]

Here we propose an alternative path forward that uses kinetic control of the anode-electrolyte interface.[94] By passivating the Mg metal surface with fluorine, we developed what was among the first Mg^{2+}-conductive solid-electrolyte interphase (SEI) layers.

The surface coating strategy has become increasingly attractive, and others have demonstrated similar coatings and interfaces that conduct Mg^{2+} ions. These include coatings based on tin,[95] germanium chloride,[96] lithium borate salts,[97] iodine,[78] and polyacrylonitrile,[77] among others, which enabled superior reversible magnesium electrochemistry in electrolytes that are otherwise passivating. This strategy avoids the complication of time-consuming syntheses and provides a path toward non-corrosive electrolytes based on simple salts and solvents that simultaneously allow for Mg^{2+} transport.

Surface modification of fluorides have been previously used to prevent electrolyte decomposition on the surface of electrode materials and enhance the cyclic stability of the Li-ion batteries.[98,99] In Li-ion batteries, the reduction products that form the SEI layer on the surface of the electrode materials has enormous influence on the electrochemical behavior of the

batteries.[100–102] The interphase layers are complex, often consist of nanoparticles or a mixture of nanocrystallites and amorphous material so that there are abundant grain boundaries and significant variations to the local chemical composition that permit ionic transportation for the electrochemical reaction. The morphology and structure (thickness, composition, and size) of the SEI films can be turned using electrolyte additives like vinylene carbonate,[103,104] fluoroethylene carbonate,[105] vinyl ethylene carbonate,[106] propane sultone[107], prop-1-ene-1,3-sultone.[101,108] These additives are preferentially decomposed to form an insoluble solid product that covers the electrode surface. These films consume some of the lithium inventory but inhibits further reaction with the nonaqueous liquid electrolytes.

It is known that inorganic fluorides such as lithium fluoride (LiF), sodium fluoride (NaF), and magnesium fluoride (MgF_2) in their bulk states are insulators and hinder the transport of ions. However, researchers have nevertheless demonstrated that ionic transportation is possible through fluoride or fluorinated interphases. LiF artificial interphases can protect the metallic anode from the side reaction and suppress dendrite growth.[109,110] Fluorinated interphases have been known to play an important role in electrode protection.[111,112]

Magnesium fluoride (MgF_2) has been widely used in various optical thin films and multilayer photonic crystals because of its low absorption, wide bandgap, high hardness and good corrosion resistance.[113] In the context of magnesium batteries, the Aurbach group has argued that MgF_2 will be passivating at levels of surface coverage as low as 1%.[62,63] Using first-principles calculations, Chen *et al.* evaluated a wide variety of potential coating materials.[114] They predicted that MgF_2 would be thermodynamically stable as a coating material, but reported that the barrier for Mg transport would be too high to be of practical use (>1.1 eV).[115] On the other hand, Matsui *et al.*[116] found that surface MgF_2 did not inhibit the performance of a Mg_3Bi_2

intermetallic composite anode, suggesting that this layer does not necessarily turn off reversible electrochemistry.

In Li-ion batteries, MgF_2 has also been found to benefit the performance of electrode materials. For example, MgF_2-coated $LiCoO_2$ composite were developed and exhibited higher rate capability and cycling stability compared to the uncoated $LiCoO_2$.[113,117,118] In these reports the MgF_2 layer reduced side reactions with electrolyte and aided the transport of Li^+ across the electrolyte-$LiCoO_2$ interface. This combined evidence suggests the MgF_2 layer is an ionic conductor but an electronic insulator. This protective layer inhibits the decomposition of the electrolyte in magnesium systems, and more importantly, allow for Mg^{2+} transport in this protective layer.

In this work, we develop a chemically inert MgF_2 layer to improve the compatibility of the Mg with the electrolyte. Even with its high specific surface area, this passivation layer protects electrolytes from decomposition on the Mg surface. Our results on the anode-side of the Mg battery are elegant example for optimizing the surface (electro)chemistry of the magnesium metal-electrolyte interface.

2.2. Methods

2.2.1. Materials synthesis

The Bi cathode materials were synthesized by a solvothermal method reported previously.[119] In a typical procedure, 0.466 g Bi_2O_3 was added into 30 ml pure ethylene glycol (EG) while stirring with a magnetic stirrer for 30 min at room temperature. The mixture was then transferred into a stainless-steel autoclave with a Teflon liner and kept at 200 ℃ for 12 h. The black precipitate was collected and washed several times by centrifugation with diluted HCl solution and deionized water after the autoclave was cooled down, and then dried at 80 ℃ overnight.

2.2.2. Preparation of MgF_2 modified Mg foil

To prepare fresh Mg foil, commercial Mg foils were immersed into 0.1 M HCl solution for 2 min until the surface oxide layer was removed, then washed with THF three times and dried in vacuum oven at room temperature. Then the Mg foils were transferred into glovebox and mechanically polished with sandpaper (2000 grit) and wiped with THF prior to use. MgF_2 modified Mg foil were prepared by reacting hydrogen fluoride and metallic fresh Mg. The fresh Mg foils were immersed into 0.2 M hydrofluoric acid solution and sonicated for 5 min at room temperature to obtain the MgF_2 layer. Then, the Mg foils were washed with THF and dried in vacuum oven at room temperature and transferred into the glovebox.

2.2.3. Materials Characterization

The crystal structure of the Bi_2O_3 starting material and Bi nanowires were determined by XRD (D8 Bruker X-ray diffractometer with Cu-Kα radiation (λ=1.5418 Å)) between 10° and 80° (2θ). Energy dispersive X-ray spectroscopy (EDS) was used to characterize the Mg foil surface. The morphology for all materials was observed with SEM (JEOL, JSM-7000F). The specific surface area and pore characteristics were determined by multipoint Brunauer-Emmett-Teller (BET) and Barrett-Joyner-Halenda (BJH) desorption analyses to estimate the surface area and pore size respectively.

2.2.4. Electrochemical Measurements

The electrode of Bi was prepared by coating a mixture of 70 wt. % of active material and 15 wt. % of super-p as conducting agent and 15 wt. % of polyvinylidene fluoride (PVdF) as binder onto an Al current collector. 2032- or 2025-type coin cells were assembled in an Ar-filled MBraun glove box using the prepared electrodes as positive electrodes, Mg foils as negative electrodes and microporous membrane (Celgard 2400) as the separators. The “all phenyl” complex (APC) electrolyte that comprising PhMgCl and AlCl3 in a ratio of 2:1 was used in this study has been reported in previous literature.[90] In brief, 10 ml of 0.5 M $AlCl_3$-THF solution

(Sigma-Aldrich) was added drop by drop in 10 ml of 1 M PhMgCl-THF solution, then stirred at least 24 hours prior to use. For the galvanostatic cycling test in symmetrical cells, the cells were cycled at 0.25 mA cm^{-2} for 1 h in each half cycle. In the battery assembly, fresh Mg metal electrodes or MgF_2-coated Mg metal was used as the working electrode and the counter electrode, and APC was used as the electrolyte. Cycling voltammetry was performed on Solartron-1470 instrument (England) with Bi positive electrode and Mg negative electrode at 25 ℃ at a sweep rate of 0.1 mV s^{-1}. The charge–discharge tests were conducted on a LAND cell test system (Land CT 2001A) and cycled between 1.0 V and 0.01 V (vs Mg^{2+}/Mg) at 25 ℃, and the capacity of the cells were calculated based on the amount of active material (Bi).

2.3. Results and Discussion

The formation process for the MgF_2-coated Mg electrode is illustrated schematically in Figure 3a. To remove the oxide layer on Mg foil, Mg was first washed with diluted hydrochloric acid (HCl, 0.1 M). The MgF_2 coating layer was then applied by treating the fresh Mg metal with 0.2M hydrogen fluoride (HF) by sonication. This reaction evolves hydrogen (H_2) gas and produces the fluoride surface protection layer via a metal exchange reaction ($Mg + 2HF \rightarrow MgF_2 + H_2$). No bubbles are observed on the Mg surface after sonication and HF treatment.

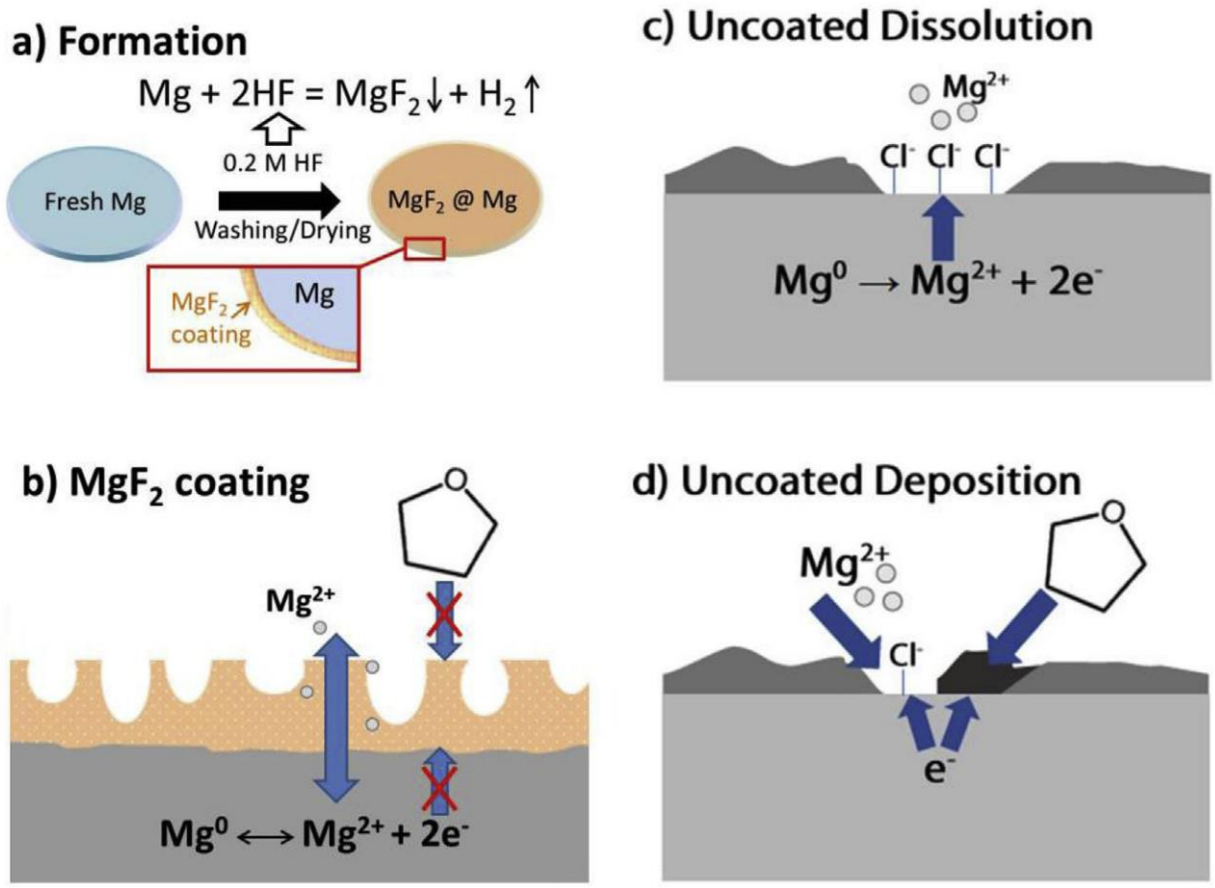

Figure 3. (a) Schematic illustration of the formation process of the MgF_2 surface coating. (b) Schematic of the proposed operating mechanism of the MgF_2 for stripping and plating of Mg metal. (c) Compared to the MgF_2 film, Mg stripping with a conventional Mg metal anode must proceed where the anode has not been passivated by electrolyte reduction products (dark gray). The active area is believed to contain an adsorbed layer of chloride ions. (d) Plating of the bare metal is not 100% efficient and leads to the growth of the layer electrolyte reduction products.

Using this design, the electrolyte (here, the all phenyl complex (APC) electrolyte[90]) is only in contact with the outer surface of the Mg electrode and cannot reach the inner Mg foil (Figure **3**b). The outer layer formed by MgF_2 is porous, but mechanically rigid and has a high hardness.[120] Thus, the inner Mg foil shrinks inward during the extraction, and during electrodeposition, Mg^{2+} penetrates through the passivating layer to react with the Mg metal. This passivation layer protects APC-based electrolytes from further decomposition on the Mg surface and favors the formation of a thin, porous layer with improved interfacial transport properties.

This is in contrast with the behavior of the bare Mg metal with APC. At high enough overpotentials, Mg^{2+} is extracted from regions where the bare metal has not been passivated by the electrolyte (Figure 3c). This reaction between the metal and organohaloaluminate electrolyte is believed to be mediated by adsorbed chloride ions on the surface,[82] whereas byproducts from the reduction of the electrolyte block Mg transport. When deposition takes place, Mg plating must compete with reduction of the electrolyte, leading to new growth of the surface passivation layer (Figure 3d).

Nitrogen gas adsorption-desorption isotherms were recorded to evaluate the surface area and pore sizes (Figure 4a). The BET derived specific surface areas of MgF_2-coated magnesium was 6.87 $m^2 g^{-1}$, which is significantly higher than that of fresh Mg (0.86 $m^2 g^{-1}$). The nearly order-of-magnitude higher surface area is largely attributable to the formation of hydrogen gas bubbles during the deposition of MgF_2. The passivation layer is conformally coated on the surface of the Mg electrode and provides a physical barrier to direct contact between Mg and the electrolyte. It is believed that the large specific surface area provides a large contact area between the electrode surface and the electrolyte for the electrochemical reaction to take place. Additionally, the BJH pore size distribution curve obtained from the nitrogen sorption isotherms suggests that the MgF_2-coated Mg electrode contains broadly distributed pores, most of which are smaller than 15 nm, with an average pore diameter of ~2.5nm (Figure 4b). The mesopore size and volume on MgF_2-coated Mg are advantageous for energy storage since the large pore channels permit rapid electrolyte transport at the interface.

The MgF_2 coating layer on Mg metal was observed by energy dispersive X-ray spectra (EDS) mapping of the cross-section of a MgF_2-coated Mg disc as shown in Figure 5a. Fluoride is uniformly distributed in the surface layer, which is <200 nm thick.

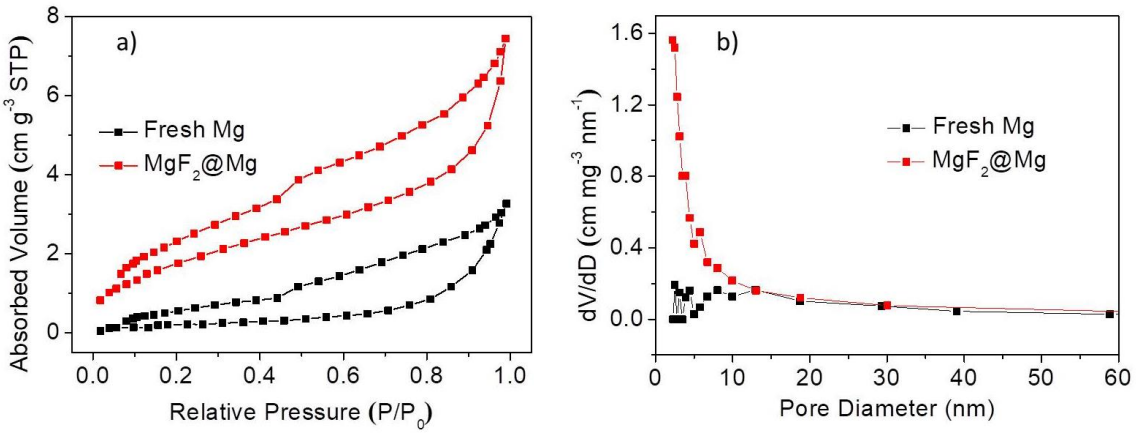

Figure 4. (a) N_2 isotherm adsorption–desorption curves for fresh Mg and MgF_2-coated Mg; (b) Barrett-Joyner-Halenda (BJH) desorption pore size distributions for fresh Mg and MgF_2-coated Mg.

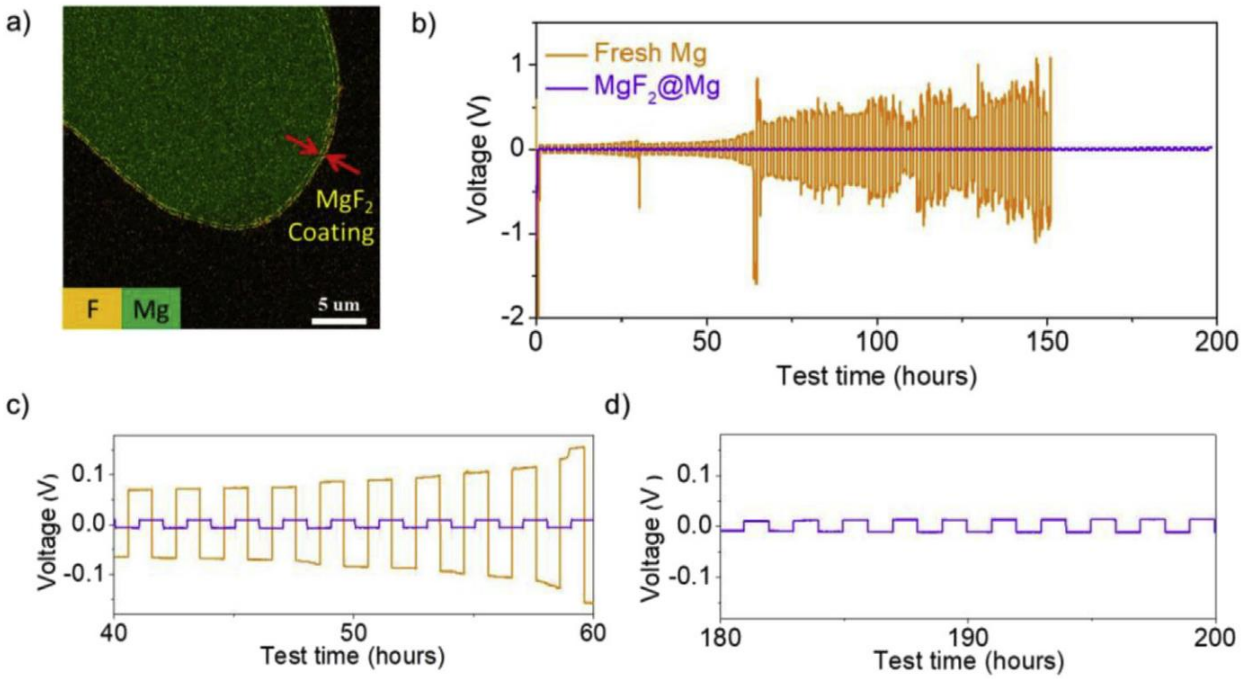

Figure 5. (a) Cross-section EDS mapping of the as-prepared MgF_2-coated Mg electrode. (b) Voltage profiles of the symmetric cells cycled with fresh and coated Mg metal at a current density of 0.25 mA cm^{-2} (1 h for each half cycle). (c) and (d) Magnified curves of the cycling for symmetric cells of fresh Mg (orange curve) and MgF_2-coated Mg (violet curve).

The overpotential for magnesium plating and stripping at the Mg-electrolyte interface was studied with APC as the electrolyte. To evaluate the electrochemical properties of the coated Mg

electrode, symmetrical Mg coin cells were assembled using the APC electrolyte and cycled at a current density of 0.25 mA cm^{-2} for 75 cycles. As shown in Figure 5b–c, the symmetrical cell with bare Mg electrodes experienced extremely high and rapidly increased hysteresis up to 200mV after 60 h, then followed by a severe overpotential increase around 65 h, which was probably caused by the passivation film derived from APC, indicating that the passivation film was unstable and high resistive. In contrast, the electrode coated with MgF_2 exhibited a lower voltage hysteresis of only ~25mV. The small resistance might also be attributed at least in part to an order of magnitude larger specific surface area of the MgF_2 interphase layer, but nevertheless no obvious losses from electrolyte degradation are observed, even after 100 cycles (Figure 5d).

To further assess the protective ability of MgF_2 on Mg metal, cyclic voltammetry (CV) was performed at a scan rate of 0.1 mV s^{-1} between 0.01 and 0.9 V (Figure 7). A slow sweep rate was used in this study to gain a better fundamental understanding of the electrochemistry and electrochemical performance by avoiding the kinetic impacts and the possibility of dendritic growth of Mg. Standard coin cells (2025) were assembled using bare or coated Mg foil as the negative.

Bismuth (Bi) was selected for the cathode in this work due to the high volumetric capacity (up to 3430 mAh cm^{-3}) and low potential for Mg alloying/de-alloying.[121,122] These results were obtained with one of our earliest formulations of the all-phenyl complex (APC) Mg electrolyte, where we could achieve stability up to only ~1.2 V, compared to 3.1 V reported by others.[90] Thus we were limited to using low-voltage Bi as our positive electrode. The Bi nanorod was synthesized via a solvothermal method using the reduction of bismuth oxide (Bi_2O_3) by ethylene glycol.[119]

The morphology and structure of commercial bismuth oxide (Bi_2O_3) and the obtained bismuth (Bi) nanorods were characterized by scanning electron microscopy (SEM), transmission electron microscopy (TEM) and X-ray diffraction (XRD) and the results are presented in Figure 6. A well-crystallized Bi_2O_3 framework with monoclinic Bi_2O_3 (JCPDS card no. 65-2366) is shown in Figure 6Figure 6a, while all the reflection peaks in Figure 6b are indexed as crystalline Bi (JCPDS card no. 44-1246) after the solvothermal method. The TEM images of the as-prepared Bi nanorods in Figure 6d show uniform diameters of ~150 nm, and the nanorods are aligned together to form a bundled structure held together by van der Waals interactions between the small rods.[119,122] The high resolution TEM image in the inset image of Figure 6d shows a fringe spacing of about 3.3 Å, corresponding to the spacing between the sheets of quasi-layered structure of bismuth.

Mg-Bi coin cells with Mg foil as the negative electrode and Bi/carbon composite as the positive electrode were assembled and tested. Figure 7a–b compare the CV curves of the Mg-ion batteries with anodes made of fresh Mg foil and MgF_2-coated Mg, and the corresponding redox peaks of the samples are listed in Table 3.

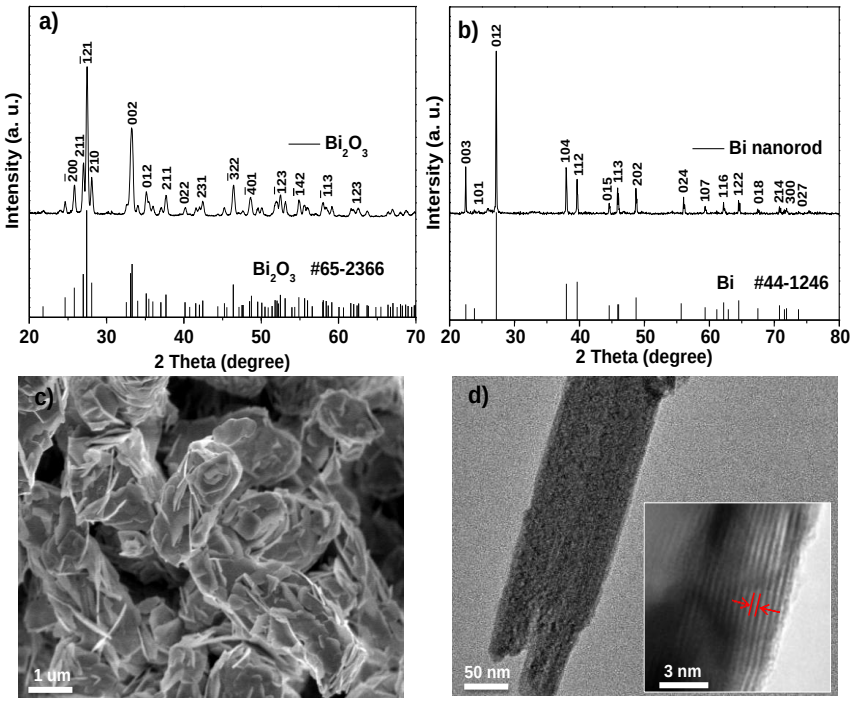

Figure 6. X-ray diffraction patterns of commercial Bi_2O_3 (a), as-prepared Bi nanorods (b) and standard XRD patterns for Bi_2O_3 (JCPDS no. 65-2366) and Bi (JCPDS no. 44-1246). The diffraction patterns of the materials show they are well-crystallized, and are in good agreement with the standard XRD patterns. SEM images of commercial Bi_2O_3 (c) and TEM image of Bi nanorods showing a bundle of nanorods. Inset shows high-resolution TEM image with a fringe spacing of about 3.3 Å (d).

Table 3. The redox peaks of the fresh and coated Mg foil.

Sample		1st	2nd	3rd
Fresh	Peak 1 (V)	0.13		
Mg	Peak 2 (V)	0.38	0.39	0.40
	Peak 3 (V)	0.50	0.52	0.54
Coated	Peak 1 (V)	0.18		
Mg	Peak 2 (V)	0.38	0.39	0.39

The reductive current displayed at 0.01 V is Mg^{2+} insertion and alloying with Bi ($2Bi + 3Mg^{2+} + 6e^- \rightarrow Mg_3Bi_2$), while the oxidative peak at about 0.4 V is attributed to the de-alloying reaction.[123] The increase of the reduction current is most likely associated with the wettability of electrolyte on the electrode, and the formation of the Mg_3Bi_2 alloy. This phenomenon was also

observed in different systems.[124] These symmetric peaks indicate good reversible electrochemical insertion/extraction of Mg-ions to and from the Bi electrode. In the case of the cell with fresh Mg electrode, it is worth noting that large current responses were observed at above 0.5 V in the anodic scanning. The de-alloying reaction between Mg and Bi only occurs below 0.5 V, as observed in different systems and reported in literature,[121,122,124] and the oxidation of APC is not expected to occur on positive electrode at this low voltage,[54] so this suggests that the current responses is attributed to the decomposition of the APC electrolyte on Mg electrode surface. Anodic scanning leads to the decomposition of physically adsorbed molecular films on Mg, leaving behind a deposition layer. It was observed that the alloying/de-alloying current gradually increased, and the decomposition peaks are still broad during subsequent cycles (at the 2nd and 3rd cycles). It indicates that the reaction of Mg_3Bi_2 undergoes an activation process where a physically adsorbed film was decomposed during the voltage scan. The unstable passivating film on the Mg surface leads to the continuous decomposition of the electrolyte.

Different electrochemical behavior was observed in the cell with MgF_2-coated Mg foil (Figure 7b). The voltage of the alloying peak in the first cycle somewhat positively shifted to 0.18 V. The reversible alloying/de-alloying current can be clearly identified, and the current peak for electrolyte decomposition above 0.5 V disappears. It suggests that the MgF_2 layer is favorable for the migration and diffusion of Mg cation ions but inhibits electron transfer and protects the Mg metal surface from side reactions. The slight decrease in the peak splitting in case of the bare Mg metal is indicative of an activation process characteristic of this system,[76] while the slight increase in polarization with the MgF_2 may indicate a minor increase in impedance at the surface of the anode. It suggests that Mg^{2+} extraction from MgF_2-coated Mg

electrode is easier than the pristine electrode and that the MgF_2 layer has a lower migration barrier for Mg cations compared to the physically adsorbed film. In addition, the peak current corresponding to electrolyte decomposition above 0.5 V is significantly suppressed. This voltage region exhibits a low cur- rent shoulder without any discernible peak on the subsequent cycles during Mg^{2+} depositing on the Mg electrode, which suggests the MgF_2 layer inhibits electron transfer between Mg and electrolyte and effectively protects the Mg metal surface from side reactions.

Constant current charge–discharge tests were also conducted to assess the electrochemical activity of the MgF_2-coated metal anode. Figure 7c-d shows the charge-discharge curves of the fresh and coated Mg metal at 30 mA g^{-1} for the 1st and 2nd cycle between 0.01 and 1.0 V. It reveals that the discharge voltage drops quickly to ~0.12 V and then rises to reach a plateau at approximately 0.2 V. This feature indicates that an activation process exists, which is mostly associated with the wettability between the electrode particles and electrolyte and the growth kinetics of the Mg_3Bi_2 alloy.[124]

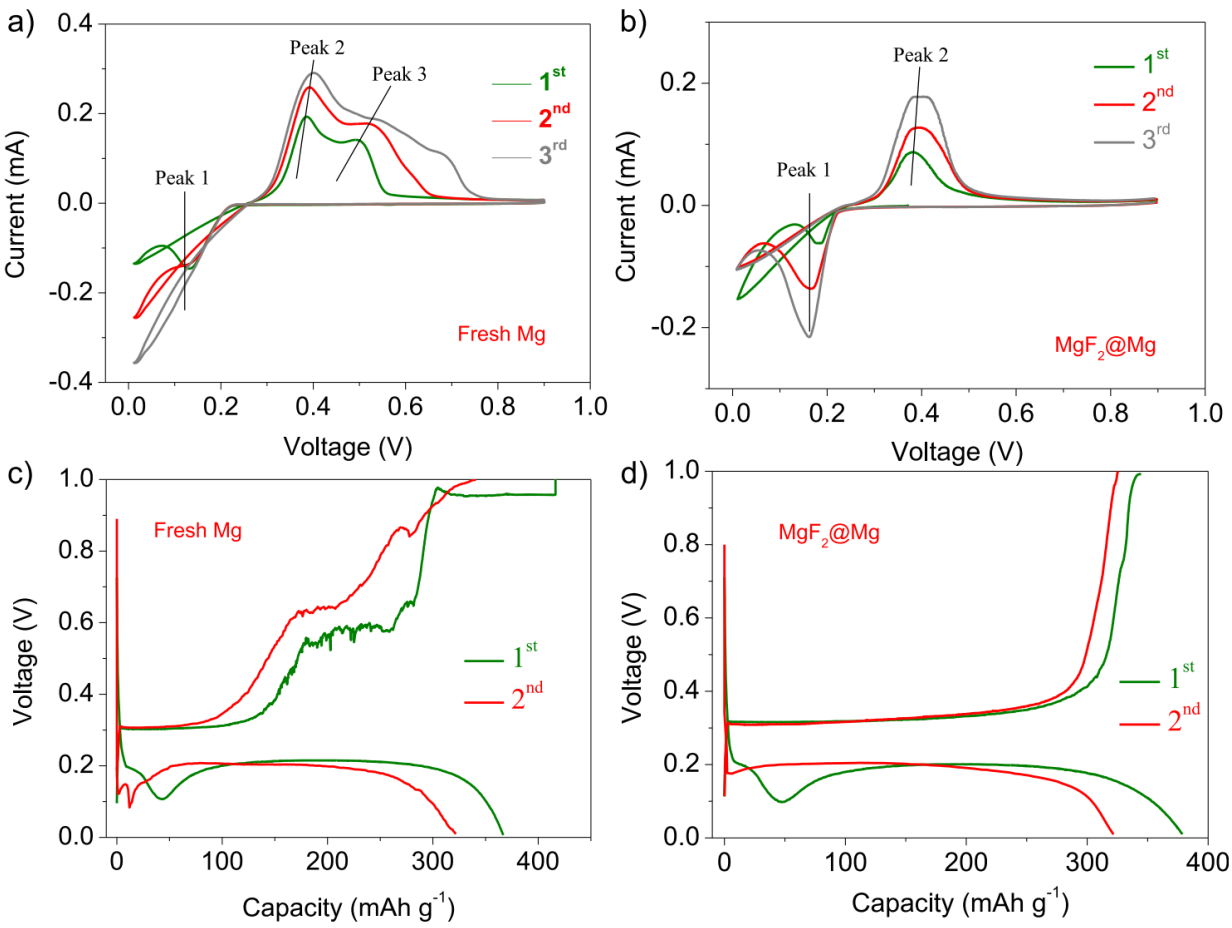

Figure 7. Cyclic voltammograms using Bi nanorods as positive electrode and different magnesium foils as negative electrodes: (a) Fresh Mg foil and (b) MgF_2-coated Mg foil; Scan rate: 0.1 mV s^{-1}. After coating the metal with MgF_2, the close voltage difference of the first cycle, ~0.2 V, between ions-insertion and extraction processes seems to show fast kinetics of migration and diffusion of Mg cation ions. The decomposition of the electrolyte is happening in the voltage above ~0.4 V in fresh Mg sample and its repeated reaction is observed. Galvanostatic charge–discharge profiles of the 1st and 2nd cycle for (c) fresh Mg and (d) MgF_2-coated Mg foil at a current density of 30 mA g^{-1}. The electrochemical measurements were carried out at 25 °C in 2025 coin cells. Capacity is calculated based on the weight of the active material mass of Bi.

The Mg insertion/de-insertion processes seen from galvanostatic charging and discharging are consistent with the CV results and suggests that Mg ions can be reversibly inserted into and extracted from the as-prepared Bi nanorods. However, at a higher de-insertion voltage, the cell with bare Mg metal displays two shoulders at around 0.5 and 0.9 V, and exhibits a Coulombic efficiency of 113% in the first cycle. These plateaus can be assigned to electrolyte decomposition

on magnesium metal. The reaction products on the Mg surface form a passivating layer which blocks the deposition of the Mg. As discussed in the next section, this instability in the voltage profile may be indicative of the unstable nature of Mg as a reference electrode,[125] and suggests increased surface impedance at the anode. Therefore, more energy needs to be dedicated to pushing Mg^{2+} through whatever passivation layer may exist and less energy is committed to inserting Mg^{2+} into the Bi material. This decomposition still occurs in the charging process at higher voltage in the second cycle and results in a Coulombic efficiency of 106%. It suggests that the surface film formed on the fresh Mg surface in the first cycle cannot fully prevent the decomposition of the APC electrolyte, and consequently lead to the continuous consumption of the electrolyte and growth of the passivating layer. For the cell using MgF_2-coated Mg foil, the long voltage plateau at around 0.3 V and the sharp increasing voltage starting from 0.4 V are identified during charging (Figure 7d), which is similar to the other Bi studies.[121,122] The first charge capacity is 340 mAh g^{-1}, while the Coulombic efficiency is 90% and reaches 99% in the second cycle. Notably, the polarization of MgF_2-coated Mg in the second discharge curve is smaller than that of fresh Mg, indicating the dissolution of Mg^{2+} from Mg in MgF_2 layer is easier than the passivation layer derived from APC decomposition on fresh foil. These strongly suggests that the MgF_2 layer is not only an ionically conductive film for Mg^{2+} transport but also an effective passivating layer that protects against side reactions.

The cycling performance of fresh Mg and MgF_2-coated Mg are shown in Figure 8a. The cells were (dis)charged at a current density of 30 mA g^{-1} for initial two cycles, followed by cycling at a current density of 120 mA g^{-1} in the voltage range of 0.01-1.0 V. The charge capacity of the cell with fresh Mg decreased from 416 to 275 mAh g^{-1} with over 100% of coulombic efficiency in the first seven cycles, then the capacity gradually increased in the subsequent cycles. This is

attributed the decomposition and activation process identified from the CV results. More importantly, the APC electrolyte fails to form a stable passivating layer on Mg, which continually consumes the electrolyte during cycling and leads to the increased irreversible capacity. Note that the coulombic efficiency also fluctuates during cycling and the charge capacity remains at 232 mAh g^{-1} after 50 cycles. This can be ascribed to the compacted Bi nanorods in the present work that might suffer from serious structural transformation resulted from the large volume change (~100%) during the alloying and de- alloying process. It might contribute to the capacity fading with a loss of electrical contact between the active material and the conductive additive. More importantly, the voltage profiles of the fresh Mg electrode between 0.01 and 1 V with representative cycles reveal that the voltage of the discharge plateau is decreased, while the charging voltage increases during cycling, as shown in Figure 8b. It indicates the polarization of the electrodes increase because of the slow kinetics and reduced Mg^{2+} diffusion in the (dis)charge process after long cycling. These results suggest that the surface film formed in fresh Mg is unstable and the film seems to be electronically conductive because side reactions at Mg continue throughout testing, and results in the formation of a passivating layer which causes the fast deterioration of the cells in the long cycling. However, for Mg coated with MgF_2, the charge capacity is 342 mAh g^{-1} at a rate of 30 mA g^{-1} and the capacity remains 286 mAh g^{-1} after 50 cycles, exhibiting a better retention property compared to fresh Mg. The coulombic efficiency after the first cycle is nearly 100% during all subsequent cycles. Remarkably, no obvious change in galvanostatic voltage profiles during the long-term cycling (Figure 8c), demonstrating the good stability of the surface film after the MgF_2 coating. The evidence shows the passivating layer formed by MgF_2 suppresses the electrolyte

decomposition and eliminates the side reactions between Mg and the APC electrolyte leading to lower polarization and improved cycling stability.

The rate performance of the cell with fresh Mg or with MgF_2-coated Mg was evaluated at various (dis)charge current densities. The cells were tested at 30, 120, 300, 600, 1800, and 3000 mA g^{-1} in turn as shown in Figure 8d, the corresponding discharge capacities are 307, 280, 275, 272, 184, and 152 mAh g^{-1} for Mg and 317, 322, 321, 329, 227, and 226 mAh g^{-1} for MgF_2-coated Mg. The coated electrode also displays a good capacity recovery when the current density switches back from 3000 mA g^{-1} to 120 mA g^{-1}, suggesting good electrode structure stability and reaction reversibility. All these improvements are attributed to the excellent ionic conductivity and suppressed side reactions at the metal interface enabled by the MgF_2 buffer layer.

In order to further confirm the Mg^{2+} conductivity, electrochemical impedance spectroscopy (EIS) was carried out at room temperature. Figure 8e shows the Nyquist plots for the cells consisting of fresh Mg and MgF_2-coated Mg electrode after three cycles. The experiments results show depressed semi-circle response for both electrodes, suggesting porosity within the electrode surface.[126] Fitting the Nyquist plots with an equivalent circuit (Figure 8f) composed of internal resistance (R_s), passivation film resistance (R_f), and charge transfer resistance (R_{ct}). After coating with MgF_2, the overall resistance ($R_s + R_f + R_{ct}$) is smaller than that of fresh Mg foil, as shown in Table 4. This result indicates that, even though the charge transfer resistance is greater with the coated material, the MgF_2 layer is more ionically conductive than the native film that forms on Mg in APC.

Table 4. Fitting results of EIS for fresh and coated Mg foil.

Sample	R_s (Ω)	R_f (Ω)	R_{ct} (Ω)
Fresh Mg	60	2553	4800
Coated Mg	114	1022	5331

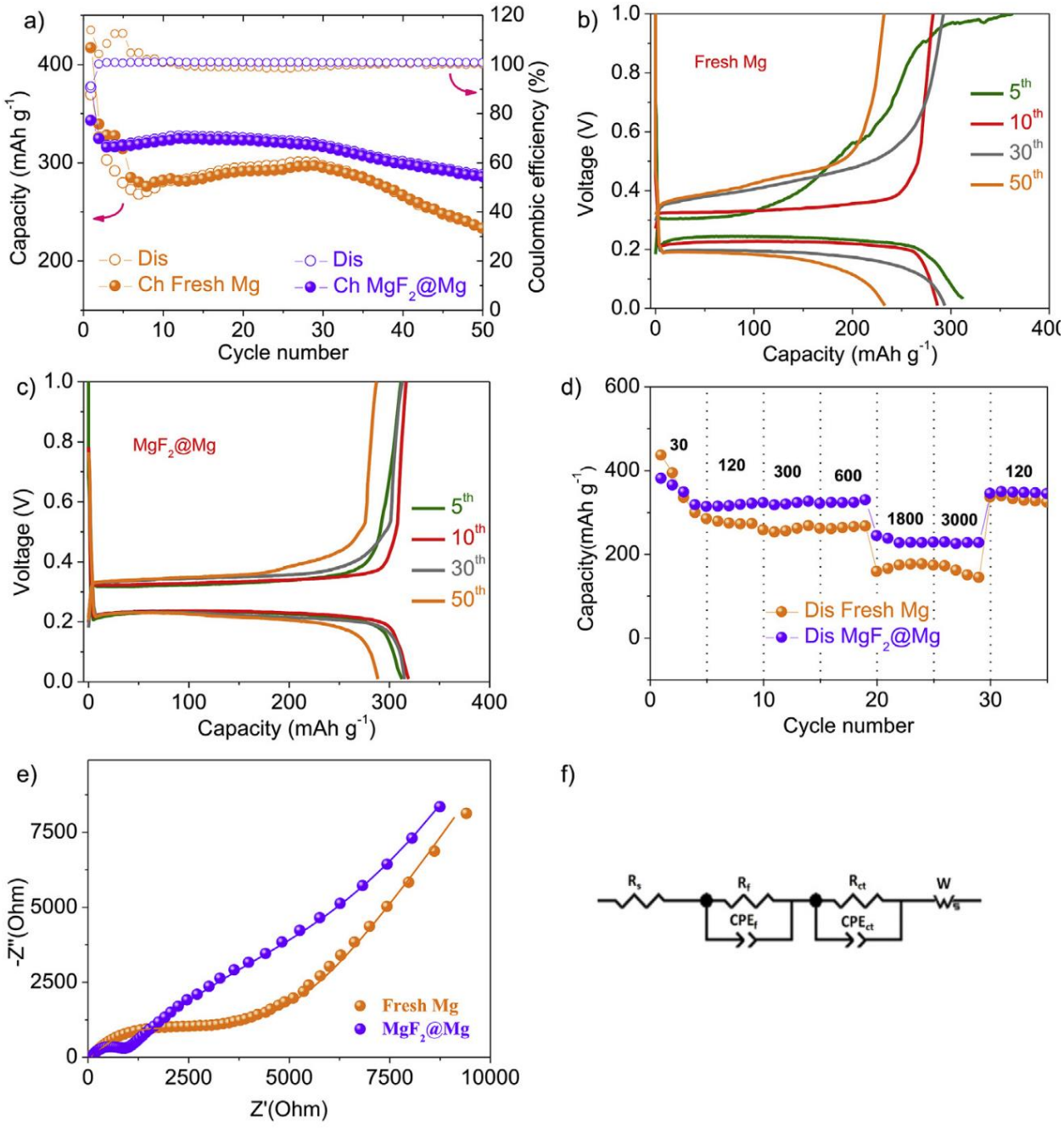

Figure 8. Charge-discharge tests using Bi nanorods as positive electrode and fresh or coated magnesium foils as negative electrodes: (a) Cycling performance of fresh Mg and MgF_2-coated Mg foil in the range of 0.01-1.0 V, charge-discharge voltage profiles of fresh Mg (b) and MgF_2-coated Mg (c) at a current density of 120 mA g^{-1} between 0.01 and 1.0 V. (d) The comparison of the rate capability of the fresh Mg and MgF_2-coated Mg at different current densities. The cells

were tested at 30 mA g^{-1}, 120 mA g^{-1}, 300 mA g^{-1}, 600 mA g^{-1}, 1800 mA g^{-1}, and 3000 mA g^{-1}. (e) Electrochemical impedance spectroscopy and fitting results for fresh Mg and MgF_2-coated Mg foil after 3 cycles. (f) Equivalent electrical circuit model for the EIS.

The surface morphology of the Mg foils cycling was observed by SEM before and after three cycles (Figure 9a-d). Each image includes an inset that shows the electrode's appearance. The relevant EDS spectrum is also presented at the bottom of each image and the elemental content estimated from EDS is shown in Table 5. Prior to cycling, the surface of the fresh Mg foil is smooth with metallic color but has some wrinkle-like features in the SEM (Figure 9a) which resulted from the HCl washing process. The existence of elements carbon and oxygen in Figure 9**Error! Reference source not found.**e-h are attributed to the carbonate and oxidation or the adsorption of the CO_2 and O_2 when the samples were exposed to the air while the sample was transferred. A sharp magnesium peak is observed whereas chlorine is not in the as-prepared fresh Mg foil. This confirms that HCl is removed completely after the washing process.

After soaking in HF, the hue of the Mg foil becomes slightly yellow and fluorine is detected in the EDS spectrum (Figure 9b, f), indicating MgF_2 has been successfully coated onto the Mg surface. This treatment produces a flexible and ionic conductive framework with a porous structure at the surface, likely formed by H_2 gas bubbles during the HF treatment (cf. the BET data in Figure 4a). After the cell with uncoated Mg was charged and discharged three times, the Mg surface was observed to turn dark and a thick fluffy deposit was padded on the Mg, as shown in Figure 9c. In addition, aluminum and chlorine are clearly observed from EDS in Figure 9g and the carbon and oxygen content increased compared to the pre-cycled Mg foil (Table 5). Since aluminum and chlorine exist only in APC electrolyte, but not in Mg foil or in Bi electrode, it clearly suggests that the thick layer is derived from insoluble precipitates from the APC

electrolyte. This is strong evidence that the APC electrolyte decomposes because of the high reactivity of the Mg metal and the instability of the electrolyte formulation. However, this situation did not happen when Mg was coated with MgF_2 passivating layer. Only minor visual, morphological changes were observed in Figure 9d and h and the elemental content remains nearly the same after cycling (Table 5). As diagramed schematically in Figure 3, this observation confirms that a protective passivating layer can be formed by the MgF_2 coating, which protects the Mg foil and suppresses electrolyte decomposition.

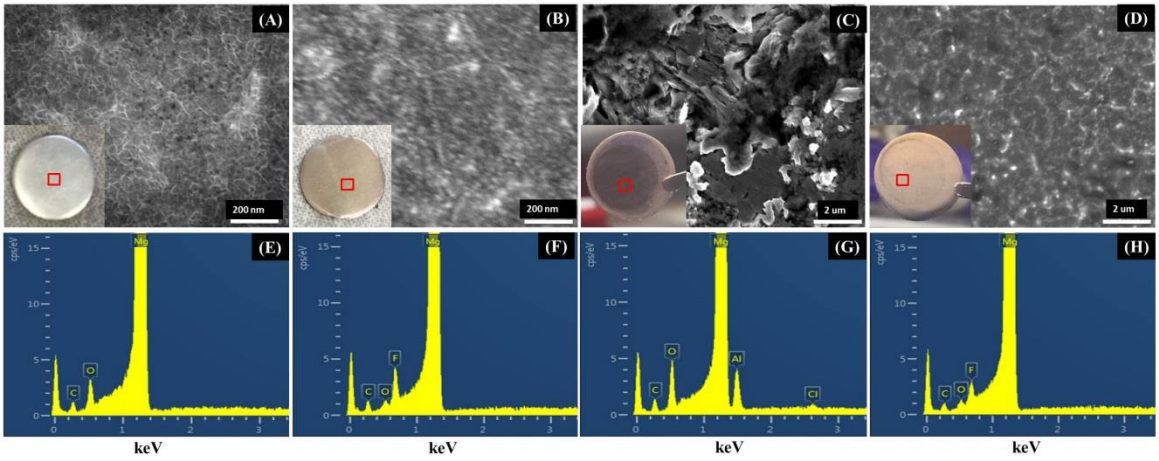

Figure 9. SEM images of Mg electrodes: fresh Mg (A) and MgF_2-coated Mg (B) before cycling, fresh Mg (C) and MgF_2 coated Mg after 3 cycles. (Photographs of the Mg electrodes disassembled from coin cells are shown in the inset); EDS patterns of the surface of the Mg electrodes from fresh Mg (E) and MgF_2 coated Mg (F) before cycling, and fresh Mg (G) and MgF_2 coated Mg (H) after the cycling.

Table 5. Elemental content of the samples from EDS.

Sample	Mg(%)	O (%)	C (%)	F (%)	Al (%)	Cl (%)
Mg pre-cycling	91.9	2.4	5.7	-	-	-
Mg after cycling	85.4	4.3	7.3	-	2.8	0.2
MgF_2 pre-cycling	92.1	0.6	5.5	1.8	-	-
MgF_2 after cycling	92.5	0.9	5.6	1.0	-	-

SEM images of the bare Mg electrode taken before cycling show a smooth surface. Elemental mapping only shows Mg and a small amount of C and O, attributed to the momentary exposure to air during sample transfer (Figure 10a). After three galvanostatic cycles using APC as the electrolyte, the surface is much rougher and deposits of Al and Cl from the electrolyte are apparent (Figure 10c). In contrast, SEM shows the Mg electrode coated with MgF_2 appears smooth before cycling and only modestly rougher after (upper left inset Figure 10b and d). The intensity of the elemental maps before and after cycling shows no major change in the surface composition and does not indicate any Al- or Cl-containing side products – evidence for the efficacy of the MgF_2 layer in preventing parasitic side reactions with the electrolyte.

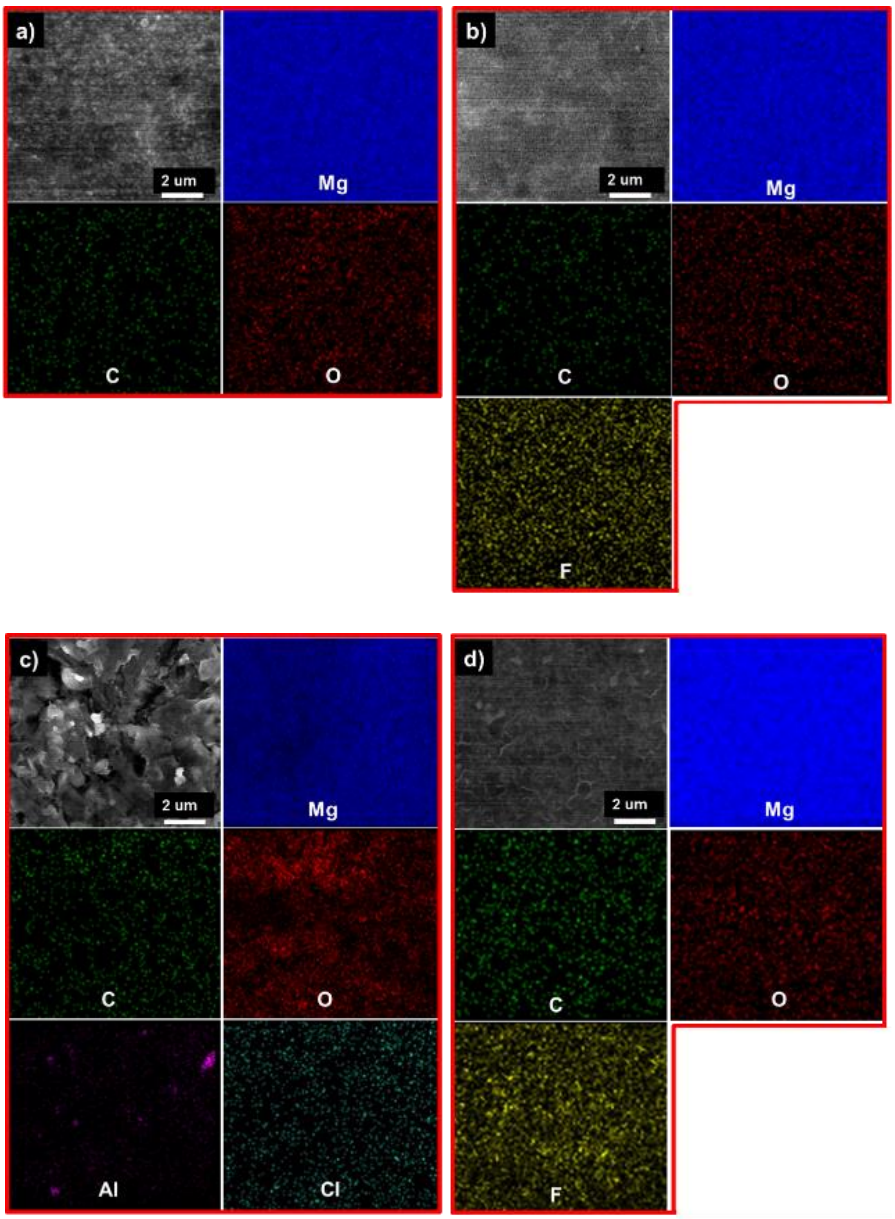

Figure 10. EDS mapping of the fresh Mg (a) and MgF_2-coated Mg (b) before cycling, and fresh Mg (c) and MgF_2-coated Mg (d) after the cycling. It reveals that the uncoated Mg surface consists of Al, Cl and increased O content that derived from the decomposition of APC electrolyte. However, the carbon and oxygen distribution of the coated Mg sample increased only slightly after cycling.

The discovery of Mg^{2+}-conducting surface films contradicts conventional wisdom that passivation films on Mg metal are fully insulating[62] and the assumption that MgF_2 would be impassable to magnesium transport.[63,115,127] However, this discrepancy can be resolved with a close reading of the literature. Lu et al.'s original study[62] and recent results from the Aurbach

lab[63] show that electrolytes using PF_6^- will passivate Mg anodes. However, the conformal MgF_2 surface film formed from our treatment likely bears little resemblance to the fluoride-containing surface film formed when PF_6^- anions or solvent molecules are reduced at the metal surface. The nature of the MgF_2 film and the reasons behind why it permits Mg^{2+} transport deserve further study so that improved Mg-conducting SEI layers or solid-state electrolytes might be developed.

Overall, the Mg electrodes coated with MgF_2 perform better than those based on fresh Mg foil. By carefully studying the morphology and the structure-property relationship, we propose the following main reasons for the high performance. First, the MgF_2 coating helps protect the APC electrolyte from decomposition on Mg surface. The stable passivating layer prevents the direct exposure of magnesium to the APC electrolyte and, thus, enhances the stability of electrolyte. This is supported by the fact that the major difference in irreversible capacity comes from the first and second charge curve. Second, it is possible the MgF_2 benefits the electrochemical performance, since MgF_2 has been reported to facilitate Mg^{2+} conductivity in the electrolyte as salt.[128,129] Finally, the passivating MgF_2 layer is carefully designed so that the passivating layer covers almost all the exposed surface of Mg, which minimizes the side chemical reaction and helps improve interfacial compatibility between electrode and APC electrolyte.

2.4. Conclusions

In this work, we report improved compatibility between Mg metal and the electrolyte interface through a simple coating technique, wherein an ionically conductive but electronically insulating magnesium fluoride (MgF_2) layer forms when Mg is immersed in hydrofluoric acid. With this passivating layer, the voltage stability, coulombic efficiency and cycling performance of a Bi/Mg cell are appreciably improved. This is attributed to successful suppression of the

electrolyte side reactions. This design principle for Mg metal surface chemistry has important applications in Mg battery technology.

Chapter 3. Experimental Design for Magnesium Cathode Studies

3.1. Introduction

At the cathode side of the magnesium battery, there are two main issues. First, electrolytes that are compatible with magnesium have relatively narrow voltage windows. The family of organohaloaluminate/ether electrolytes reported by Aurbach *et al.*[53] reversibly strip and plate magnesium but they are only stable up to ~2.2 V. Advances have extended this range to ~3.1 V for the "all-phenyl complex" electrolyte (APC),[54] but the reproducibility of these results has been hard to control. This has not only been a problem in our own lab but is acknowledged as a problem by other prominent researchers in the field.[71]

The second major problem pertains to the cathode materials, which suffer from low total energy density or limited cycling performance. Large overpotentials and low intercalation levels are often cited as evidence for slow transport kinetics.[130–132] However, a growing body of work disputes this common preconception and instead suggests removing ligands from Mg^{2+} at the cathode interface (i.e. desolvation) is the true bottleneck.[133,134]

Enhanced electrostatic effects from the divalent ion are usually cited as the culprit for slow diffusion, but are mitigated by the host's ability to delocalize electrons and change valence states.[135–137] While Chevrel phases are the best example from the very small set of kinetically fast, long-term stable cathode materials demonstrated thus far (>2500 cycles, Figure 11),[53,135] their low voltage and theoretical capacity (~1.1 V, ~128.8 mA h g^{-1} for Mo_6S_8) make them uncompetitive compared to Li-ion cells.[138] In contrast, the low bar of 30-100 cycles is considered to be reasonably good performance for other cathode materials.[139]

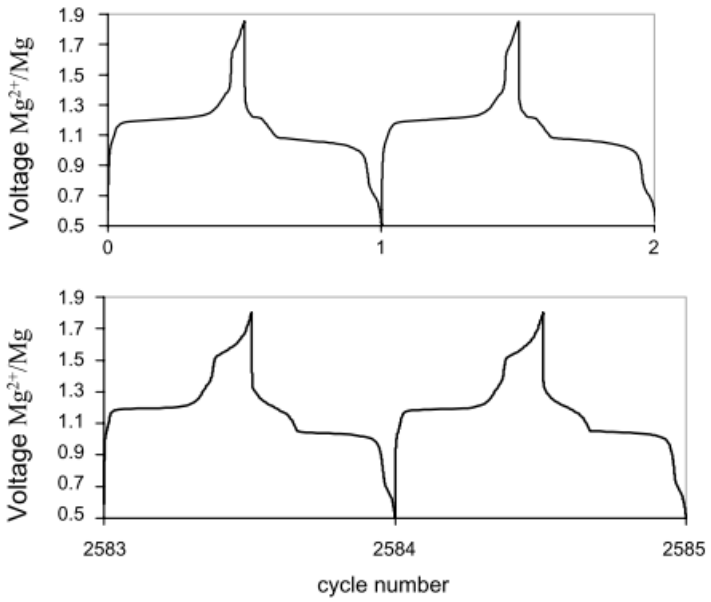

Figure 11. Voltage profiles for rechargeable Mg/Mo_6S_8 coin cells demonstrate excellent longevity. Reprinted from ref. [135] Copyright © 2003 The Japan Chemical Journal Forum and Wiley Periodicals, Inc.

We believe the poor performance of most cathode materials reported to date is not an intrinsic limitation, but is in part a problem compounded by improper electrochemical design. Previously, we have reviewed a large number of discrepancies concerning the electrochemical design of magnesium battery studies.[50] Our critical review found that studies on the magnesium electrolytes[53,67] and their compatibility with Mg metal[62,140] and current collectors[87,141–145] often conflict with the experimental protocol reported in a significant fraction of publications on magnesium cathodes. Presumably, these experimental protocols have been designed on the implicit assumption that the setups used in Li-ion research carries over to magnesium studies. However, this is demonstratively untrue in the case of electrolyte and cathode material performance, and should not be assumed in the case of any other component of a magnesium battery cell. Here we briefly review certain procedural pitfalls that have plagued the literature.

3.1.1. Electrolytes

The dearth of robust magnesium electrolytes has long hampered the search for high-voltage

cathode materials. For convenience, electrolytes such as $Mg(ClO_4)_2$ in AN or PC have often been substituted to study electrochemistry at the cathode. However, the high charge density of Mg^{2+} leads to large de-solvation energies at the cathode (roughly 3 times larger than for Li^+).[146] Therefore, the choice of Mg electrolyte will have a much more significant impact on the performance of the cathode. Complicating this further, not all electrolytes interact with the different cathode materials in the same way. For example, while excellent cycling performance is observed for Chevrel phase materials in $Mg(AlCl_2BuEt)_2$/THF and APC,[53,54] fundamentally poorer behavior is observed for the same cathode in $Mg(ClO_4)_2$/AN, and no insertion at all occurs when the solvent is PC.[147] However, oxides like TiO_2 and V_2O_5 do not react with APC at all but show better performance in other electrolytes.[55,148] This contradicts the common view that solid state diffusion of Mg^{2+} in the cathode governs its performance and instead forces us to shift the focus to understanding the reaction mechanism of Mg^{2+} at the cathode-electrolyte interface. This will be a complicated process (requiring concerted transfer of two electrons and the magnesium ion) that may be unique to each combination of cathode and electrolyte and requires urgent attention.

Further, water in the electrolyte has been long known as crucial to improving electrode capacity,[132,134] while other additives like LiCl boost ionic conductivity.[68] Moreover, there is no guarantee that Li intercalation compounds will react with other ions by the same mechanism.[149,150] Since the cathode-electrolyte interface is not nearly as well understood compared to the magnesium-electrolyte interface, we suggest that it is worth isolating the cathode before rushing into full-cell magnesium batteries.

3.1.2. Counter and Reference Electrodes

Another related issue that has long been reported is the passivation of Mg in most conventional salts and solvents.[52,62] However, the severity and rate of passivation is not entirely

clear, as many studies report reversible (albeit limited) electrochemistry using this combination of anode and electrolyte. Again, it may be the case that such studies show the results of limitations on the electrochemical system and not the cathode alone. Although this possibility is not often addressed, results published by Liang *et al.*[151] support this hypothesis. By nanosizing both the MoS_2 cathode material and the Mg anode, nearly twice the capacity was obtained compared to the cases where only the cathode material particle size was reduced.

However, the cells were charged up to 3 V, which is beyond the stability window of the electrolyte, $Mg(AlCl_3Bu)_2$, (~2.5 V[67]), and the Cu and Al current collectors (< 1.8 V[87]). It has been suggested that at low current densities, the anode will not be fully passivated by the formation of surface films.[152] Results from our group[94] and other groups investigating magnesium metal coatings[77,78,95] have shown a similar trend – full cells with different cathodes demonstrate superior performance with the coated magnesium metal compared to the bare magnesium metal alone. This underappreciated results strongly implies that many systems and cathode materials have unknowingly been studied under *anodically* limited conditions. This further suggests that many "unworkable" cathode materials may be perform better than has otherwise been assumed.

To this point, even in the case where the Mg anode is not totally passivated (and thus still usable as a counter electrode), it should be understood as a quasi-reference electrode – and not a very good one.[125] Native surface films will be present on Mg even after polishing the metal in a glove box,[62] and additional films (of varying thickness and resistivity) are expected to grow after immersion in the electrolyte. If that electrolyte passivates Mg, then the potential of the reference electrode is no longer governed by the reversible Mg/Mg^{2+} couple, but by the potential of whatever surface films form. When this has been taken into consideration, the voltage of a Mg

metal quasi-reference electrode has been consistently more positive than the reversible Mg/Mg^{2+} redox couple by 0.5-0.7 V in some cases[62,153,154] and up to 1 V in others.[125] Hence, the discharge voltages measured at the cathode are significantly lower than the equilibrium potential, which may partially explain the difference between experimental and theoretical voltages obtained in some cases.

This is yet another situation where the design of the experimental setup adversely affects the observed cathode energy densities. To avoid this issue, silver-ion and activated carbon electrodes can serve as reference electrodes in nonaqueous three-electrode experiments,[155–159] and similarly activated carbon can serve as readily available alternatives for the counter electrode.[158,159]

3.1.3. Current Collectors

Lastly, the current collector has often been overlooked. Corrosion of current collectors in Li-ion batteries is a known issue that affects long-term functionality and safety.[160,161] While Cu or Al foil are popular choices for Li-ion research, it has been shown that both corrode at relatively low potentials in $Mg(AlCl_2BuEt)_2$/THF (no greater than 1.8 and 1.2 V, respectively).[87,145] This shows that the usable voltage window for electrolytes is also dependent on the current collector. Similar results were obtained for Ni and stainless steel, which are stable up to ~2.1 V,[141] but chloride-containing electrolytes are corrosive to stainless steels used for battery casing components.[86] Dissolution of the current collector can interfere with the intended electrochemical response in cyclic voltammetry (CV) studies, as the observed corrosion current looks the same as the desired electrochemical reaction at the same potential. For the purposes of fundamental studies into the failure modes and reaction mechanisms, we have developed a simple and robust process for screening cathode materials without encountering these issues.

Searching through the MIB cathode literature reveals a slew of inconsistencies. These issues include operating the cells outside the voltage stability window of the electrolyte, charging

cathode current collectors above their dissolution potential, and using Mg as an electrode in passivating electrolytes. These various effects cast some doubt on the veracity or reproducibility of some magnesium studies, while in other cases substandard design options may curtail the performance of ostensibly underachieving materials. This work provides a template towards avoiding both cases.

3.2. Methods

3.2.1. Materials Synthesis

Vanadium pentoxide xerogel was prepared as the active material for initial screening. In a typical synthesis, 136 mg of vanadium pentoxide (Sigma Aldrich) was stirred with 2 mL of deionized (DI) water and 0.6 mL of 30% hydrogen peroxide (Fisher Scientific) for 15 minutes, then sonicated for another 10 minutes. The solution was diluted to 13 mL with DI water to obtain a 60 mM solution. This solution was sonicated for 80 minutes, changing the water after 40 minutes to reduce the temperature of the sonication bath. This solution was diluted to 7.5 mM with 89 mL of DI water and stirred until the solution was translucent. Roughly 100 μL of the solution was dropcast on FTO glass and annealed at 240°C for three hours.

3.2.2. Electrolyte Synthesis

The 0.33M APC electrolyte was prepared in a glove box by adding 25 mL of 2.0 M PhMgCl in THF dropwise to 50 mL of 0.5 M $AlCl_3$ in THF (both solutions were available from Sigma Aldrich). The mixture was stirred over a weekend to provide sufficient stability.

A second electrolyte, 0.3M $Mg(TFSI)_2$ in a 1:1 mixture of glyme and diglyme was prepared according to Ha *et al.*[162] To prepare 50 mL of this electrolyte, 8.769 g of the $Mg(TFSI)_2$ (Solvay, France) was added to a 1:1 solution of the two solvents, glyme and diglyme (Sigma Aldrich).

3.2.3. Materials Characterization

The phase of the annealed V_2O_5 xerogels ($V_2O_5 \cdot nH_2O$) were studied using X-ray diffraction (XRD, D8 Bruker X-ray diffractometer) with Cu-K_α radiation between 5 and 45°C (2θ). Samples

were also characterized using thermogravimetric analysis (TGA) from room temperature to 500°C (TGA 7, PerkinElmer) under nitrogen at a heating rate of 5 °C min^{-1}.

3.2.4. Electrochemical Measurements

Various custom-built three-electrode cells were built using sealed glass jars with copper wire leads threaded through the cap and sealed with epoxy. Cells were assembled in an argon-filled glove box using approximately 5 to 10mL of one of the two electrolytes described above for each experiment.

Different substrates were selected as the current collector (working electrode) to be screened as a blank experiment using the two prepared electrolytes. These were stainless steel foil, nickel foil, platinum foil, and fluorine-doped tin oxide (FTO) glass (all from Sigma Aldrich). Rectangles of polyacrylonitrile carbon felt (CeraMaterials) were cut and used as both the counter and reference electrode. The dimensions for the counter electrode were roughly 1 cm x 2 cm x 0.3 cm and roughly 1cm x 0.5cm x 0.3 cm for the reference electrode.

Cyclic voltammetry was conducted using one of two potentiostats (Solartron 1287, UK or CH Instruments, Model 605C, US) at scan rates of 200 mV s^{-1} to find the electrochemical stability window for each pair of working electrode and electrolyte. The open circuit potential of a three-electrode cell using carbon as both the reference and working electrode was obtained over 24 hours using an Arbin battery tester (BT-2000, Arbin Instruments). For comparison, the open circuit potential of a symmetric Mg//Mg cell was measured using 2016-type coin cells with APC as the electrolyte.

3.3. Results and Discussion

The main thrust of section is focused on identifying the appropriate protocol for magnesium battery cathode studies. Often coin cells using magnesium metal as the reference electrode are employed in magnesium battery tests. However, we have found that magnesium is not a reliable

reference electrode, even in electrolytes like APC that are known to reversibly plate Mg metal. The open circuit potential of a magnesium symmetric cell (i.e. a coin cell where Mg metal is used as both the positive and negative electrode) should be close to 0V if it is to be used as a suitable reference electrode. Here, Mg metal would more accurately be called a quasi-reference electrode because the precise reaction potential of the metal in nonaqueous systems is not known, but can be calibrated using an internal standard like the ferrocene (Fc/Fc^+) redox couple.[163] However, this is clearly not a stable reference potential even under open circuit conditions (Figure 12). Instead, we have used carbon felt as a significantly more robust and reliable quasi-reference electrode, analogous to other reports.[157,158] The voltage difference between the Mg electrodes grows over time, indicated nonuniform growth of some surface films in the electrolyte. Over the course of 24 hours, the average voltage difference was 0.218V vs. itself with a standard deviation of 49mV, which is unacceptably poor performance. In contrast, the voltage difference between two carbon electrodes was less than 4mV over the entire day and fluctuated by less than 1mV. This gives us much greater confidence in our own measurements and less confidence in many measurements reported in the literature.

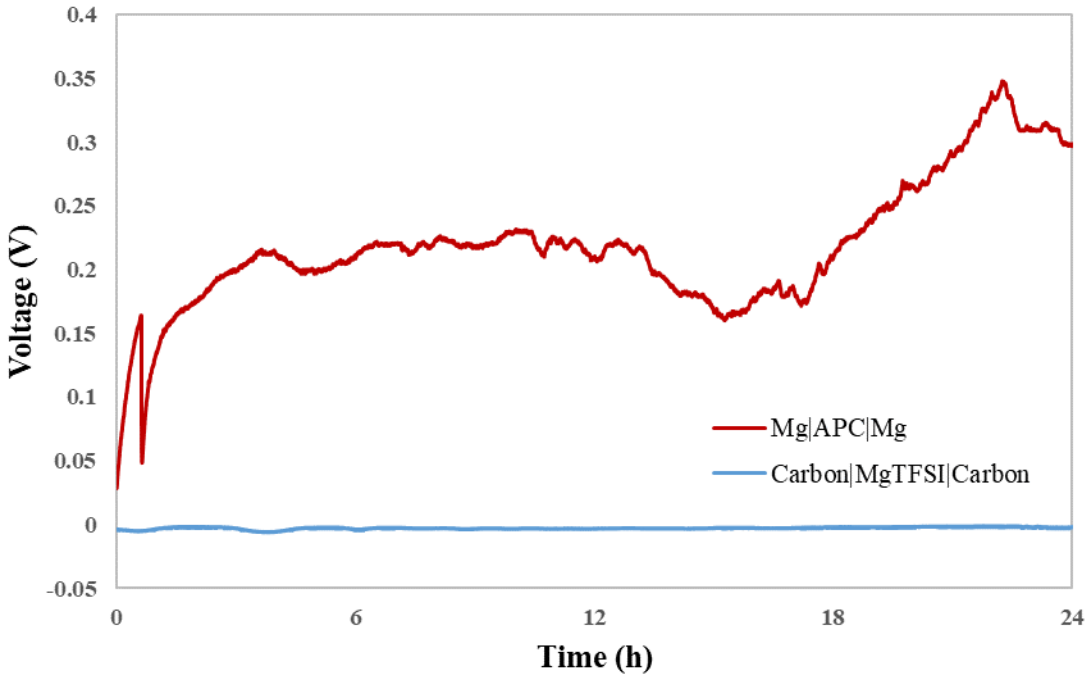

Figure 12. The open circuit voltage of magnesium metal against itself (red) is not as stable as implicitly assumed. Using PAN carbon felt (blue) in a three-electrode configuration is much more stable and reliable over the course of 24 hours.

The carbon quasi-reference electrode was calibrated using ferrocene as an internal standard. Across scan rates of 5, 10 and 100 mV s^{-1} the halfway potential ($E_{1/2}$) of the Fc/Fc^{+} was found to be 0.712 ± 0.031 V vs. carbon. The scan at 10 mV s^{-1} with APC as the electrolyte and Pt foil as the working electrode is shown in Figure 13. Conversion between reference potentials gives carbon (where the current is supplied by adsorption of anions from the electrolyte) a voltage of ~2.5V vs. Mg/Mg^{2+}.[164] This is in agreement with other results[158] although this figure may only be accurate to within 200mV because of the uncertainty associated with different nonaqueous solvents.[125] Interestingly, the peak-to-peak splitting between the oxidation and reduction potentials is rather large (282 mV). This means the reaction was only quasi-reversible and suggests that the ionic conductivity of this electrolyte (0.33M APC) is low and may need to be improved, or may be uncharacteristically slow reaction kinetics in this electrolyte.

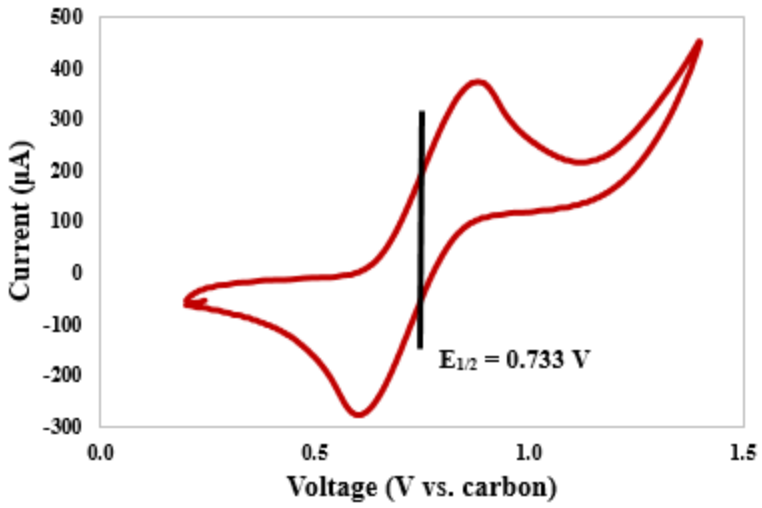

Figure 13. The Fc/Fc+ redox couple exhibits quasi-reversible kinetics in APC using a Pt foil working electrode and a scan rate of 10 mV s^{-1}. The rise in current above ~1.2V indicates the onset of electrolyte decomposition.

The electrolytes used in this study we selected based on their ease to prepare and to give contrast between two different families of salt and solvent. The electrochemical voltage window depends on both the identity of the electrolyte and the identity of the surface that is being polarized (the working electrode). Cyclic voltammetry using different substrates at the working electrode gave information about where the electrolyte begins to break down. Thin foils of platinum, nickel, stainless steel were tested as well as FTO glass. Since most tests are run using coin cells, FTO glass has not be previously reported. However, we find that our three-electrode configuration is readily amenable to using FTO glass as a substrate and it outperforms the other three materials for both electrolytes considered here (Table 6). The first scan for each working electrode in $Mg(TFSI)_2$//glyme/diglyme is shown in Figure 14, where it is stable almost 1V beyond the rest. Qualitatively similar results were obtained for APC. FTO glass holds steady or improves after 5 cycles (some passivation process reduces the observed current after successive

cycles), whereas combinations like APC and stainless steel show increasing corrosion currents and reduced voltage stability, as expected for corrosive chloride-containing electrolytes.[86]

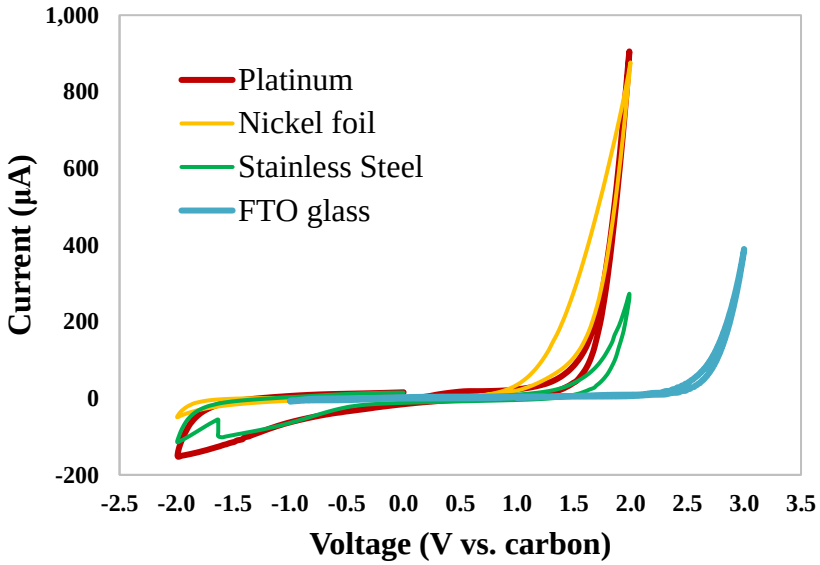

Figure 14. The first cycles for 0.3 $Mg(TFSI)_2$ in glyme/diglyme are shown for cyclic voltammograms taken in a 3-electrode configuration where the working electrode was the independent variable. FTO glass exhibits the best stability up to ~2.1 V vs. carbon (~4.6 V vs. Mg/Mg^{2+}).

Table 6. The compiled results for 8 different combinations of current collector and electrolyte after the 1st and 5th cycles recorded at 200 mV s^{-1}. For both electrolytes FTO glass demonstrates the highest stability.

		Electrolyte Breakdown Voltage (V vs. Carbon)			
Electrolyte	**Cycle Number**	**Pt foil**	**Ni foil**	**FTO glass**	**Stainless Steel**
$Mg(TFSI)_2$ // glyme/diglyme	1	1.3	1.2	2.1	1.1
	5	1.0	0.8	2.1	1.6
APC // THF	1	0.7	0.4	1.0	0.7
	5	0.7	0.7	1.5	-0.3

This result gives us confidence that FTO glass may serve as a reliable substrate for magnesium battery cathode studies because it will not corrode like stainless steel or undergo other side reactions that make interpretation of electrochemical results more complicated. Lastly,

thin films of the vanadium oxide annealed on FTO glass were used as a cathode material for preliminary screening for electrochemical activity. Thin films have been used previously in the literature[158,165] and may serve as an excellent platform for studying fundamental reaction mechanisms and failure modes without the influence of carbon additives used in coin cells. Such additives may reduce the stability of the electrolyte[166] and will need to be addressed in the future but this is not the main goal of research at this preliminary stage. Besides good electrochemical performance, this configuration is easy to fabricate via dropcasting or electrodepositing material onto the glass, and easy to transport for XRD, XPS, and other kinds of materials characterization before and after electrochemical testing.

Results from TGA and XRD for the $V_2O_5 \cdot nH_2O$ gave inconclusive results for the sample annealed at 240°C (Figure 15a and b). The water content from TGA suggests that $n \sim 0.5$ at 240°C, while XRD showed that the transition from the xerogel (~11.7 Å layered spacing) back into orthorhombic V_2O_5 (~4.34 Å) occurs somewhere between 120 and 240°C. This discrepancy is not uncommon based on other literature results,[165,167] but will be worth revisiting in more depth later and may be a consequence of the different heating environment between the TGA and the furnace annealing steps.

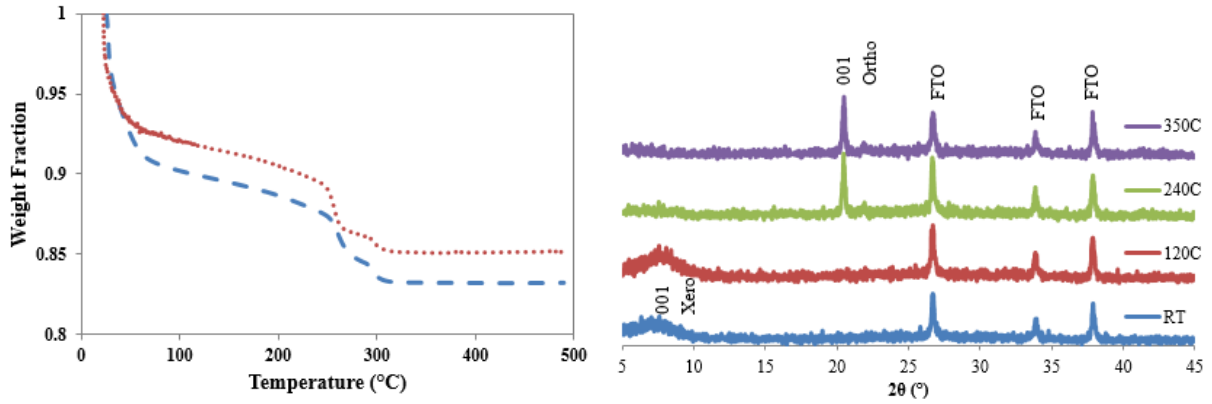

Figure 15. a) Duplicate TGA results for dried V_2O_5 xerogel annealed at 240°C for 3 hours. The ramp rate (5°C/min and the temperature range was 0-500°C b) XRD patterns for xerogels annealed at room temperature (ambient, blue), 120 (red), 240 (green) and 350 °C (purple).

Although full electrochemical and materials characterization is not complete, initial results show the importance of the electrode-electrolyte interface (Figure 16). Whereas conventional wisdom suggests that slow solid-state diffusion limits cathode performance, this result shows that the same material may show completely different electrochemical responses in different electrolytes. Since many cathode studies are performed with only one electrolyte, it is easy to envision the possibility that a perfectly good cathode material may have been tested with an electrolyte that does not support Mg electrochemistry. This intuition is supported by one of the few studies on the cathode surface for Mo_6S_8.[133] Fast kinetics are attributed to this material (Chevrel phase) in APC because of its low desolvation energy moderated by Mo-Cl-Mg bonds. In contrast, oxides do not have low-energy surfaces that show exposed V or other metal sites and do not benefit from this same mechanism. Although this result is only preliminary, it provides guidance for future studies of cathode materials.

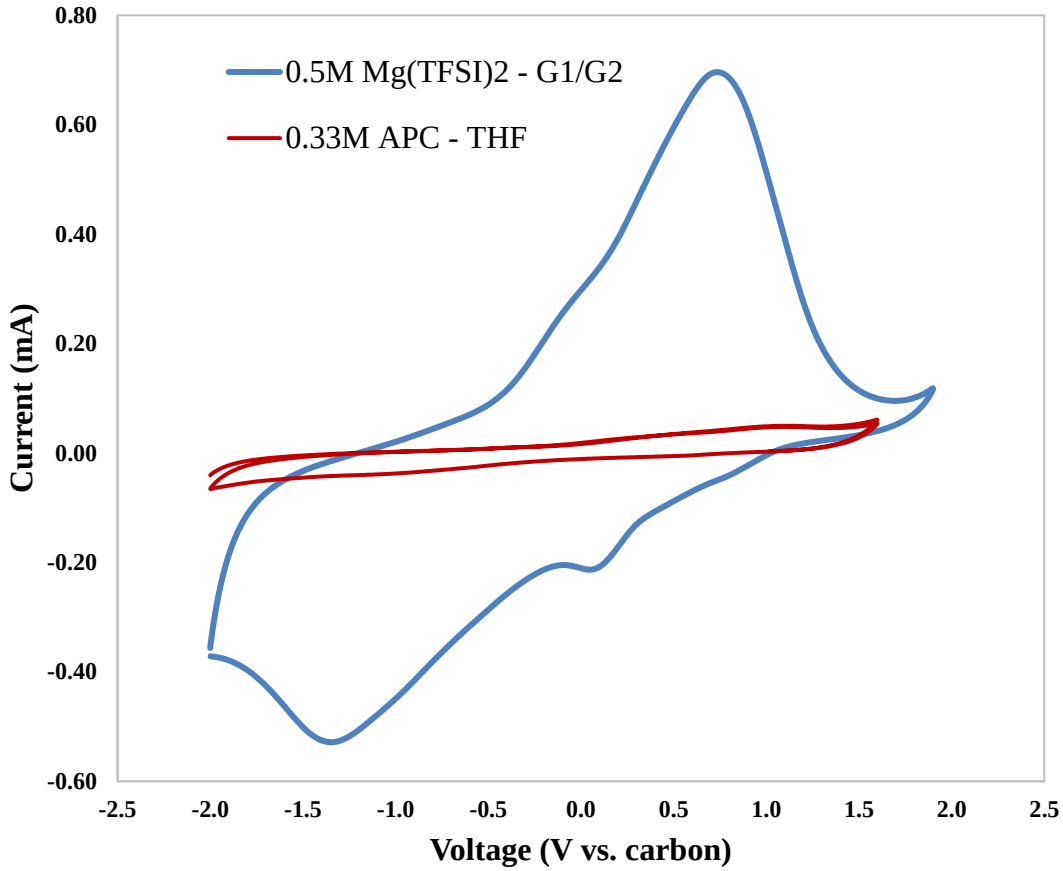

Figure 16. No electrochemical activity is observed for vanadium oxide using APC as the electrolyte, but cyclic voltammograms of the same material in $Mg(TFSI)_2$//glyme/diglyme shows redox peaks consistent with intercalation.

3.4. Conclusions

Preliminary electrochemical studies have demonstrated the advantages of a well-designed three-electrode setup over standard two-electrode coin cell configurations for Mg battery studies. Going against common operating procedures, we have identified carbon felt as a robust alternative to magnesium metal foil at both the reference electrode and the counter electrode. We also show that FTO glass shows higher stability than any of the most common current collectors for magnesium electrochemical tests – even platinum. Coating thin films on this inexpensive glass is a good platform for both electrochemical and future materials characterization. Lastly,

we show that the cathode-electrolyte interface offers a rich opportunity for studying cathode materials once it is understood that limitation to diffusion alone cannot be responsible for the poor performance of magnesium cathode materials to date.

Chapter 4. Implications for Future Research on Magnesium Batteries

These results provide avenues to make progress at both the cathode-electrolyte and anode-electrolyte interfaces. Here the goal is to streamline our current electrochemical setup so that we not only have infrastructure and protocols that work but also the understanding behind why our setup works.

4.1. A Reliable Mg Quasi-Reference Electrode

At the anode, we will work to improve the understanding of the MgF_2 coating. The growing body of work on Mg^{2+}-conductive coatings[77,95] demonstrates that the magnesium SEI layer need not be as detrimentally passivating as once believed. Between our results[94] and other recent publications,[78,114] there appears to be something special about magnesium halides in particular as ionic conductors that has gone unobserved until the past few years. However, our results contradict the Aurbach group's understanding of MgF_2 as an insulator[62,63] and will likely require more work to resolve this discrepancy to the community's satisfaction.

Regardless, a theme in many reports is that deliberate care is often not taken in the design of the Mg-electrolyte interphase layer, and as a consequence it is generally inappropriate to use untreated magnesium as a reference electrode because the surface reactions are not well characterized or characterizable (Figure 12).[125] A reliable reference electrode must have a well-known potential that is stable over time. In addition, it should be non-polarizable (i.e. its potential does not change as current is passed through it), especially when tests are performed using 2-electrode cells like coin cells. By combining this insight from our cathode screening setup with the results from symmetric cell test of MgF_2-coated magnesium (Figure 5b-d), it may be possible to determine if the coated Mg metal is a suitable quasi-reference electrode.

The low overpotential and high reversibility of the coated metal foil suggests that it could be a good reference electrode for magnesium studies. There has not been a thorough analysis of

magnesium reference electrodes to date, so by extending this work could be the first to characterize a reliable reference electrode for magnesium. On top of this, MgI_2 is under consideration as an alternative to using MgF_2 (and dangerous HF solutions).[78] By characterizing both Mg halide coatings, it may be possible to determine if either coating is privileged as a reference electrode or if these coatings in general make magnesium electrochemistry consistently more reliable.

In fact, the dearth of reliable reference electrodes is not unique to Mg, and plagues other non-Li battery technologies.[125,168] If successful, our study could then be generalizable to other systems such as Ca or Na batteries and have significant impact on the subfield of nonaqueous electrochemistry.

4.2. Systematic Electrochemical Screening of Magnesium Battery Cathode Materials

With or without the successful development of magnesium-based reference electrodes, we have developed a simple setup for electrochemically screening prospective magnesium battery cathode materials. Its key features include 1) a simple design based on 3-electrode beaker cells, 2) a wide operating voltage range thanks to the FTO current collector and $Mg(TFSI)_2$-based electrolyte, 3) compatibility with electrolytes that don't require complicated organometallic syntheses, 4) reliable voltage measurements based on the activated carbon quasi-reference electrode, and 5) rapid preliminary screening of surface compatibility using multiple electrolytes. Taken together, these features circumvent known problems in magnesium battery experiments and results.

To make this a more compelling publication, it is worth proving that our setup reproduces the results of other well-characterized materials such as V_2O_5[158] and Mo_6S_8.[53] More thorough electrochemical analysis (e.g. cycling at different rates) is required here, and follow-on characterization of the electronic and crystal structure should be applied (e.g. XRD, XPS, XAFS

and other spectroscopy or microscopy techniques as appropriate) on order to guide further development and improvements of "hits" that come from the screening of cathode materials. Two important variables that have not been thoroughly investigated and controlled for are the effects of trace water[169] and $MgCl_2$ as an additive,[83] both of which are known to have significant impact on magnesium electrochemistry.

This will serve as a template, both for screening new magnesium battery cathode materials, but also for re-evaluating materials that may have simply performed poorly based on faulty assumptions of the electrochemical system.

4.3. Development of Positive Electrodes for Magnesium Batteries via Defect Engineering

Once the infrastructure and electrochemical understanding has been fully developed and promising materials are identified for further research, this opens lines of inquiry that are more traditional to the Cao lab. Two examples include how growing different facets or controlling defects change the surface energy and performance of sodium- and lithium-ion battery cathode materials.[170,171]

Insofar as cathode-electrolyte compatibility has masked the true performance of cathode materials,[133] the development of new coatings or introducing surface defects may help catalyze the desolvation of Mg^{2+} at the cathode surface (and MgF_2 has been suggested as a potential candidate for this role as well[115]).

Further, bulk doping of F into MoO_3 has been shown to be another strategy to improve cathode performance.[172,173] The authors attribute this to the modulation of the crystal structure and reducing the barrier to Mg^{2+} diffusion in the host material. Dopants and/or materials that possess greater hybridization between the metal center *d* orbitals and the ligand *p* orbitals are

also believed to help increase electronic conductivity and bear the burden of absorbing the divalent charge of Mg upon intercalation.[174,175]

If the improved interfacial understanding has limitations and diffusion remains the biggest issue (of which I am not convinced), there are design rules we can turn to for addressing the slow solid-state diffusion.[176] Other familiar techniques include nanosizing the cathode material, as shown in the case of several magnesium sulfides,[177] and modulating the interlayer spacing of layered materials, such as vanadium oxide xerogels.[165] This snapshot provides myriad opportunities for fine-tuning prospective cathode materials that pass muster at the screening stage.

4.4. Against "Sluggish Diffusion"

Our results have highlighted the twin possibilities that a) many magnesium battery cathodes have been tested under anodically limited conditions and b) the poor performance of certain cathode materials may be artificially masked by the inappropriate choice of electrolyte. Both cast doubt on the assertion that "sluggish diffusion" (owing to greater electrostatic forces from Mg^{2+}) accounts for the poor performance of magnesium cathode materials. Other times, researchers hedge by referring to "sluggish kinetics" which is technically true but imprecise as far as the source of this effect. In any case, slow solid-state diffusion is taken at face value in many magnesium battery papers.

A growing body of work already shows that this is an incomplete understanding. For example, desolvation energy is going to play a much larger role as a potential rate-limiting step for Mg than analogous Li batteries.[146,178] Since 2009, the Aurbach group has argued that solid-state diffusion alone cannot account for the poor performance.[137] Instead, the cathode's ability to defray the additional strain on the crystal or electronic structure from adding or removing two

electrons per Mg ion appears to be a better explanation for the good performance of Mo_6S_8 and the poor performance of others.

On top of this, we have shown that V_2O_5 is compatible with $Mg(TFSI)_2$ in glyme-based solvents, but not compatible with APC in THF. The Aurbach group has found the exact opposite to be the case with Mo6S8 – it functions with APC as the electrolyte but not $Mg(TFSI)_2$.[179] In another instance, changing the solvent affected the performance of a Mn_2O_3 electrode with APC as the electrolyte.[180] Using tetraglyme as the solvent lead to a fraction of the capacity obtained when dimethyl ether (glyme) was used in the APC electrolyte, pointing to the importance of removing the coordination shell for Mg electrochemical activity.

In another context, both the chevrel phase (Mo_6S_8) and MoO_3[133,181] performed differently based on how the Mo metal center interacts with Mg at the surface, which in turn has its own complicated bonding with salts and solvents in the electrolyte. In particular, Mo in the chevrel phase helps to catalyze the removal of Cl^- counter ions bonded to the Mg_xCl_y monomers and dimers in solution, whereas $Mg(TFSI)^+$ is easier to pull apart at the MoO_3 surface than $MgCl^+$. There are many more such examples where researchers have observed different electrolytes offer different performance with the same material, but do not seem to draw the conclusion that cathode-electrolyte interfacial issues may have greater significance than slow solid-state diffusion alone.

Although it may be a Sisyphean task trying to get around this mental inertia,[182] I believe it would be worth summarizing our findings and the findings of others to explicitly make the appeal to consider surface processes rather than bulk diffusion as the rate-limiting step for magnesium battery cathode research.

4.5. Towards High Energy Full-Cell Magnesium Batteries

In the longer term, it is conceivable that a suitable anode (likely with some kind of coating), simple electrolyte (likely based on $Mg(TFSI)_2$ or other simple salts), and cathode material could be found and optimized to work harmoniously together. Additional characterization would be required to move from the 3-electrode beaker cells used so far to (reliable) coin cell tests or another custom-designed cell configuration. At this point, magnesium battery materials research would begin to resemble that of today's well-established Li-ion protocols in order to boost the energy density, power density, and longevity of such cells for commercial applications. This remains a long way off, but our hope is that this work plays a part in the relay race toward practical magnesium batteries.

Chapter 5. Battery Data Analytics for Electric Aircraft

5.1. Introduction

As battery costs continue to drop and new battery-enabled technologies are brought to market, an ever-increasing amount of data is generated. A common refrain is that "data is the new oil," in that it is an abundant resource that can enable rapid technological development, but must also be refined before it becomes valuable. This is especially true for the battery industry, which is inherently multidisciplinary, leading to datasets that are generally not opening available and offer low interoperability. Battery data science encompasses many scales and applications, ranging from density functional theory, physics-based modelling to managing and maintaining MWh battery systems in the field. Here we constrain our focus to data engineering and data-driven modelling (i.e. machine learning) to forecast health, specifically in the nascent application of electrified flight.

The emerging electric aviation industry is drawing attention from both defense and private industry. The use of distributed electric propulsion technology will revolutionize the future of military operations, relief and humanitarian operations, and benefit the US economy as a whole. The benefits of electric aviation include lower operation and maintenance costs, environmental sustainability, and freedom to operate without runways when vertical take-off and landing (VTOL) capability is employed.

The development and assessment of energy storage systems is critical for this new environment. In contrast with automotive electrification, the aerospace and aviation markets demand higher performance and more stringent safety requirements. The standard operating procedures for electric aviation have not yet been defined, and there are gaps in understanding of battery safety and reliability as these systems age. This poses major challenges both for the

certification agencies who must define these new safety standards or procedures, and the manufacturers who must implement these new processes.

In order to address this challenge, significant investments in telemetry and battery systems have been made, but the value of that data has not yet been realized. In the following chapters we report our approach to develop the data infrastructure necessary to extract insights and value from raw data across the life cycle of the battery, from initial R&D and acceptance testing all the way through operations and eventual end-of-life (EOL) decommissioning (Figure 17). By combining cell-level understanding of battery health with state-of-the-art machine learning methods, this will help inform the development of new SOPs for battery pack manufacturing, in-flight operations, routine maintenance, and EOL determination.

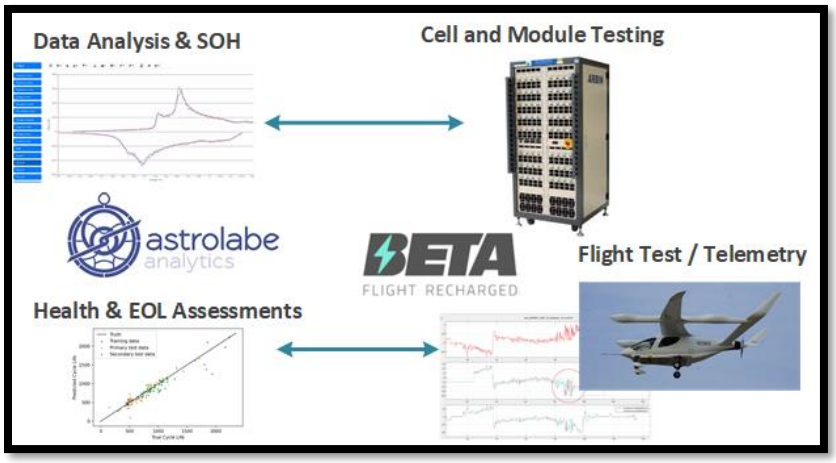

Figure 17. The goal of this proposed project is to combine battery analytics with R&D and operations data from EVTOL startup Beta Technologies to bring safety and high performance to electric aviation.

5.2. Model Development with Machine Learning

This section outlines the typical process for developing a model with machine learning (ML) methods. Like the scientific method is the gold standard for scientific hypothesis testing, there are established procedures and accepted norms for applying ML to a new problem. The first step requires the goals of the model and the project to be defined. The type of model is defined based

on the desired output and input data. Once the model has been selected, the data that is available for developing the model is inspected and divided into different data sets. Some data is used for model training and validation, while other data is withheld from the model development procedure altogether. The training and validation data sets are used to develop *features*, which are the input data to the model, using a variety of domain-specific and data-specific data exploration methods. The features are then used to train and tune the selected model(s) with the primary objective of optimizing the model's quantifiable performance. Finally, the optimal model is applied to the withheld data to see if the model continues to perform well on new data. Each of these steps is described in further detail in the remainder of this section.

5.2.1. Model Selection

ML models are a class of algorithms that self-optimize and improve their performance based through *experience*. Typically, experience comes in the form of data. Data generally consists of a vector of values, $\boldsymbol{x}$, corresponding to a single sample. The model takes the data, applies a transformation to the data, and provides an output, $\boldsymbol{y}$, also called the *outcome variable*, which may be a scalar or a vector. Generally, as the number of samples increases (i.e. the size of the data set increases) the model's performance increases.

In general, two types of ML algorithms exist. They are *unsupervised learning* and *supervised learning*. The distinguishing feature between these two approaches is the type of data used for model development. In supervised learning, each sample in the data set includes the correct desired output (i.e. both $\boldsymbol{x}$ and $\boldsymbol{y}$ are known). In unsupervised learning, the output ($\boldsymbol{y}$) is not known at the time of the training. Supervised learning typically performs much better than unsupervised learning, and is used in the ML algorithms in this work. Two common types of algorithms in supervised learning are regression and classification. Note: this section is *not*

exhaustive; other partially-supervised and reinforcement learning approaches exist and are not included here.

5.2.2. Regression & Classification Problems

Supervised learning algorithms include regression, neural networks, support vector machines, and classification. Regression, neural networks, and classification algorithms are used in this work. Regression algorithms use the input features, $\boldsymbol{x}$, to estimate a *numerical value*. Classification algorithms estimate the probability that the sample belongs to a specific category (i.e. values between 0 and 1). Neural networks can be used for classification or regression.

The first step to developing a model is deciding whether a classification or regression algorithm is appropriate. Classification models can be developed with very high accuracy if binning samples into different categories is the most important aspect and are scored in a very straightforward manner. Accuracy of classification algorithms is based on whether the algorithm correctly labels a sample into the correct category. Regression analysis, by contrast, is useful when a specific number is desired, but is generally more difficult to quantify. Regression models are scored using a predefined *loss function*, though *auxiliary score functions* may also be used to quantify their performance. The loss function is used as a guide against which the model is optimized; parameters in the models are tweaked to minimize the value of the loss function.

Once an algorithm has been selected, the data must be prepared for model development.

It is critical to point out that the available dataset must be divided into three separate groups (at least). The three groups are: training, validation, and test data sets. The training and validation data are actively used in the model development process, while the test data set is withheld completely until the model has been completely developed. This allows the model to be scored on data that the model has never seen before, and data that was not used to develop the model. Ideally, a random split of all the data is used to generate the three groups.

5.2.3. Data Exploration and Feature Development

Data exploration is an extremely important stage for developing a ML model. When a ML model is developed from scratch, or new features are developed, this stage can take a significant amount of time, effort, domain-specific knowledge, and ingenuity. During the data exploration phase, a variety of different features are developed. Note that during the data exploration phase, ideally the training data is used for developing features. In low-data situations, the validation data may also be used.

Recall that the input features, $\boldsymbol{x}$, are the inputs to the ML algorithm. During this phase, we aim to generate features that exhibit correlation, or *covariance,* with the desired output values, or outcome variable(s). In general, there may be some linear or nonlinear relationship between the raw, unprocessed data and the desired outcome variables. During the data exploration phase, the raw data must be transformed into features that (ideally) correlate strongly with the outcome variable to empower the ML algorithms.

5.2.4. Training and Tuning the Model

Once features have been developed and exploration has been completed, the model is trained with the training and validation data sets. The training data is used to optimize the model while the validation data is used to automatically tune the training hyperparameters. Overall, an optimal model is produced given the input features using the data in the training and validation data sets. Again, test data is *never* used during training or for guiding the model development. When the model is completely trained, a variety of plotting approaches can be employed to visualize the model's performance. In some situations, it can be beneficial to review the results and inspect major outliers (where the model fails). The outliers may either be due to failure in the data processing pipeline where features are generated incorrectly or show a parameter subspace where the model starts to fail. These are helpful insights for guiding the training and tuning

process, fixing feature generation code, and identifying areas where a new model may be required.

5.2.5. Inspect Test Data Results

Once the model has desirable performance with the training and validation data, the model can be tested on the test data. The test data represents the closest thing to ‘new’ data that the model could see, since it was not present during the training or feature development process. It is common to show the performance of the model on training, validation, and test data sets.

Chapter 6. A User-Friendly Environment for Battery Data Science

6.1. Introduction

It is well understood that electrochemical energy storage using batteries represents a space prime for innovation. However, one of several bottlenecks for the commercialization of new battery technology is at the level of battery research and development. Teams of battery scientists, engineers, and technicians are faced with an array of data management challenges as they test battery performance. Labs may test hundreds or thousands of cells in parallel, with each cell generating megabytes or gigabytes of data, depending on the nature and duration of the test.

As a given battery lab grows, routine data analysis becomes onerous. Different pieces of hardware are accompanied by proprietary software and mutually incompatible data formats that does not scale well over time. Furthermore, while R&D teams are composed of chemists, material scientists, or other engineers, expertise around software development, IT, or data science often falls outside a team's core competencies. As a result, battery engineering teams often lose 25% of their time on rote data management and analysis chores using fragile legacy software solutions. This problem is extant across all stages of the battery value chain - from when raw materials are refined to assembly into electrodes and other subcomponents, all the way through field deployment and commissioning.

This lack of standardization slows down individual researchers, their team's project timelines, and any collaboration between groups. While MS Excel VBA macros are still commonplace, a growing body of software tools and solutions have been developed that each address different aspects of this problem space. This includes, inter alia, commercial software from Voltaiq,[183] the Battery evaluation and early prediction software package (BEEP),[184] the Dahn research group's Universal Battery Database,[185] *cellpy* developed by researchers at IFE Norway,[186] Battery Archive,[187] and Galvanalyser.[188] Preliminary concepts for a battery data

genome have also been proposed to help develop best practices for working with and sharing data.[61]

Here we report a suite of workflow tools for battery researchers to lay the foundation for future battery infrastructure and innovation. The platform integrates with major hardware vendors to extract data from installed hardware and load it into a cloud database. A second effort incorporates analytics for routine data visualization, dashboarding and reporting using a web application to save time and provide greater visibility for battery data stakeholders into their testing data. Third, we employ Jupyter Notebooks[189] as a web-based API for custom scripting and an environment for battery data science. The platform promises to accelerate battery R&D and shave significant time off product development efforts.

6.2. Technical Details

This platform is designed to simplify data management for companies across the battery value chain:

1. It streamlines data cleaning, the most tedious in any data analysis project. By integrating our cloud-based software with the hardware installed on-site, we automatically port raw test data into a unified and useful format for analysis.
2. It provides advanced data visualization and analytics tools. Hours of analysis can be done in minutes or seconds to generate standard plots and statistics for cell capacity, voltage profiles, as well as more involved analyses like incremental capacity[190] or other user-defined functions. Templates for standard battery performance metrics can be generated with a few clicks, and more advanced analyses that were previously time-prohibitive are now built-in functions. This is particularly important for battery developers where thousands of battery cells may be tested simultaneously, each being cycled thousands of times.

3. It provides an API for custom analysis and reporting. Our reporting tools provide templates that automatically generate reports that are meaningful to executives, investors, and other non-scientists.

6.2.1. Data ingestion

The breadth of different hardware vendors and file formats for battery testers and potentiostats leaves plenty of room for standardization. The first task of the system is to take in data from disparate sources and collate it into a common data structure. To date, the set of supported hardware and file types are shown in Table 7.

Table 7. The platform currently supports datasets from the following hardware vendors in the specified file formats. *Note that many vendors have many different software versions that have been deployed over time, and not every such version may be supported yet.

Hardware Vendor	**Supported File Formats***
Admiral Instruments	Excel, .txt
Arbin Instruments	.csv, Excel, .res
Basytec	.txt
Biologic	.mpr, .mpt
Land/Landt	Excel
Maccor	.csv, Excel, .001 (CSV with channel as file extension)
Neware	Excel, .nda
Novonix	.csv
Versastat	.par

Data may be uploaded in two ways: a) by uploading discrete sets of files using the web interface (Figure 18), or 2) by downloading a tool to automatically monitor a given local directory and uploading the test data in that folder (Figure 19). The automatic process can be set to ingest new data on a schedule specified by the user in the case of tests that are actively running (e.g. once every morning at 5am). This client-side application uses the .NET WinForms library.

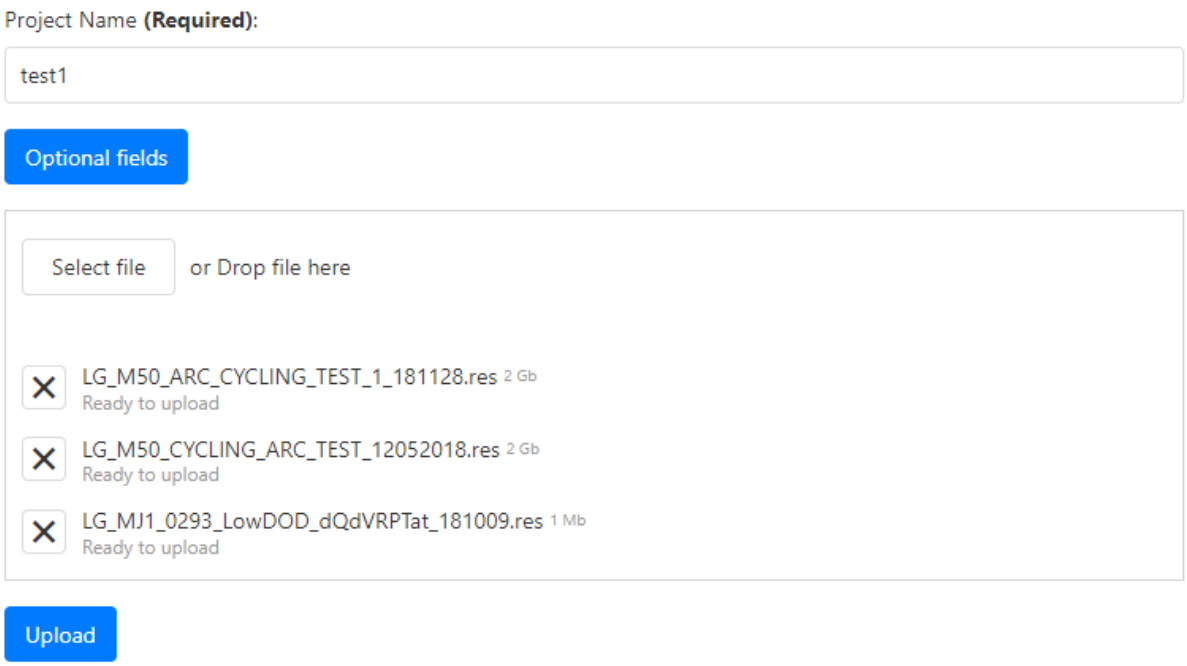

Figure 18. Example screenshot of three Arbin .res files being uploaded.

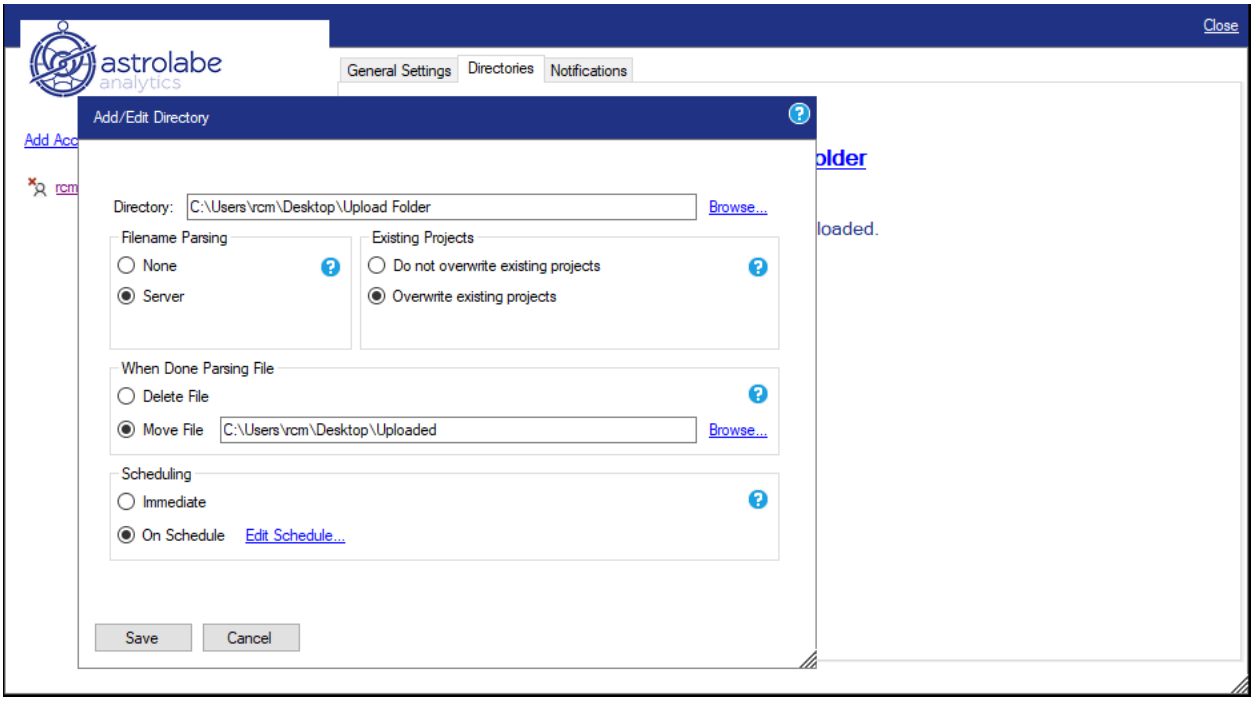

Figure 19. User interface for the automatic upload process.

6.2.2. Database Server

The next component of the system is the database, which is SQL Server 2017. The actual files that are uploaded get stored using Amazon Web Services' Simple Storage Service (AWS S3). A configurable retention period is used to delete previous versions of files older than 365 days to avoid using up S3 space.

Web browsers accessing the web app form another client-server connection. The web app runs Angular 11 in the browser and ASP.NET on the server. The server exposes most of the data and functionality using either a RESTful API or via OData. The web app connects to the database server over SSL.

Sharding has been implemented to enable scale out, which plays a role in how the data is structured. For battery testing data, the master node in the sharding implementation holds the following primary tables:

***Projects*:** Holds project metadata. A row in this table represents the data for one test channel. Some file formats contain multiple channels for a single file, so there will be multiple rows created in those situations. Most metadata can be modified by the user via the web app. Examples of the metadata that can be stored here include the filename, file size, number of cycles, active material loading, and other relevant data. See Appendix for further details.

***ProjectTags*:** Allows the users to attach their own arbitrary additional metadata to the project. This is essentially a key/value table that has a relation to the project row that it is connected to. Columns are:

Id
Name
Value
ProjectId

The shard nodes contain the actual data. There are only three tables in our shards:

***DataPoints*:** This is the raw time series data. Based on how different hardware handles data logging and acquisition, not all file formats have data for every column in this table, although we calculate those values when possible. Columns include:

Id
Capacity
Current
CycleIndex
CycleStep
Energy
Index
Power
ProjectId
Temperature
Time
Voltage
StepIndex
WallTime

Resistance

***Cycles*:** This table contains pre-computed cycle statistics generated from the DataPoint data parsed from the file. This is generated as part of file parsing. Columns include such data as (dis)charge capacity, energy, and power and their statistics (e.g. maximum or minimum power).

6.2.3. Web Application

Detailing every feature of the web app is beyond the scope of this report, but there are a few key operations. Specific usage examples will be given in the next section on Example Use Cases.

Upload: As mentioned above (Figure 18), this is the intake of data. The user selects one or more files for upload. The files must have an expected file extension (Table 7), and a Name is a required field. Other metadata fields are available for entry as well as ability to specify permissions. Files are split into chunks to accommodate large file uploads. These chunks are uploaded to a REST endpoint. Once all chunks are uploaded, each file gets a job assigned to it to parse the data and store in the database. Jobs are executed with a tool called Hangfire.

***Project List**:* This shows a list of projects the user has uploaded and available. The list is retrieved from various OData endpoints depending on what list is being viewed. An example of this GUI is shown in Figure 20. Items in black have been uploaded and processed, whereas grey text means that it is currently being processed, and red text means that an error has occurred (for instance in the case of data that does not fit a recognized format).

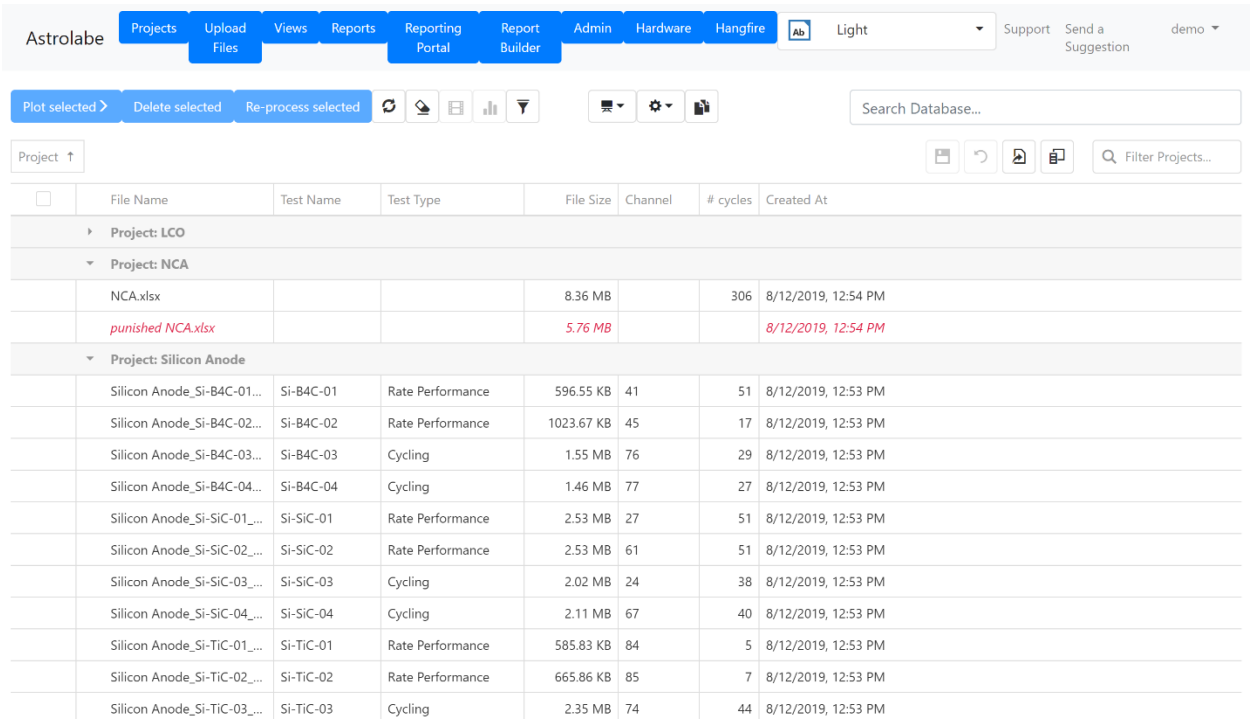

Figure 20. Screenshot of the homepage for selecting data for further analysis.

***Plotting*:** Once one or more projects are selected, they can be plotted. The basic built-in functionality allows users to select an independent variable for the x-axis from a dropdown menu (e.g. cycle number, or capacity, or time), and then select up to two dependent variables for the y-axes (e.g. for plotting capacity and coulombic efficiency vs. cycle number, Figure 21).

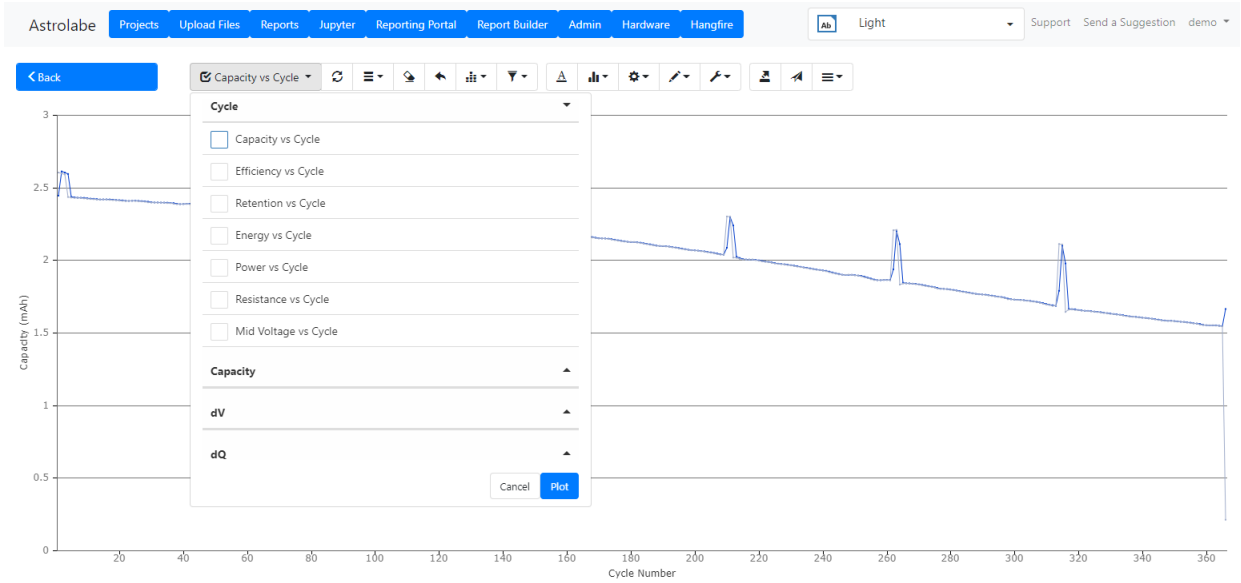

Figure 21. Example screenshot plotting cycling statistics.

The client sends the list of projects along with information about which plot is requested as well as parameters for the plot. Other parameters may have already been stored as defaults on the server side. Using all these parameters, the server sends back data points that are then plotted using CanvasJS.

It is worth noting that many different projects are used to provide functionality in the web app, although the client side uses DevExtreme GUI components and CanvasJS for chart generation.

Users can belong (optionally) to one or more Organizations, which are essentially groups of users. Users may assign projects to an Organization for sharing across a given team, or from their organization to a downstream data stakeholder.

6.2.4. Jupyter Notebook

Jupyter Notebook comes equipped with kernels for several different languages without installing anything. This allows power users to put together custom scripts and analytics for use cases that are not built-in to the core webapp. Users can query the database using the

project_search library. These queries return Pandas DataFrames (Figure 22). This API also keeps our database structure, and more specifically the querying of data cross database shards agnostic. That is, users can specify certain projects and then additionally specify whether or not to include time series data (query.includeDataPointData()), cycle statistics (query.includeCycles()), and/or other custom metadata about a given project query.includeProjectTags()).

Users will find the standard set of scientific computing libraries preinstalled (such as NumPy,[191] SciPy,[192] Matplotlib,[193] scikit-learn,[194] and pandas[195]), as well as libraries for advanced visualizations (Altair[196]), and battery-specific tools such as cellpy[186] and Pybamm.[197] We are interested in collaborating with the wider community to establish best practices and interoperable tools and solutions for data pipelining, data-driven modeling and other applications based on this work to date.

Jupyter (via Jupyterhub functionality) is distinct from web app functionality. The only link there is that the web app is used to provide authentication information to Jupyter, specifically, to which Organizations a user belongs.

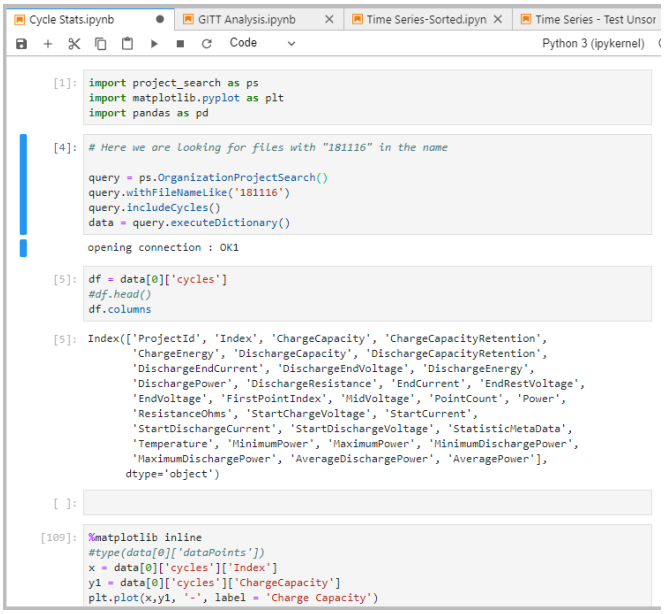

Figure 22. Screenshot of Jupyter Notebook interface and sample query using the project_search library.

6.3. Example Use Cases

While this is not intended as the full documentation for the software, a few illustrative use cases are presented here.

6.3.1. Getting started

A preliminary video tutorial for new user registration, uploading data, and basic plotting of cycling statistics, voltage profiles, and differential capacity plots is available from Ref. [198].

6.3.2. Templates for Generating Voltage Profiles

For frequently generated plotting, users may build a template that produces a reproducible output for a given plot. For example, users may select Voltage vs Capacity from the Templates dropdown menu and specify an interval or custom range of cycles to generate a re-usable template for voltage profiles (Figure 23). Additional optional settings for chart formatting are also available in this menu.

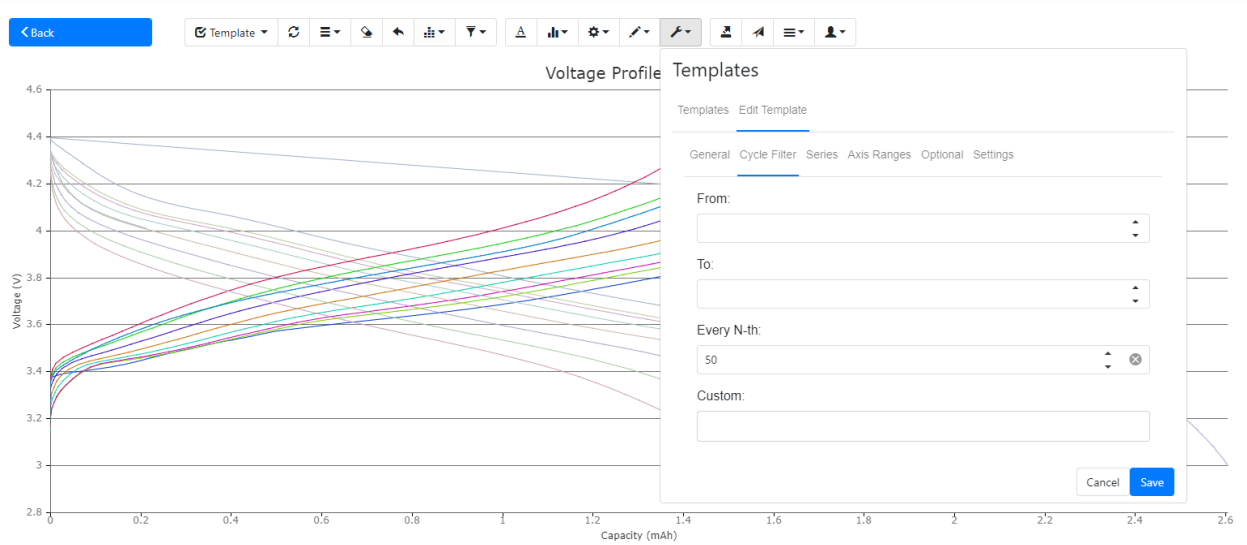

Figure 23. Example screenshot of the cycle selector tool used to generate a template for repeated analysis.

6.3.3. Differential Capacity Analysis

Differential capacity or incremental capacity analysis are diagnostics that have been identified as leading indicators of battery degradation.[190,199,200] By taking the numerical derivative of capacity stored (discharged) over a given voltage step size, peaks emerge that correspond to phase transformations that are characteristic to a given battery material chemistry. Over time and with cycling, peak intensity tends to go down as capacity decreases and peak position will change as the internal resistance and electrochemical overpotentials change (Figure 24). As such, this is a useful tool for battery health forecasting. For example, shifts in the potential where Li intercalates into graphite are known to emerge before capacity fade is noticeably affected.[201,202]

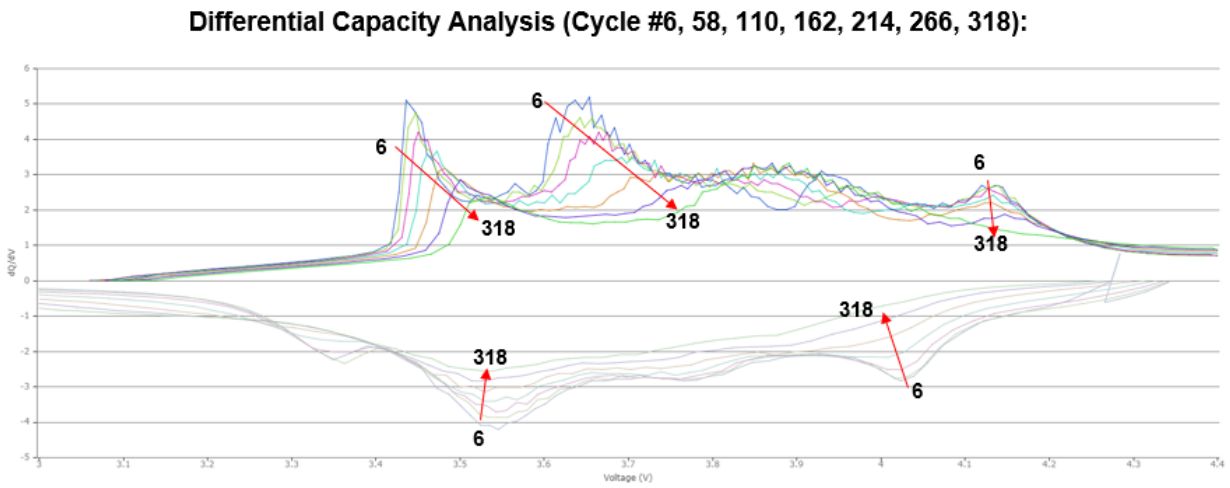

Figure 24. Advanced analyses such as differential capacity analysis can be used to resolve the evolution of electrochemical processes over time. Using built-in capabilities already deployed, we find peak position and intensity changes during cycling, suggesting an evolution in overpotential and loss of capacity.

6.3.4. Galvanostatic Intermittent Titration Technique (GITT)

The webapp provides functionality that covers many but not all routine battery data analysis applications. GITT is an example where Jupyter can be deployed to cover those applications not natively supported in the webapp, and give the user the ability to write and run custom scripts. Taking data from a GITT measurement made using a Maccor battery tester, a basic Jupyter Notebook document can be written to run the analysis and print the desired output (Figure 25).

Figure 25. a) A portion of the Python script and b) output figure generated for GITT analysis.

6.4. Conclusion

Modern software and data science tools allow for many new opportunities to better equip battery scientists and engineers. While battery modeling researchers are familiar with tools such as MATLAB and Python, many experimentalists do not have this background. Here we described a platform for battery data management and analysis that allows users to streamline data chores and more rapidly iterate on data-intensive projects and hypotheses.

This platform is a web-based application that consists of workflow tools to run the standard analyses familiar to any battery materials scientist or engineer, as well as an API based on Jupyter Notebook for more advanced custom analyses.

Our goal is to help grow an ecosystem of battery innovators that builds on the similar work of others in this community, with the objective of tightening the feedback loop between basic science at academic institutions and applied engineering that takes pace in industry to advance battery technology. We are eager to collaborate with others in the battery community to build on this work and help develop standards for battery data best practices.

Chapter 7. Battery Lifetime Forecasting for Cell Qualification and Validation Testing using Neural Networks

7.1. Introduction

As costs fall and energy density increases, lithium-ion batteries service a growing range of applications. However, battery safety and reliability remain challenges because of the wide range of duty cycles, operational environments, and manufacturing conditions these nonlinear electrochemical systems are subject to.

Accurately predicting battery lifetime is an active area of research and development across industry and academia.[203–205] Ensuring battery safety and performance is critical across all stages of battery development (from R&D, materials development, cell design and manufacturing) and end-use applications (consumer electronics, automotive, aerospace). Cell cycle life is a critical input for warranty design and plays a role in other product design and validation steps, such as cell qualification by a cell integrator, or for cell binning and grading, either at end-of-line testing for the cell OEM or by the customer during battery pack assembly. For a battery pack manufacturer, improved cycle life forecasting allows for grading cells without sole reliance on the cell OEM. This in turn allows the pack manufacturer to run a tighter quality control process that reduces cell-to-cell variation that hurts pack performance and reduces overall risk.

It is common practice in industry to develop a multidimensional model for battery performance and interpolate through lookup tables based on datasets generated over a wide enough range of test conditions. For example, cells may be tested across current steps such as 0.2C, 0.5C, 1C and 2C, temperature steps from -20°C, -10°C, 0°C, 20°C, and 40°C, and states of charge from 0 to 100% in 10% increments. Then once this model is developed for a given cell, the product developer can incorporate the expected duty cycle defined by application for accurate cycle life estimation. However, this is a expensive process that may take weeks or months to draw conclusions.

Others have published work on data-driven methods for battery cycle life prediction, most notably catalyzed by the work of Severson *et al.*[201] A recent report from the same group built on that work to study and optimize fast-charging protocols using the first 100 cycles of test data.[206] Another report used only the first 50 cycles to perform accurate predictions and developed the concept of knee onset (where capacity fade begins to accelerate), which is shown to predict and precede end-of-life.[207] An automated feature selection process has been used to find inputs for data-driven prediction with high accuracy, and found calendar aging and time spent in certain voltage ranges to be significant impacts on capacity fade.[208] A recurrent neural network that uses features derived from incremental capacity analysis (corresponding to degradation mechanisms) has been demonstrated for cells with lithium titanate as the anode and a blended NMC-LCO cathode.[209] Many other examples are available in the literature.

Using battery test data published in open repositories, we extend the model developed by Severson et al. to predict cell cycle life across a range of temperatures, C-rates, and industry-relevant chemistries. Using a neural network architecture, this model can be easily extended in the future to incorporate both new features and new data as both are made available to improve the accuracy of its forecast.

This work highlights the value of data-driven methods for solving industry-relevant problems, as well as the value that can be unlocked by making test data openly available to the wider battery community.

7.2. Preliminary Cell Lifetime Prediction

The first milestone of our NSF SBIR work focuses on reproducing state of the art cell life prediction algorithms.[201] The cited work focuses on developing novel ML features and applying the features to both a regression and classification model. The regression model aims to predict

the true cycle lifetime of a cell given cell cycling data from the first 100 charge-discharge cycles. The classification model aims to classify cells by whether they will last longer or shorter than 550 charge-discharge cycles using cycling data from the first 5 charge-discharge cycles.

7.2.1. Feature Development

In the cited work, three batches of batteries were tested. The first batch of batteries was used as the training data set, the second batch as the validation data set, and the final batch as the test data set. The training and validation data sets are used to develop features in the model. In our work, we focused on developing the features shown to correlate with the cycle life in the research paper. Details of these features and the experimental procedures necessary to generate the features are provided in

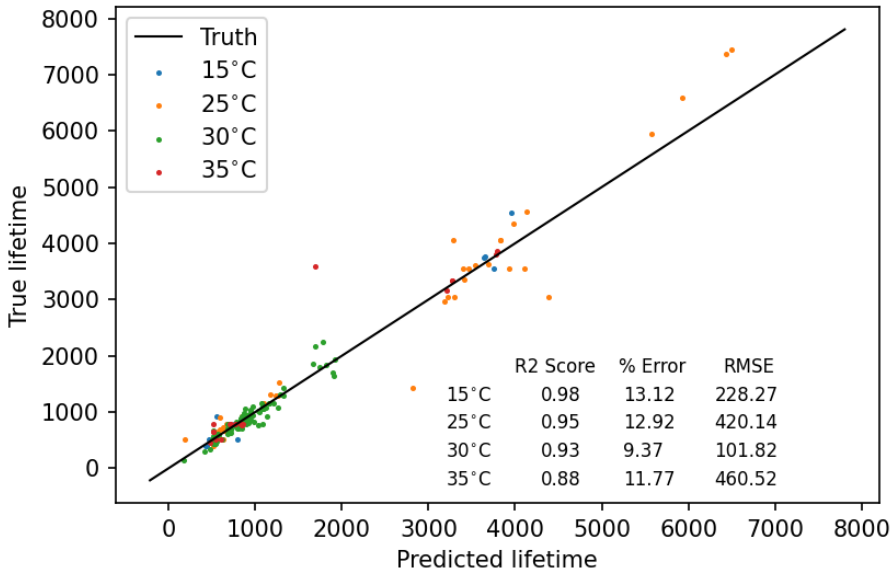

Figure 38. Performance metrics of the neural network with respect to different operating temperature.

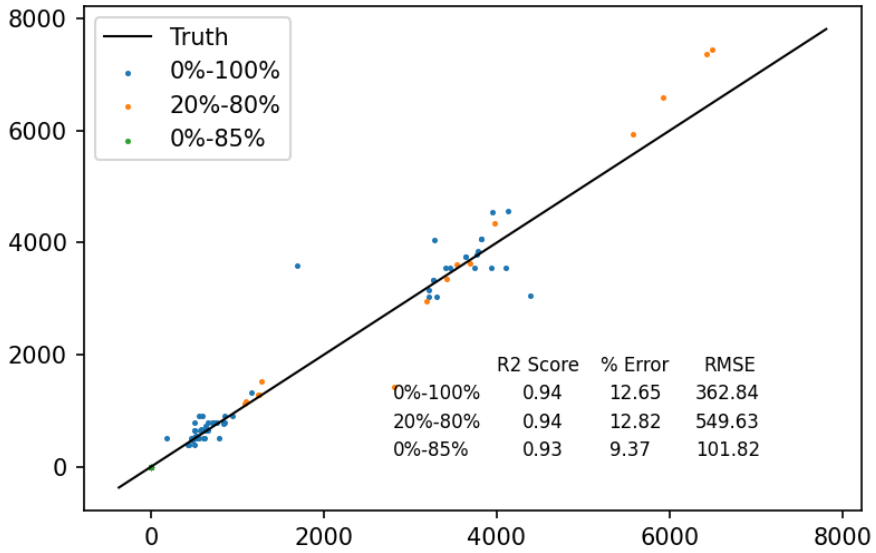

Figure 39. Performance metrics of the neural network with respect to different depths of discharge.

7.4.1. Model Features and Experimental Tests .

As previously mentioned, it is critically important to ensure that the features exhibit some correlation with the output variable. One of the steps in our development process is to generate the covariance plots, which are shown below in Figure 26.

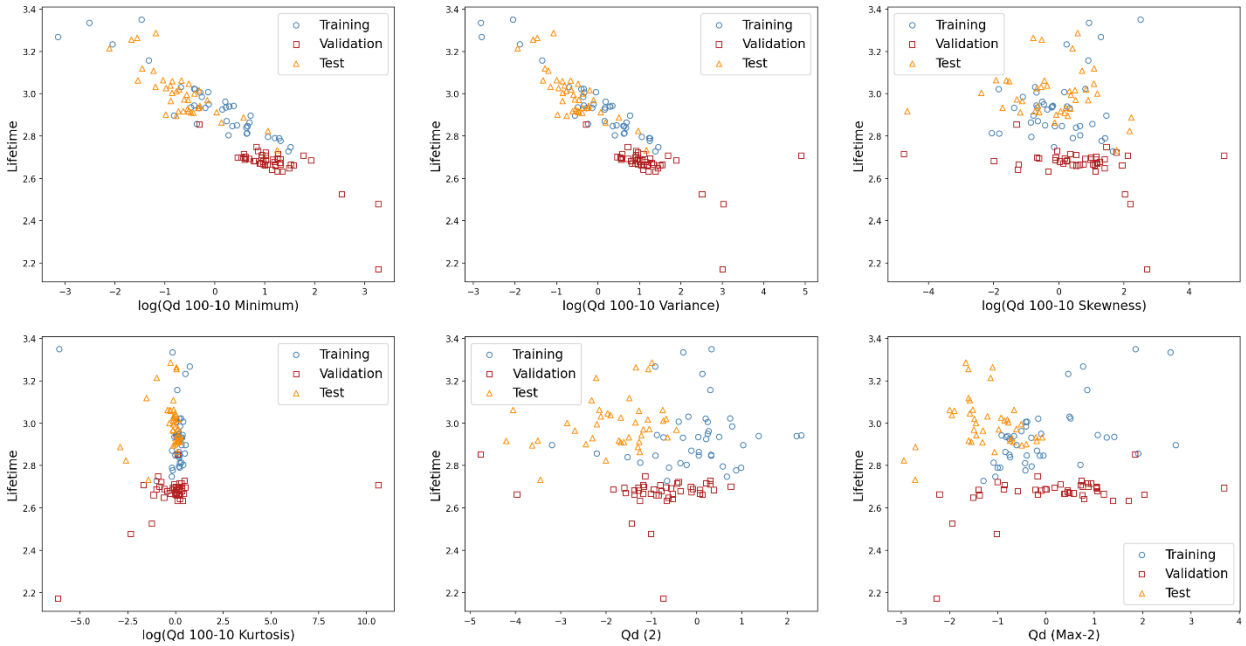

Figure 26. Features generated to train the regression models.

In each of these plots, the feature is plotted on the x-axis while the y-axis shows the cycle lifetime. It is evident that the first two features have strong correlation with the output variable. The other features exhibit lower correlation but prove useful for training the models. A fuller discussion of the significance of these features will be provided later.

7.2.2. Model Training

The regression model is trained using a regularized loss function for regression. The loss functions can be stated as:

$$\hat{\boldsymbol{\omega}} = argmin_{\boldsymbol{\omega}} \ \|\boldsymbol{y} - \boldsymbol{X}\boldsymbol{\omega}\|_2^2 + \lambda P(\boldsymbol{\omega})$$

$$P_{lasso}(\omega) = \|\boldsymbol{\omega}\|_1$$

$$P_{elastic}(\omega) = \frac{1-\alpha}{2}\|\boldsymbol{\omega}\|_2^2 + \alpha\,\|\boldsymbol{\omega}\|_1, \quad \alpha \in [0,1]$$

where ω is the vector of feature weights, or loadings.

The first term in the loss function is the *reconstruction loss*, which quantifies the difference between the predicted values and the true values. The second term in the loss function is the

regularization term. The regularization term is added to the loss function to minimize overfitting of the training data when training a model *and* impart other properties depending on the type of regularization employed. Two regularization strategies are employed in this work: lasso and elastic net. Both lasso and elastic net regularization strategies aim to achieve a property called *sparsity*, wherein only a subset of the original features are used to predict the outcome variable. This enables data scientists to find the best correlative features to use in combination to achieve a tradeoff between number of features and model performance. Furthermore, some studies have shown that sparse solutions often achieve equivalent or better performance and exhibit superior extrapolation to datasets with parameter and feature ranges that differ from the original training data set.

Classification algorithms generally use a logistic regression to estimate the likelihood of an output value given the input features. This classification optimization utilizes a standard log-loss loss function as implemented in Python's SciKit-Learn library. Similar to regression, regularization can be added to the loss function. In this case, only *l2* regularization is employed, which keeps the weighting of different features small.

7.2.3. Results

Three different types of models are produced for the regression approach. The three different types of models use different sets of features in the samples in the data set. The feature sets are *full, discharge, and variance*. In the full models, all of the correlated features are used for prediction. In the discharge models, only the features derived from the discharge curves are used, while in the variance model on the discharge curve variance feature is used. Classification models are developed for the full feature set and the variance-only feature set. The feature

details, including feature set descriptions, are provided in

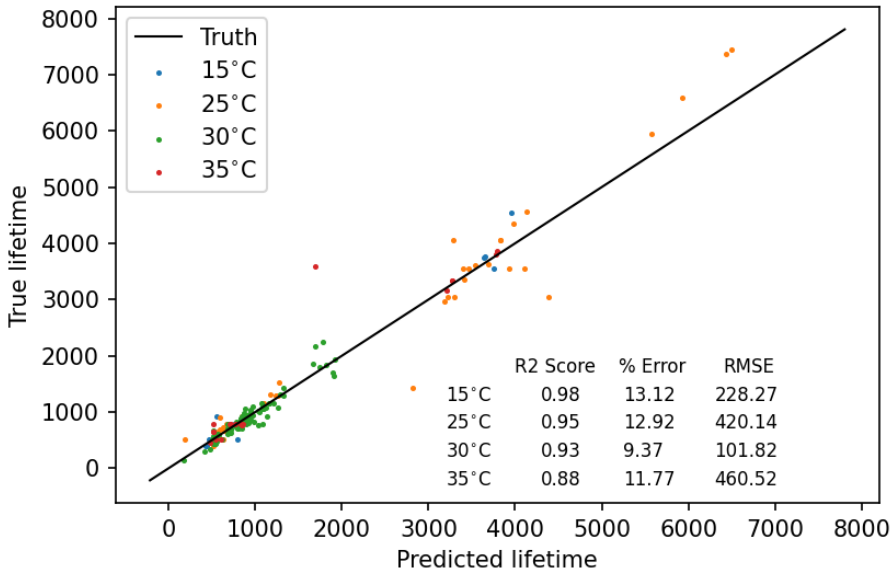

Figure 38. Performance metrics of the neural network with respect to different operating temperature.

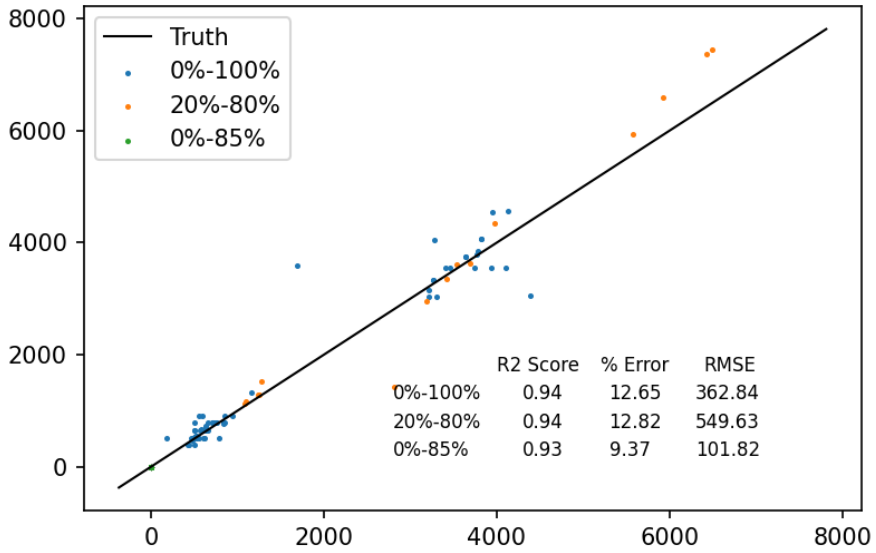

Figure 39. Performance metrics of the neural network with respect to different depths of discharge.

7.4.1. Model Features and Experimental Tests .

7.2.3.1. Regression Results

The regression algorithm is scored a variety of ways in the original work. Recall the regression algorithm aims to estimate the true cycle lifetime of the cell. The scores presented here represent the *percent error* defined by the equation:

$$Err = \frac{1}{n}\sum_{i=1}^{n}\frac{|y_i - \hat{y}_i|}{y^i}\cdot 100\%$$

where y is the true outcome variables and $\hat{y}_i$ is the predicted value.

The regression models for the full feature set significantly outperform the results from the previous cited work. The training and validation mean percent errors are <1% and 4.6%,

respectively, compared to the reported results of 5.6% and 14.1%. The test data exhibits 5.2% error (

Figure 27), compared to the 10.7% error in the paper. The discharge-only (Figure 28) and variance-only (Figure 29) feature set models compare favorably to the previously published results. Overall, the regression models from the prior research report have been successfully reproduced as shown below.

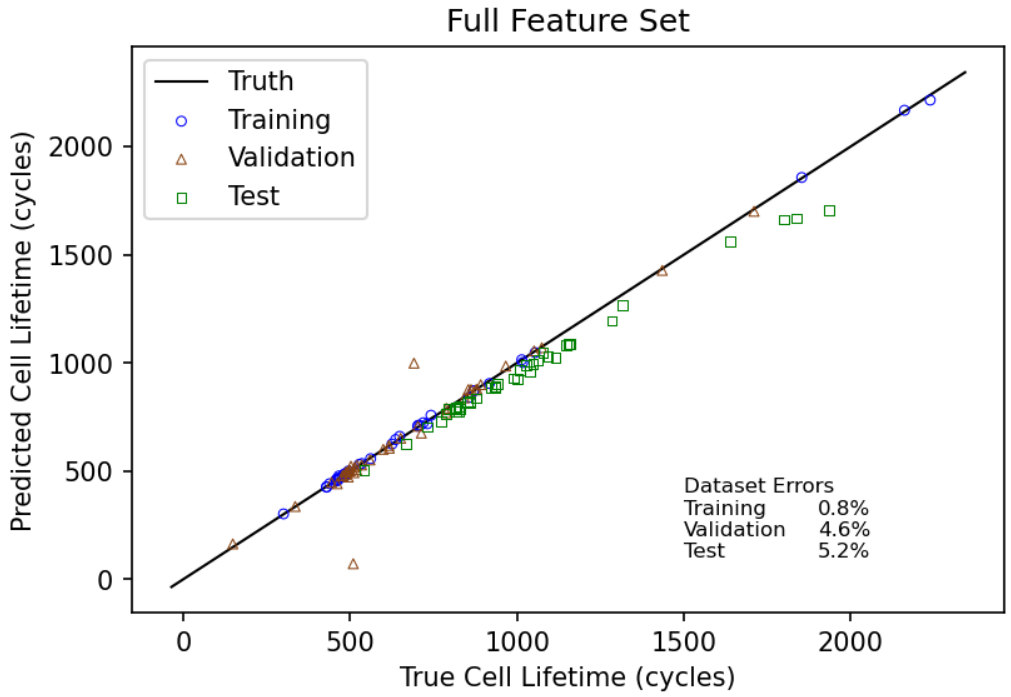

Figure 27. Observed and predicted lifetime for full model.

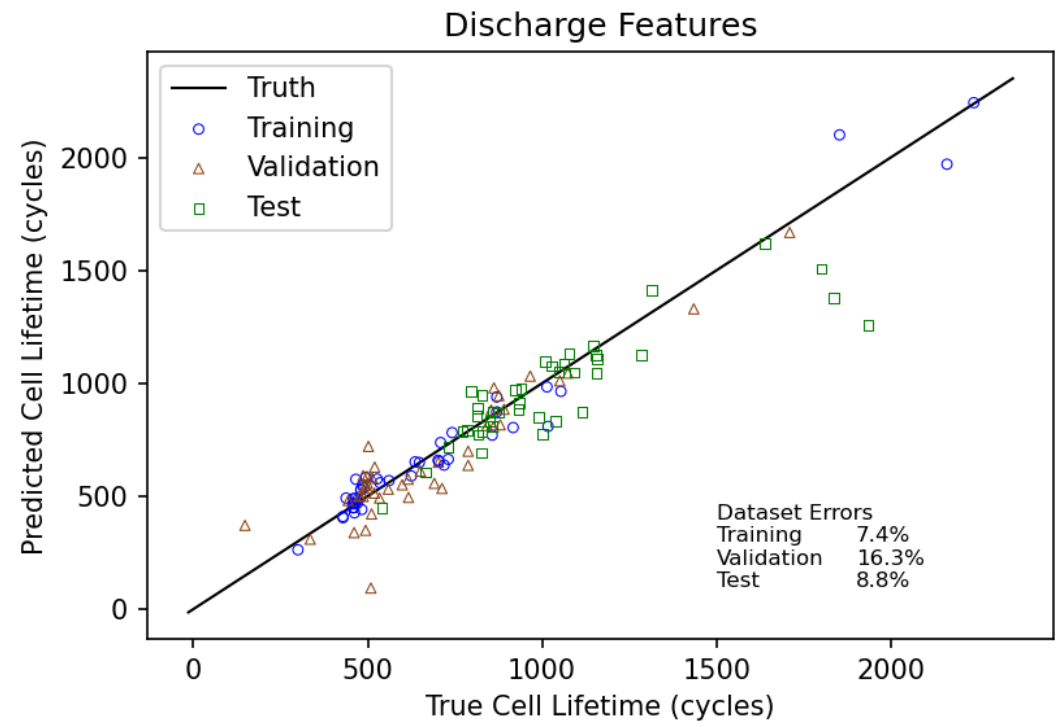

Figure 28. Observed and predicted lifetime for discharge model.

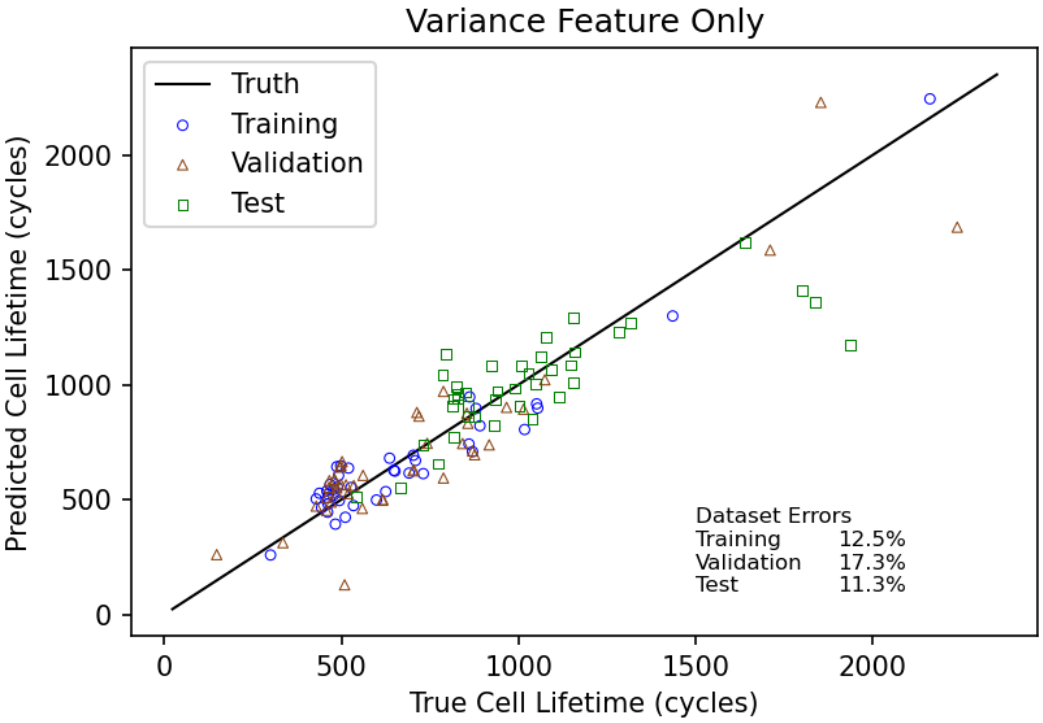

Figure 29. Observed and predicted lifetime for variance model.

7.2.3.2. Classification Results

The classification algorithm is scored based on its accuracy. Recall that the classification algorithm aims to categorize cells as cells that will last longer than 550 charge-discharge cycles and cells that will last less than 550 charge-discharge cycles using data from the first 5 charge-discharge cycles. An 'accurate' classification means that the algorithm places a sample into the correct category. Accuracy is defined as the simple ratio between correct and total samples.

The classification models are presented in the following figures. The model that uses only the variance feature achieves 76%, 83%, and 97% accuracy for the training, validation, and test data sets, respectively (Figure 30). The full-feature model has an accuracy of over 90% for all three datasets when classifying cells into bins of cells expected to last longer or shorter than 550 charge-discharge cycles (Figure 31). These results slightly differ from the original paper, but overall yield good results for a low-data situation.

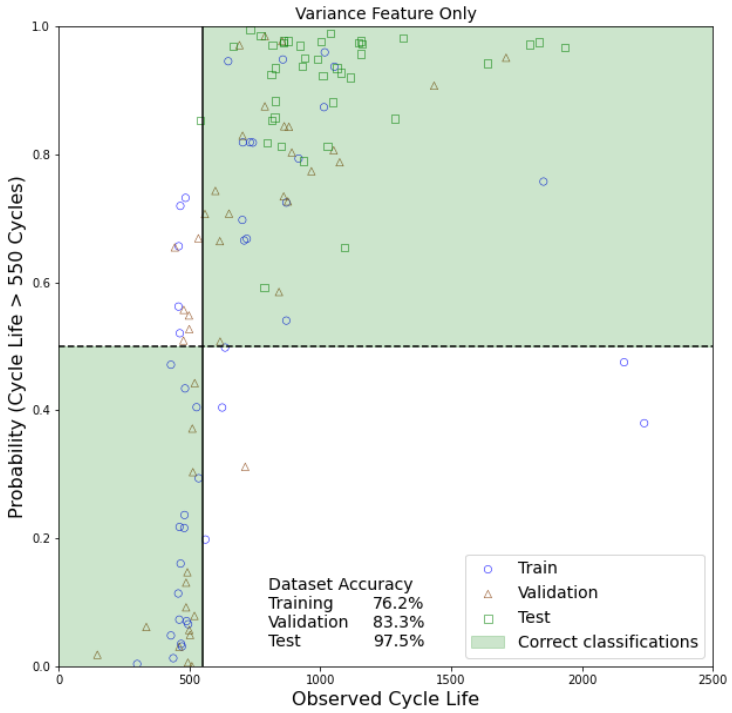

Figure 30. The probability of a battery's lifetime exceeding the lifetime threshold of 550 cycles vs observed cycle life using the "variance classifier". The decision boundary is 0.5.

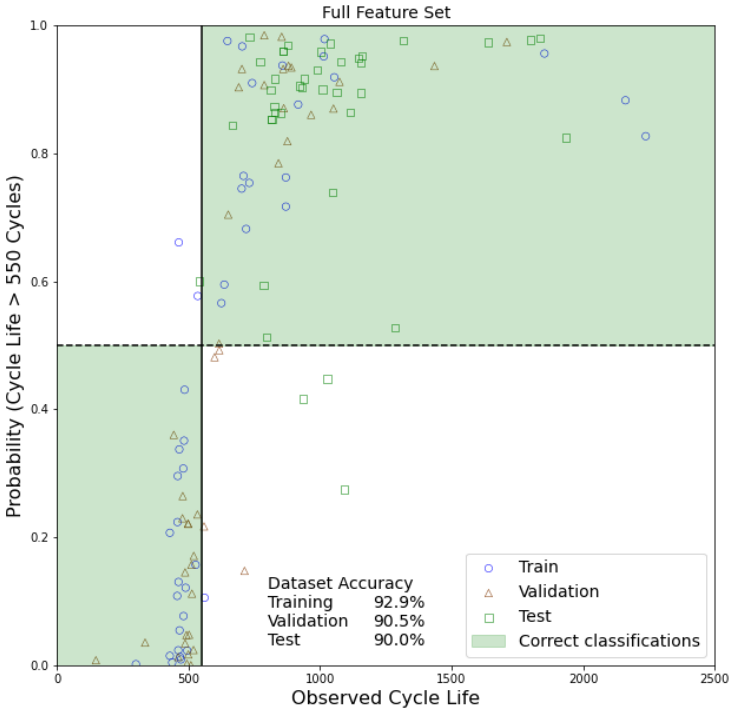

Figure 31. The probability of a battery's lifetime exceeding the lifetime threshold of 550 cycles vs observed cycle life using the "full classifier". The decision boundary is 0.5.

7.3. Expanding the Parameter Space

The second milestone of the effort focuses on developing a neural network which can accurately predict end-of-life of cells covering a wider parameter space than the original work. This is necessary as different types of lithium-ion batteries are used in varying operating conditions based on the application. Here we use a combination of dataset used for above to achieve proof-of-concept[201] and another dataset in which the cell cycling was performed with a larger variety of cell chemistries and test conditions.[210]

The dataset used to develop the regression models for in the previous section includes cycling data for lithium iron phosphate (LFP) cells with only one varying parameter i.e., charging policy. The second dataset includes cycling data for lithium iron phosphate (LFP), lithium nickel cobalt aluminum oxide (NCA), and lithium nickel manganese cobalt oxide (NMC)

cells obtained under varying cycling conditions as shown in Table 8. All the cells in this dataset were charged at the rate of 0.5C.

Table 8. Cycling conditions used to generate the dataset

	Cell Chemistry		
Cycling Parameter	LFP	NMC	NCA
Temperature	15°C, 25°C, 35°C	15°C, 25°C, 35°C	15°C, 25°C, 35°C
Depth of Discharge	0%-100%, 20%-80%	0%-100%, 20%-80%	0%-100%, 20%-80%
Discharge policy	0.5C, 1C, 2C, 3C	0.5C, 1C, 2C, 3C	0.5C, 1C, 2C

7.3.1. Feature Development

The features used to optimize the neural network were selected from the same features used to train the full model in section 7.2. The features selected can also be computed using the raw data available in the second dataset. Since the second dataset does not have internal resistance (IR) data, the features computed using IR data were omitted. The features used are mentioned in the features section.

The features computed from the combined dataset were split into training, validation and testing datasets and the neural network was optimized using the training and validation datasets. Testing data as mentioned previously is data that has never been used for training the neural network or tuning the hyperparameters and is used to test the performance of the model once it achieves desirable results with the training and validation data.

7.3.2. Model Training

Neural networks in general use learning algorithms to adjust their free parameters (i.e., the biases and weights) to attain the desired network output.[211,212] The algorithm used in this case is backpropagation. Backpropagation computes the gradient of an objective (also referred to as a cost/loss/performance) function to determine how to adjust a network's parameters in order to

minimize errors that affect performance.[213] Neural networks generate outputs only based on the correlation formed (i.e., the biases and weights calculated using the backpropagation algorithm) between the inputs and the outputs during the training. Hence, the training dataset must be vast and contain relevant features to obtain accurate results.

The network architecture and hyperparameters were optimized by manually tuning them such that the loss function of the network is minimized. The network architecture is shown in Figure 32 and the hyperparameters tuned are as follows:

1. **Number of hidden layers** between the input and output
2. **Activation functions** are used to introduce nonlinearity to models, which allows deep learning models to learn nonlinear prediction boundaries.
3. **Dropout** is regularization technique to avoid overfitting (increase the validation accuracy) thus increasing the generalizing power. The rate varies from 0 to 1, with 0 having the minimal effect.
4. **Optimizers** are used to solve optimization problems by minimizing the loss function.
5. **Number of epochs** is the number of times the whole training data is shown to the network while training.
6. **Batch size** is the number of sub samples given to the network after which parameter update happens.

The model is trained until the training and validation loss functions are minimized and does not decrease with the increase in number of epochs as shown in Figure 33. The weights calculated at the epoch with minimum validation loss are saved as model weights.

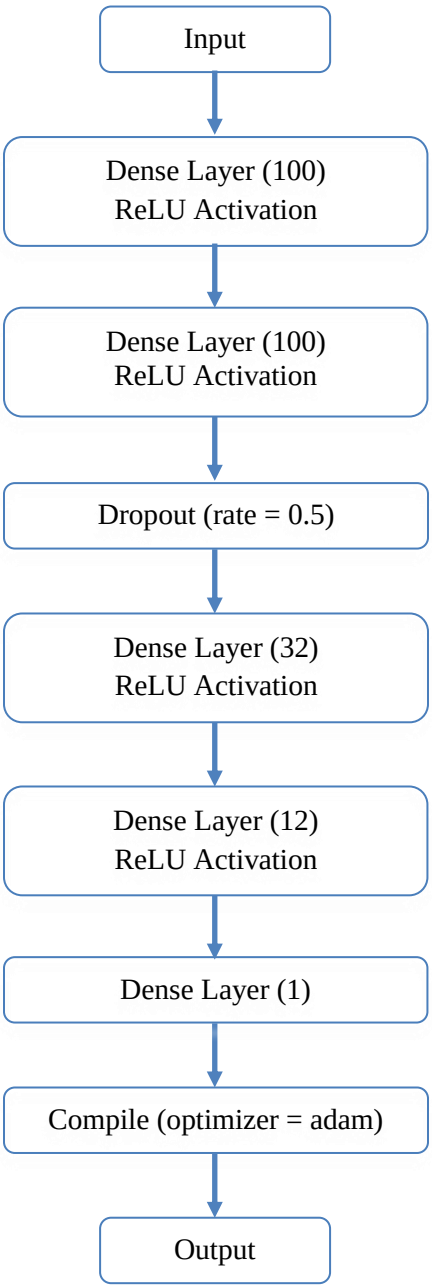

Figure 32. The architecture of the neural network developed.

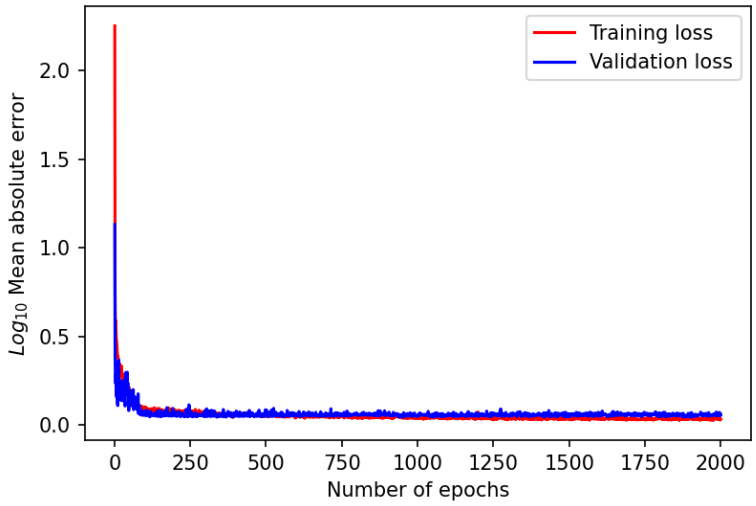

Figure 33. Training and validation loss observed with the increase in number of epochs.

7.4. Results and Discussion

The performance of the neural network is evaluated by using the following metrics:

R2 score (Coefficient of determination):

$$R^2\left(y, \hat{y}\right) = 1 - \frac{\sum_{i=1}^{n}\left(y_i - \hat{y}_i\right)^2}{\sum_{i=1}^{n}(y_i - \overline{y})^2}$$

$$\text{where } \overline{y} = \frac{1}{n}\sum_{i=1}^{n} y_i$$

Percentage error:

$$Err = \frac{1}{n}\sum_{i=1}^{n}\frac{|y_i - \hat{y}_i|}{y^i} \cdot 100\%$$

Root mean squared error:

$$RMSE = \sqrt{\frac{\sum_{i=1}^{n}\left(y_i - \hat{y}_i\right)^2}{n}}$$

where y_i is the true value and $\hat{y}_i$ is the predicted value.

Figure 34 below show the absolute error in the predicted lifetime of the cells and Figure 35 shows the performance metrics of the model on training, validation, and testing datasets.

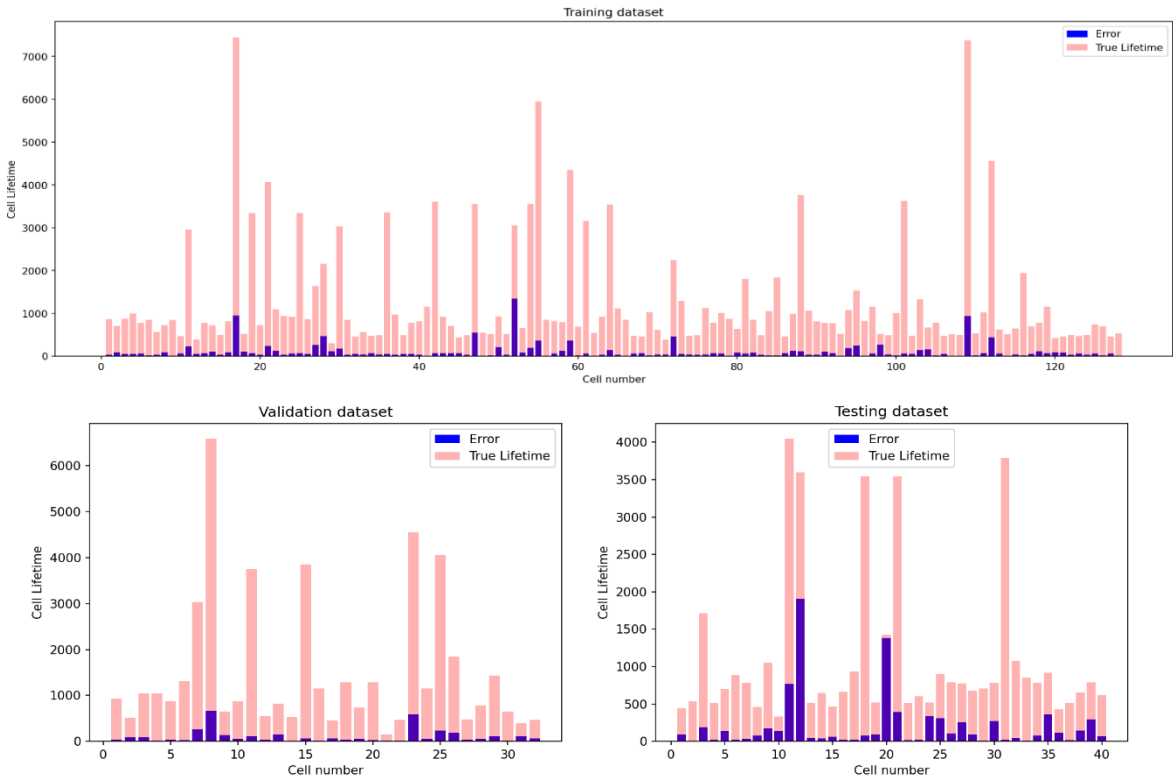

Figure 34: Absolute error observed in the lifetime prediction for cells in the training, validation, and testing dataset.

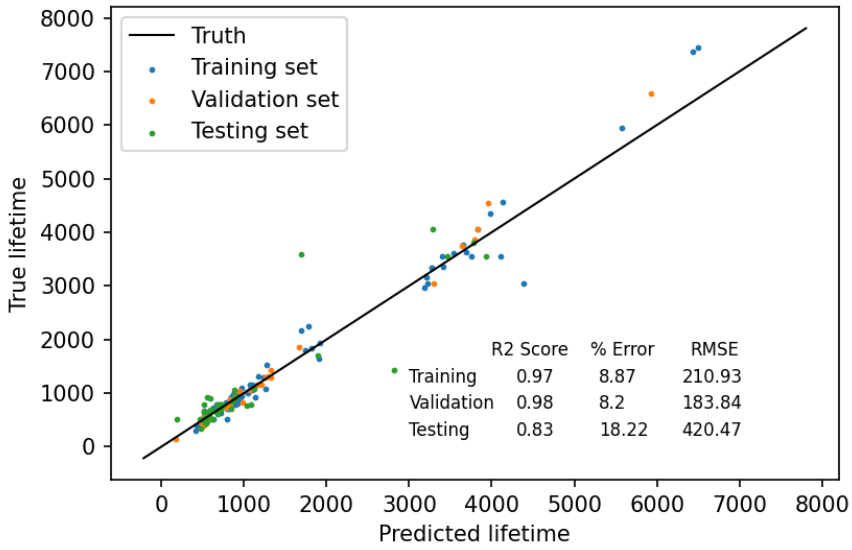

Figure 35. Observed and predicted lifetime for the neural network.

The following figures show the error in prediction with respect to subsets of datasets, namely cell chemistries (Figure 36), charging rate (Figure 37), cycling temperature (Figure 38), and depth of discharge (Figure 39). The model performs well on all the subsets with only a little variation in error.

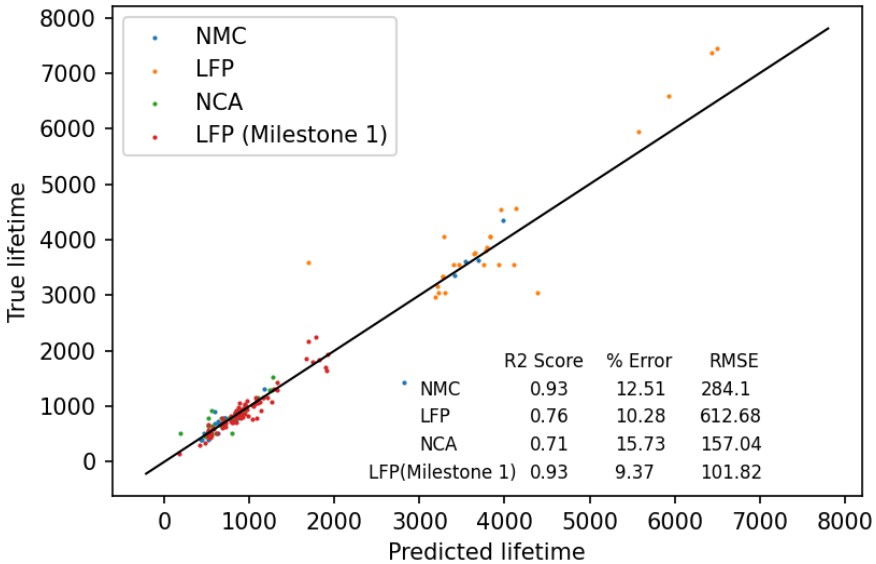

Figure 36. Performance metrics of the neural network with respect to different cell chemistries.

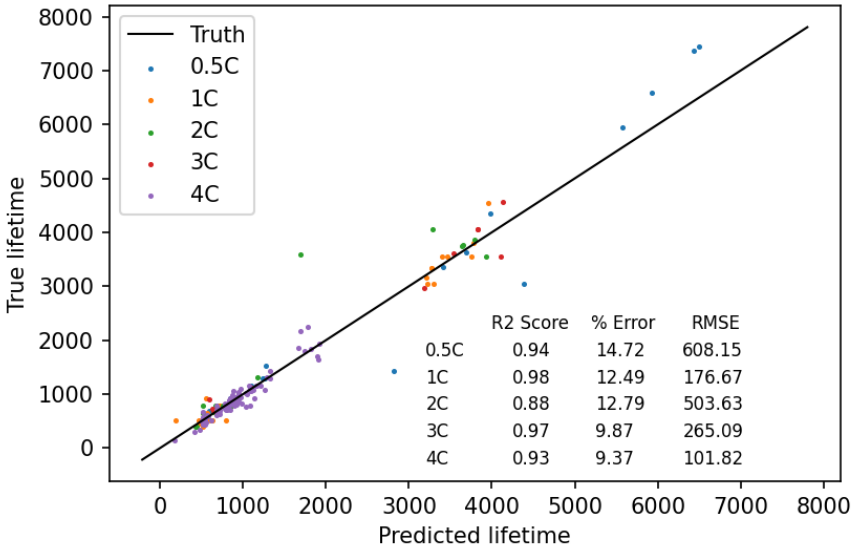

Figure 37. Performance metrics of the neural network with respect to different charging policies.

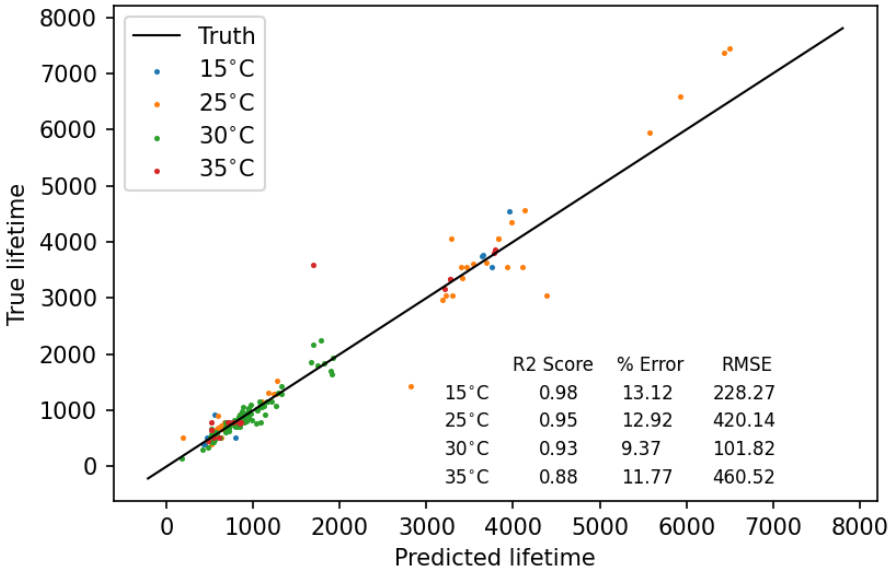

Figure 38. Performance metrics of the neural network with respect to different operating temperature.

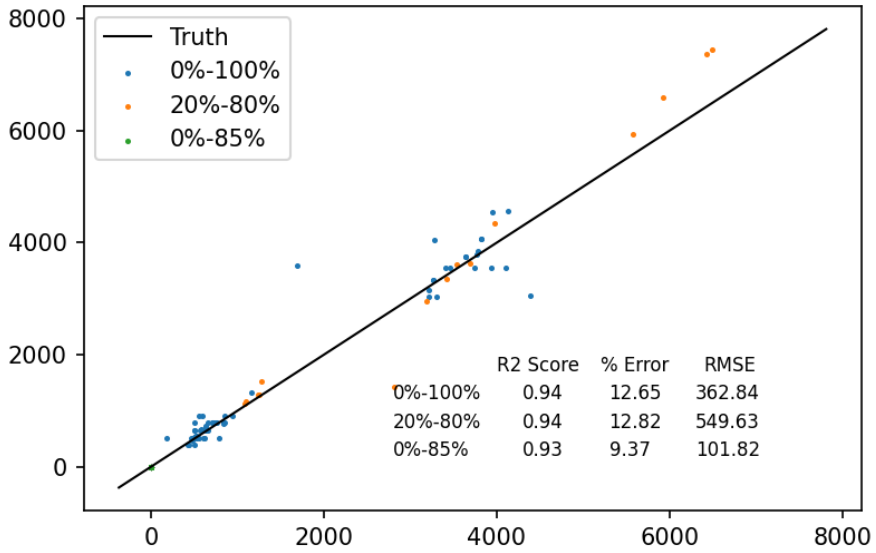

Figure 39. Performance metrics of the neural network with respect to different depths of discharge.

7.4.1. Model Features and Experimental Tests

7.4.1.1. Features and Feature Sets

The features used to develop each model are shown in Table 9. The three feature sets used in the previous work[201] are named *full*, *discharge*, *and variance*, and this work is named *Neural Net*.

Table 9. Features considered in different models.

Feature	Full	Discharge	Variance	Neural Net
$Q_{variance}^{100-10}$	✓	✓	✓	✓
$Q_{minimum}^{100-10}$	✓	✓		✓
$Q_{skewness}^{100-10}$	✓	✓		✓
$Q_{kurtosis}^{100-10}$	✓	✓		✓
Q^{2}	✓	✓		✓
$Q^{\{\max[2,100]-2\}}$	✓	✓		
$Q_{slope}^{\{2,100\}}$	✓			
$Q_{intercept}^{\{2,100\}}$	✓			✓
$IR_{minimum}^{\{2,100\}}$	✓			
IR^{100-10}	✓			
$\int_{2}^{100} T\ dt$	✓			✓
Average charge time, first 5 cycles	✓			✓

The first four features in the table use discharge capacity curves from the 10th and 100th cycle. The discharge capacity-voltage curves are fit to a spline, and then subtracted from each other. The subtracted curve is used to compute statistics (variance, minimum, skewness, and kurtosis) that are used as features. This gives an idea of how the capacity-voltage curves change between the 10th and 100th cycle. Similarly, the classification models use the same features but between the 4th and 5th cycle instead of the 10th and 100th. The feature Q^2 is simply the discharge capacity at cycle 2. The feature $Q^{\max[2,100]-2}$ is the discharge capacity at cycle 2 subtracted from the maximum discharge capacity between cycle 2 and cycle 100. The $Q^{\{2,100\}}$ slope and intercept features fit a linear line to the discharge capacity values between cycles 2 and 100, and report the slope and y-intercept of the linear line. The IR features select the minimum internal resistance (IR) between cycles 2 and 100, and the IR at cycle 10 subtracted from the IR at cycle 100.

Finally, the integral feature computes the integral of the measured temperature between cycles 2 and 100. Details for the computation can be found in the original work.[201]

The choice of using a neural network has advantages and disadvantages. As we have shown, these are powerful models that provide high accuracy. Neural nets are extremely flexible "low bias" models that generally perform well with ample data but poorly with limited data. In low-data settings, models with higher "bias" are preferred. Bias can be thought of as assumptions as to how the data is related to what you're trying to predict. For example, in linear regression models, there is a "high bias" that assumes that a linear combination of the features can be used to accurately make predictions. As such, by taking this approach means that we can improve performance as we add new datasets. Further, adding more data means that we can add more features to our model in a more robust way. Nevertheless, neural networks are usually used with surplus input features assuming the network will figure out the relationships by itself.

As neural networks are inherently uninterpretable models, it has the drawback that it will not readily lend itself to physical interpretation.[214] However, insofar as this model is designed to be employed in engineering rather than fundamental science applications, the emphasis is on getting to accurate predictions as fast as possible, and interpretability is not as much of a drawback.

7.4.1.2. Real World Tests

The most important developed features rely on discharge capacity-voltage curves for cycles 2, 3, 4, 5, 10, and 100. Measurements every 5-10 cycles may improve model performance, but the relationship between measurement frequency and model performance are not currently known. Future studies will focus on the relationship between minimizing measurement frequency and model performance. Other features use internal resistance and temperature measurements from the same cycles, so ideally the cycling data will include both measurements when available.

We speculate that the reason that the expanded model here appears to work across three separate cathode chemistries is because of the failure mode of these cells. Differential capacity analysis suggests that the major contributions to capacity fade are loss of lithium inventory and loss of active negative electrode material.[201] It is likely that solid-electrolyte interphase formation at the graphite anode is responsible for both of these degradation modes. As such, since graphite-based anodes are used regardless of the cathode chemistry, we expect that our model will be adaptable immediately to Li-ion systems where the cathode is not a major contributor to degradation. More work would be required to validate this hypothesis, but extending this insight at the basic chemistry level to inform the development of battery prognostics and diagnostics is likely to be fruitful.

7.5. Conclusion

Here we extended state-of-the-art battery cycle life prediction to include openly available data across a wider range of temperatures, charging protocols, and cell chemistries using a neural network. Using relatively sparse data, the neural network achieves percent error between 9 and 19% depending on the subset of conditions modeled in question. By design, the model will only improve as more data is made available and as new electrochemically significant features are discovered and integrated into the model. This model works not only with LFP cells as demonstrated in previous work, but also is applicable to NCA and NMC cell chemistries. We believe this is attributable to the fact that a common failure mechanism at the anode (SEI formation) dominates capacity fade, regardless of the cathode chemistry involved. This represents a step towards a standard operating procedure for rapid cell characterization in engineering environments where a wide range of practical conditions need to be studied, such as cell acceptance testing or cell validation.

7.6. Planned Future Development

7.6.1. Feature Development

We will continue to develop features that show high correlation to the cell cycle lifetime. This is an ongoing effort, and highly correlated features may significantly improve model performance. The features will be developed based on physics-inspired concepts. Further, we will utilize concepts from dynamical time series data including approaches seen in nonlinear dynamical systems approximations.

7.6.2. Neural Networks

Neural networks generate outputs only based on the correlation formed (i.e., the biases and weights calculated using the backpropagation algorithm) between the inputs and the outputs during the training. Hence, they need to be trained with vast amounts of data containing relevant features. The accuracy of the neural network developed here is similar to that of the state-of-the-art discharge model reproduced earlier and can be increased by training the network with more cycling data. Cycling data obtained under different conditions than the ones used now can also be added to the training data to generalize the model more so that it can be used in a wide range of applications. Significant increase in the accuracy of the model is thus contingent to availability of adequate training data. There are several other openly available datasets that we intend to integrate into our current model.[215]

7.6.3. Uncertainty quantification

The subject of uncertainty quantification has been understudied.[216] In a faced-paced engineering environment, teams are always optimizing between speed to decision and accuracy of decision-making. For example, it may or may not "satisfice" to obtain results with 80% confidence after 1 week of testing rather than 95% confidence after 1 month of testing, and there are rapidly diminishing returns for the time taken to achieve greater than 95% accuracy. Efforts are underway to develop a data pipeline for automating a method for uncertainty quantification

to not only provide an estimate for battery cycle life, but also provide a measure of statistical confidence in that estimate. This allows for rational decision making that optimizes between accuracy of a given test result and the time taken to reach it.

Chapter 8. Identification of Weak Cell Blocks in Electric Aircraft Battery Packs

8.1. Introduction

The emerging electric aviation industry is poised to revolutionize transportation for a wide array of purposes, from last-mile fulfillment to urban air mobility and short-haul regional flights. The main benefits of electric aviation include lower operation and maintenance costs, lower environmental impact, and freedom to operate without runaways when vertical take-off and landing capability is employed.

The development and assessment of energy storage systems is critical for this new environment. In contrast with automotive electrification, the aerospace and aviation markets demand higher performance and more stringent safety requirements. The standard operating procedures for battery-powered electric aviation have not yet been defined, and there are gaps in understanding battery safety and reliability as these systems age. This poses major challenges for both the certification agencies who must define these new safety standards or procedures, and the manufacturers who must implement these new processes.

One such challenge is the determination of remaining useful energy (RUE). This is a complicated problem that depends on the mission profile, state of health, state of charge, and cell-to-cell variation, among other factors. Batteries are complicated electrochemical systems that show nonlinear aging and performance from one cell or one lot of cells to another. As a consequence of this intrinsic heterogeneity, cells connected in series will be loaded with the same current but reach a cutoff voltage at different times depending on their individual internal resistances. Therefore, the overall battery pack performance is governed by the performance of the weakest cells in the pack. In this work we specifically focus on the rapid identification of the weakest cell blocks in a battery pack as a preliminary step towards the development of more robust RUE algorithms for electric aviation.

8.2. Methods

In this work, data was collected from battery packs assembled by Beta Technologies, Inc. and composed of 21700 lithium-ion cells. Each pack was assembled from 14 modules, and each module consisted of 14 cell blocks, thus each pack had 196 cell blocks connected in series. The dataset consisted of 53 hour-long flight tests of these packs, where the load profile of all cell blocks is shown in Figure S1a, and the voltage profile of each of the 196 cell blocks subjected to this load is shown in Figure S1b.

Here the weakest cell blocks were defined to be those cell blocks with the lowest open circuit voltage at the end of the flight test (Figure S2). The input data was the first five minutes of time series data at the start of the flight test (example shown in Figure S3**Error! Reference source not found.**).

The open circuit voltage for weak cell blocks tends to be noticeably lower than the median value (Figure S4), and as such an outlier detection algorithm was developed for this purpose.

Local Outlier Factor (LOF) is a density-based outlier detection algorithm that was employed here.[217] The LOF algorithm is an unsupervised anomaly detection method which computes the local density deviation of a given data point with respect to its neighbors. It considers as outliers the samples that have a substantially lower density than their neighbors. The parameters in Table 100 were used to detect the weak cells using the LOF algorithm from Scikit-learn.[218]

Table 10. Input parameters for the LOF algorithm.

Parameter	Value
Nearest neighbors, *n_neighbors*	35
Contamination	0.1
Distance, *p*	1
Algorithm	‘brute’

The first parameter finds the *n* nearest neighbors of a point and returns the distance to each point (known as nearest neighbor search). The amount of contamination of the data set, i.e., the

proportion of outliers in the data set. When fitting this is used to define the threshold on the scores of the samples. The third parameter is the metric used to calculate distance. Here $p = 1$ is equivalent to using the Manhattan distance, the distance between two points measured along axes at right angles. In a plane with point p_1 at (x_1, y_1) and point p_2 at (x_2, y_2), it is defined as $|x_1 - x_2| + |y_1 - y_2|$. Lastly, the brute-force search algorithm is usually used for low-dimensional data.

The main features of significance that were found to have predictive power were the minimum voltage and voltage integral (Figure 40). Voltage integral is a simple numerical integration of the voltage over the 5-minute time frame considered. The implementation from Scipy[219] uses the composite trapezoidal rule to calculate the integral and assumes sample points are evenly spaced apart.[220]

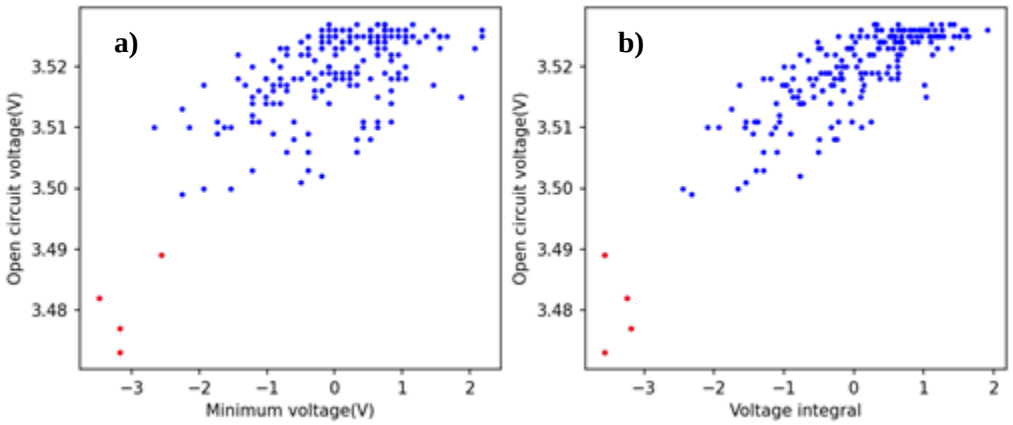

Figure 40. a) The minimum voltage and b) voltage integral where the two features found to have the best predictive power for this algorithm.

A schematic diagram of the overall algorithm development and execution process is shown in Figure 41. Clockwise from the upper left, input data from flight tests is analyzed and features such as voltage integral and minimum voltage are developed. The outlier detection algorithm is applied, and from the set of outliers identified, the two weakest cell blocks are filtered out.

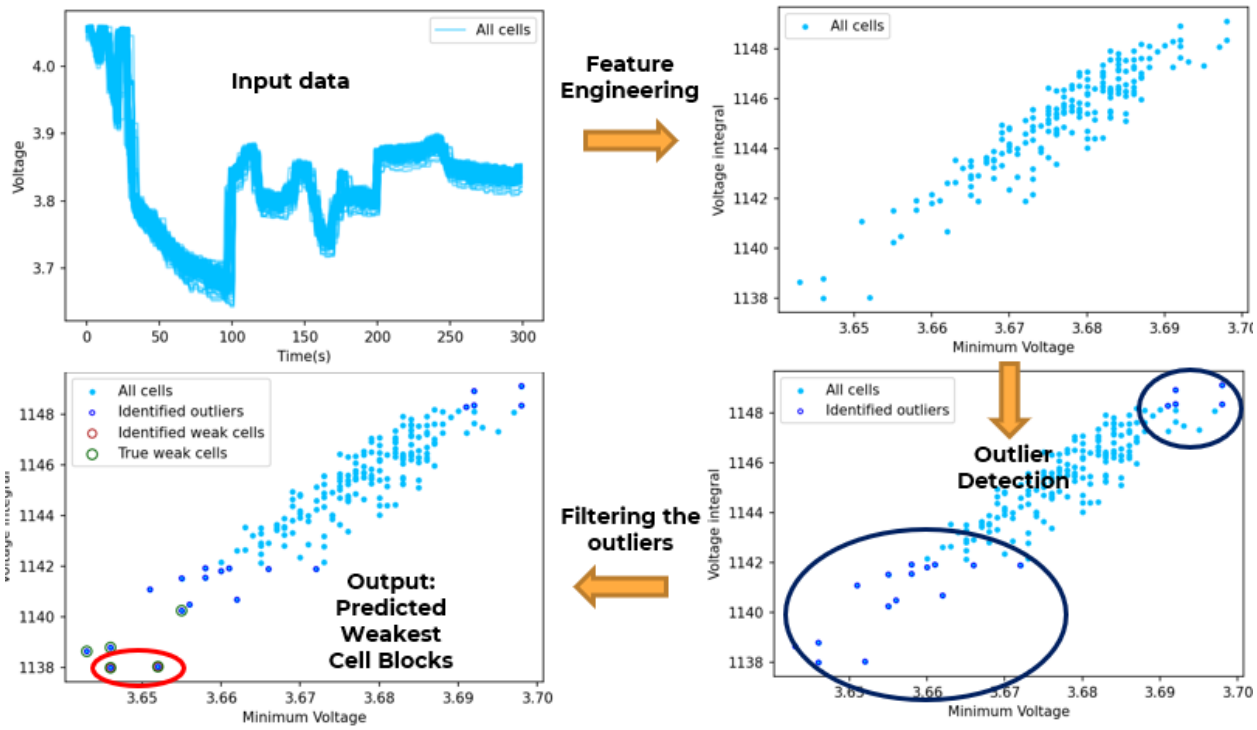

Figure 41. Schematic diagram of the overall algorithm.

8.3. Results

The algorithm developed correctly identified the weakest cell blocks in the pack 88.6% of the time (i.e. in 47 out of the 53 flight tests considered, Table 11). Two cell variants were used from the same manufacturer, where cell variant 2 is distinguishable in that it has a lower internal resistance. Most packs were composed of entirely one variant or the other, although four packs tested used a combination of the two.

Table 11. Algorithm prediction results.

Pack type	Number of battery packs	Correct results	Incorrect results
Cell Variant 1	33	29	4
Cell Variant 2	16	14	2
Mixed	4	4	0

The six flight tests where the incorrect cell blocks were flagged can be grouped into three categories. The first is attributed to time lags in data logging (Figure S5a). Discrepancies in data acquisition for this test lead to an offset in the voltage response for several cell blocks. In turn, this affected the calculation of the voltage integral and misidentified the weak cell blocks in this flight test (Figure S5**Error! Reference source not found.**b).

Another category of errors emerged when there were no apparent weak cell blocks (Figure S6). In the example shown below, the range between the highest and lowest voltage cell blocks was only 12 mV. A third category of errors can be attributed to empirical errors in filtering based on the engineered features.

8.4. Conclusion

An algorithm for identifying weak cell blocks in electric aircraft battery packs was developed using an outlier detection algorithm. The minimum voltage during the first five minutes and the voltage integral were empirically determined to be the two most important features for making this determination. The algorithm correctly identified the weakest cell blocks in 47 out of 53 cases using the first five minutes of flight test data as the input to the algorithm.

The accuracy of the algorithm can be improved by correcting the time lag in the data logging and developing features that can capture more failure modes. The development of this algorithm is a preliminary step along the way to developing more robust online fuel gauging algorithms for electric planes.

Chapter 9. Future Work for Battery Analytics in Electric Aviation

9.1. Introduction

The overarching goal of this project is to reduce risk around the development and operations of battery propulsion systems for electric aviation. The technical goals listed below focus on building new methods and algorithms for capturing battery health and performance. From a programmatic perspective, the goal is to use the technical results obtained to inform both defense and FAA standards for battery safety and certification. The results from this phase will be used to establish services and prototype products that can be scaled to support the growing electric aviation ecosystem.

During this program, we are working with Beta Technologies to develop shared infrastructure for battery data. With this foundation and our understanding of battery cell aging, we will provide cell-level diagnostics around battery life. A significant portion of this R&D program will revolve around studying how insights from the cell level propagate to performance and safety of a full battery system. The overarching goals of this effort is risk reduction around battery system operations and the establishment of appropriate safety standards for this environment. Our main objectives and key results include:

O1 – Develop recommended standards for end-of-life determination

KR1: Develop conservative end-of-life estimator using a fixed range rating.

KR2: Develop more aggressive end-of-life estimator using shrinking fuel tank rating.

KR3: Characterize other pack-level failure modes around degrading heat rejection or mechanical failure

O2 – Develop off-line testing methods of battery systems

KR1: Develop impedance-based test protocol to characterize battery packs for aviation during offline maintenance

KR2: Build algorithm that takes historical performance data and the results of the test developed in KR1 to project battery system range

O3 – Develop algorithms for online monitoring and prediction of battery health and performance

KR1: Improve accuracy of estimated hover time

KR2: Improve accuracy of estimated cruise time

9.2. Improved Acceptance Testing for Incoming Vendor Cells

The next task for full life cycle traceability (currently underway) will revolve around improving acceptance testing for incoming cells. As described in chapter 7, we have developed preliminary machine learning algorithms that can be deployed to identify "bad" cells that could negatively impact battery pack performance, thus reducing the risk of the system being unable to fulfill its mission.

Extended traceability of cells will allow for a systematic study of cell failure modes, either under induced catastrophic failure (e.g. nail penetration testing), or by more benign calendar- or cycle-based aging under conditions relevant to electric aviation applications. This information will be fed back into machine learning algorithms to continue to expand the parameter space where predictions can be made with confidence – namely over wider ranges of temperatures, duty cycles, and chemistries.

Here the key deliverable will be an algorithm that can process preliminary test data from vendors or acceptance tests to reduce cell-to-cell variation in capacity, voltage, and longevity. Adding uncertainty quantification will also be a component of this solution, in order to provide greater statistical confidence to engineering decision makers relying on these algorithms.

9.3. Offline Ground Maintenance

Building on the improved learning from cell-level data, pack- and module-level understanding will likewise improve. Our goal in this phase will be to develop standard operating procedures for assessing the health of battery packs during routine maintenance. Since this is an open area of active research for electric aviation, the outcome of this effort can be used to inform battery maintenance standards for Li-ion and novel battery chemistries, both for defense applications as well as the FAA.

Beta already has telemetry and infrastructure in place to detect cell failures from thermal runaway and subsequent lost capacity for a given 196-cell group. Leveraging the learning and results from improved acceptance testing, we will incorporate cell aging mechanisms into the understanding of how a battery pack or module ages under nominal operating conditions.

Electric aviation represents one of the most demanding applications for battery technology (Figure 42). The battery system must meet even more stringent safety requirements compared to standards in the automotive industry. Therefore, it will be feasible (if not, in fact, ideal) for us to initially perform teardowns of the pack and re-test individual cells in order to ascertain how our understanding of cell-level aging translates to pack-level performance. Comparing the lifetime aging trajectory of cells used to power flights against cell-level results from laboratory abuse testing will allow us to identify any gaps in our models and prescribe additional tests or data required to iteratively improve our predictions. We envision that the results that come from these tests will have implications across the development cycle of the battery system from design (e.g. heat rejection requirements or improvements), operations (e.g. standard operating procedures for charging), and most importantly for our purposes here, maintenance (e.g. prescriptions for tests that will steadily draw stronger conclusions around future battery performance).

Key deliverables will include a machine learning algorithm that takes known cell level data and predictions from the quality control process as well as historical pack-level data and performance to predict the range of the system bounded within confidence intervals mandated by aviation standards.

Another deliverable will be a DCIR performance test analogous to those employed in the automotive industry (such as the USABC Electric Vehicle Battery Test Procedures Manual[221]) will be developed that captures the degradation behavior of battery packs across its natural life cycle

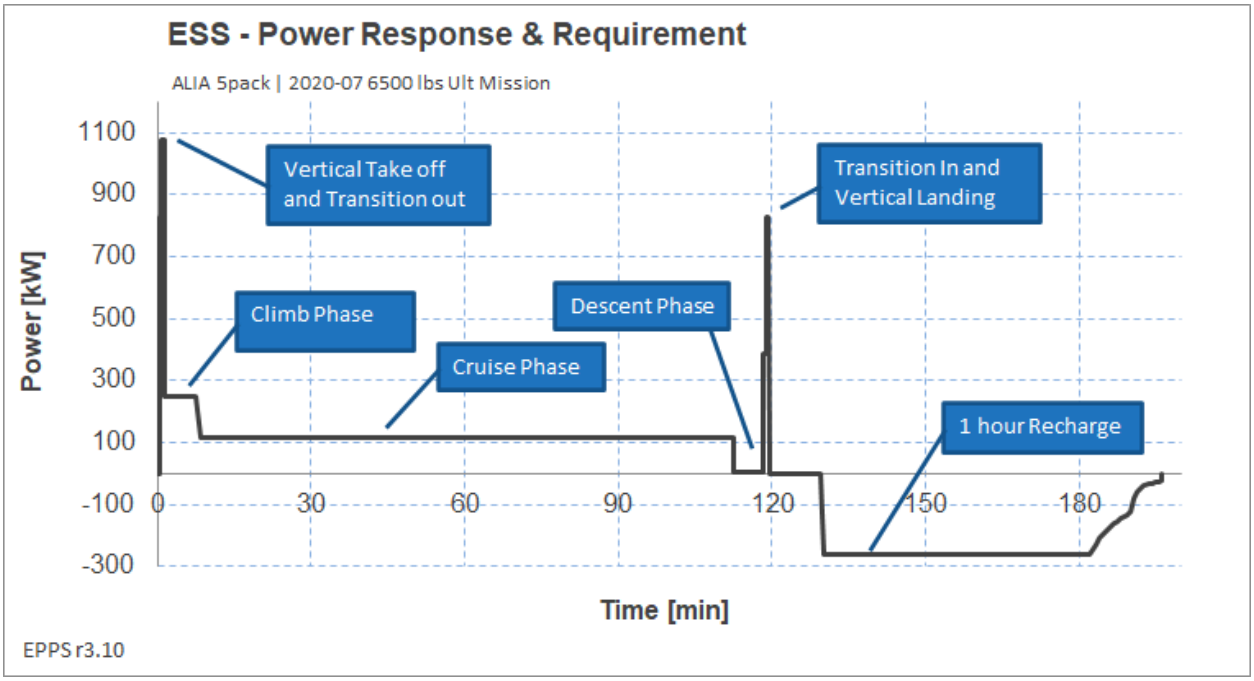

Figure 42. Example duty cycle for VTOL flight for Beta Technologies ALIA aircraft. Brief but massive power spikes at each takeoff and landing will dominate battery degradation characteristics under nominal operations conditions.

9.4. Online Fuel Gauging

As with offline maintenance, improvements made across cell life cycle testing can likewise be fed back to better predict online remaining usable power. The two primary metrics of consideration here are the estimated cruise time and the estimated hover time remaining. The cruise time is based on the differential change in voltage as a function of capacity (-dV/dQ) and a lower voltage

threshold, whereas the estimated hover time also includes the current open circuit voltage and estimates for internal resistance as inputs.

Using telemetry systems already under development by Beta, we will use live flight data to inform an algorithm that provides real-time estimates for both key flight metrics and report these values to the various relevant stakeholders, including the battery cell manufacturer, analytics team, and operator. Because of requirements around certification, the algorithm developed will not have to provide feedback directly to the BMS. Any updates to the code and parameters will go through a specific review to apply an update. This will effectively decouple algorithm development (by our team) from implementation with Beta and relaxes constraints that would otherwise require embedded systems engineering experience.

9.5. End-of-Life Determination

The most critical milestone will be around determining end-of-life and retiring battery packs from service. This is a crucial milestone not only for Beta, but also for the growing electric aviation industry, as power plants that previously burned fossil fuels are replaced with hybrid or fully electric propulsion systems. Unlike the more familiar case of electrification in the automotive industry, battery expertise is not as well distributed or established in aerospace, despite the more demanding safety and operations requirements.

To satisfy certification agencies like the FAA, new standards and criteria will need to be developed that are able to balance the aviation industry's requirements for extremely high safety and reliability against the economic reality of maximizing the number of missions a battery system will be able to complete.

We anticipate two tracks for developing EOL determination under nominal life cycle aging conditions. During the initial development of these standards, we will pursue a conservative range guarantee using a fixed range rating. That is, the battery system would start life with actual

performance that is much greater than the rated range (for example, the true range may be 250 miles while the rated range may only be 200 miles). Then the end of life would be defined as the point where it is no longer capable of delivering the requisite power and energy for a 200-mile mission.

As we learn and gain more confidence with predicting battery pack performance, we anticipate switching to a more accurate EOL determination that incorporates gradually decreasing battery pack performance (a.k.a. the shrinking fuel tank). In this instance, the battery system would start life at its rated range of 250 miles. As the battery system ages, the BMS would report a reduced range where system is safe to operate. As the accuracy and confidence of the EOL determination increases, aged packs could still be used to service short flights if they fall within the estimated range of safe operation.

It will also be important to track other challenges involved in EOL determination via other failure modes at the battery pack level. Such failure modes include: mechanical damage to the battery pack, BMS failure, or degradation of pack-level thermal cooling capabilities.

Chapter 10. Conclusions

This thesis represents a bimodal effort in both experimental and data-driven battery science. In the first half, we cover the challenges associated with the development of magnesium batteries as an alternative to Li-ion batteries. The other half of this work developed software and algorithms in support of battery data analytics and forecasting.

On the anode side, we successfully developed what was at the time one of the first known magnesium-conducting SEI layers. The MgF_2 coating produced surprisingly good performance compared to control tests with the natively forming SEI layer produced on magnesium metal in the APC electrolyte. Tailoring the SEI layer on magnesium metal is one of the most promising methods for enabling longer life for magnesium metal anodes.

On the positive side of the cell, we identified common pitfalls associated with studying cathode materials for magnesium batteries. We advocate for 3-electrode cells instead of 2-electrode coin cell testing for fundamental characterization to avoid confounding effects from the many failure modes of magnesium electrochemistry. Carbon felt is also more suitable both as a pseudo-reference electrode and counter electrode, compared to (uncoated) magnesium metal. FTO glass was shown to have higher voltage stability than even platinum and makes for a good substrate for 3-electrode testing. We also showed that the cathode-electrolyte interface is (by definition) critical for magnesium cathode electrochemistry, but underappreciated and may lead to misinterpretation for the source of what limits cathode performance.

These results demonstrate the importance of systems-level thinking to how magnesium electrodes interface with the electrolyte, rather than as three separate components (cathode, anode, electrolyte) than can be optimized independently of each other.

For the data science aspect of this work, we first presented a software solution suitable for ingesting battery test data from disparate sources. By aggregating data in an intelligent way,

users can streamline routine data analysis tasks and leverage Jupyter Notebook functionality to build advanced scripts and analytics, thereby making battery engineering teams more productive.

We also extended state-of-the-art battery cycle life prediction algorithms to a wider range of chemistries, temperatures, and charging protocols than previously reported. The neural network machine learning model achieved good accuracy with a modest amount of data and will improve as more datasets are used to train it. This algorithm is designed to be applied to real battery engineering environments for qualifying cells from suppliers and providing better quality assurance as cells are assembled into packs and modules.

Lastly, we reported an algorithm for identifying weak cell blocks in a electric aircraft battery pack. This algorithm uses the first five minutes of flight test data to extract features based on the individual cell block voltages that are predictive of low OCV. This represents a first step toward building out more sophisticated algorithms for fuel gauging for electric aircraft, an environment where the standards for electrification have not yet been written.

These three pieces constitute the starting point from which a full end-to-end solution for forecasting battery health, safety and performance will be developed. Ongoing efforts will continue to connect fundamental electrochemical degradation modes at the materials and cell level (e.g. those revealed with differential capacity analysis) to systems-level performance of entire battery systems, and guide the development of electric aircraft.

References

1. Bock, D. C., Marschilok, A. C., Takeuchi, K. J. & Takeuchi, E. S. Batteries used to power implantable biomedical devices. *Electrochimica Acta* **84**, 155–164 (2012).

2. Scrosati, B. Power sources for portable electronics and hybrid cars: Lithium batteries and fuel cells. *Chemical Record* **5**, 286–297 (2005).

3. Tran, M., Banister, D., Bishop, J. D. K. & McCulloch, M. D. Realizing the electric-vehicle revolution. *Nature Climate Change* **2**, 328–333 (2012).

4. Park, O. K. *et al.* Who will drive electric vehicles, olivine or spinel? *Energy & Environmental Science* **4**, 1621 (2011).

5. Pollet, B. G., Staffell, I. & Shang, J. L. Current status of hybrid, battery and fuel cell electric vehicles: From electrochemistry to market prospects. *Electrochimica Acta* **84**, 235–249 (2012).

6. Dunn, B., Kamath, H. & Tarascon, J.-M. Electrical Energy Storage for the Grid: A Battery of Choices. *Science* **334**, 928–935 (2011).

7. Yang, Z. *et al.* Electrochemical energy storage for green grid. *Chemical Reviews* **111**, 3577–3613 (2011).

8. Liu, J. *et al.* Materials Science and Materials Chemistry for Large Scale Electrochemical Energy Storage: From Transportation to Electrical Grid. *Advanced Functional Materials* **23**, 929–946 (2013).

9. U.S. Energy Information Administration. June 2016 Monthly Energy Review. 173–185 (2016).

10. Sandy Thomas, C. E. How green are electric vehicles? *International Journal of Hydrogen Energy* **37**, 6053–6062 (2012).

11. Tessum, C. W., Hill, J. D. & Marshall, J. D. Life cycle air quality impacts of conventional and alternative light-duty transportation in the United States. *Proceedings of the National Academy of Sciences* **111**, 18490–18495 (2014).

12. Oron, A. P. Electric vehicle footprint analysis is misleading. *Proceedings of the National Academy of Sciences* **112**, E3973–E3973 (2015).

13. Larcher, D. & Tarascon, J.-M. Towards greener and more sustainable batteries for electrical energy storage. *Nature Chemistry* **7**, 19–29 (2014).

14. Eyer, J. & Corey, G. Energy Storage for the Electricity Grid : Benefits and Market Potential Assessment Guide. *Contract* **321**, 232 (2010).

15. Koohi-Kamali, S., Tyagi, V. V., Rahim, N. A., Panwar, N. L. & Mokhlis, H. Emergence of energy storage technologies as the solution for reliable operation of smart power systems: A review. *Renewable and Sustainable Energy Reviews* **25**, 135–165 (2013).

16. Luo, X., Wang, J., Dooner, M. & Clarke, J. Overview of current development in electrical energy storage technologies and the application potential in power system operation. *Applied Energy* **137**, 511–536 (2015).

17. Kirby, B. J. Frequency Regulation Basics and Trends. (2004).

18. EPRI-DOE Handbook of Energy Storage for Transmission & Distribution Applications. (2003).

19. He, X., Delarue, E., D'haeseleer, W. & Glachant, J. M. A novel business model for aggregating the values of electricity storage. *Energy Policy* **39**, 1575–1585 (2011).

20. Balducci, P., Jin, C., Wu, D. & Kintner-Meyer, M. Assessment of Energy Storage Alternatives in the Puget Sound Energy System. (2013).

21. Walawalkar, R., Apt, J. & Mancini, R. Economics of electric energy storage for energy arbitrage and regulation in New York. *Energy Policy* **35**, 2558–2568 (2007).

22. Diorio, N., Dobos, A., Diorio, N. & Dobos, A. Economic Analysis Case Studies of Battery Energy Storage with SAM Economic Analysis Case Studies of Battery Energy Storage with SAM. (2015).

23. Kousksou, T., Bruel, P., Jamil, A., El Rhafiki, T. & Zeraouli, Y. Energy storage: Applications and challenges. *Solar Energy Materials and Solar Cells* **120**, 59–80 (2014).

24. Pawel, I. The cost of storage - How to calculate the levelized cost of stored energy (LCOE) and applications to renewable energy generation. *Energy Procedia* **46**, 68–77 (2014).

25. Battke, B., Schmidt, T. S., Grosspietsch, D. & Hoffmann, V. H. A review and probabilistic model of lifecycle costs of stationary batteries in multiple applications. *Renewable and Sustainable Energy Reviews* **25**, 240–250 (2013).

26. Poonpun, P. & Jewell, W. T. Analysis of the Cost per Kilowatt Hour to Store Electricity. *IEEE Transactions on Energy Conversion* **23**, 529–534 (2008).

27. Zakeri, B. & Syri, S. Electrical energy storage systems: A comparative life cycle cost analysis. *Renewable and Sustainable Energy Reviews* **42**, 569–596 (2015).

28. Ibrahim, H., Ilinca, A. & Perron, J. Energy storage systems-Characteristics and comparisons. *Renewable and Sustainable Energy Reviews* **12**, 1221–1250 (2008).

29. Srinivasan, V. The Three Laws of Batteries (and a Bonus Zeroth Law). *Gigaom* https://gigaom.com/2011/03/18/the-three-laws-of-batteries-and-a-bonus-zeroth-law/ (2011).

30. Liu, C., Neale, Z. G. & Cao, G. Understanding electrochemical potentials of cathode materials in rechargeable batteries. *Materials Today* **19**, 109–123 (2015).

31. Xu, K. Nonaqueous liquid electrolytes for lithium-based rechargeable batteries. *Chemical Reviews* **104**, 4303–4417 (2004).

32. Xu, K. Electrolytes and interphases in Li-ion batteries and beyond. *Chemical Reviews* **114**, 11503–11618 (2014).

33. Arora, P. & Zhang, Z. (John). Battery Separators. *Chemical Reviews* **104**, 4419–4462 (2004).

34. Crabtree, G. The Joint Center for Energy Storage Research: A New Paradigm for Battery Research and Development. *AIP Conference Proceedings* **1652**, 112–128 (2014).

35. Kam, K. C. & Doeff, M. M. Electrode Materials for Lithium Ion Batteries. *Material Matters* vol. 7 56–60 (2012).

36. Julien, C. M., Mauger, A., Zaghib, K. & Groult, H. Comparative Issues of Cathode Materials for Li-Ion Batteries. *Inorganics* **2**, 132–154 (2014).

37. Nitta, N., Wu, F., Lee, J. T. & Yushin, G. Li-ion battery materials: Present and future. *Materials Today* **18**, 252–264 (2015).

38. Massé, R. C., Liu, C., Li, Y., Mai, L. & Cao, G. Energy storage through intercalation reactions: electrodes for rechargeable batteries. *National Science Review* nww093 (2016) doi:10.1093/nsr/nww093.

39. Mizushima, K., Jones, P. C., Wiseman, P. J. & Goodenough, J. B. LixCoO2 (0<x<-1): A new cathode material for batteries of high energy density. *Materials Research Bulletin* **15**, 783–789 (1980).

40. Thackeray, M. M. M., David, W. I. F. I. F., Bruce, P. G. P. G. & Goodenough, J. B. J. B. Lithium insertion into manganese spinels. *Materials Research Bulletin* **18**, 461–472 (1983).

41. Padhi, A. K. Phospho-olivines as Positive-Electrode Materials for Rechargeable Lithium Batteries. *Journal of The Electrochemical Society* **144**, 1188 (1997).

42. Ohzuku, T. & Makimura, Y. Layered lithium insertion material of LiCo1/3Ni1/3Mn1/3O2 for lithium-ion batteries. *Chemistry Letters* **30**, 642–643 (2001).

43. Albrecht, S. *et al.* Electrochemical and thermal behavior of aluminum- and magnesium-doped spherical lithium nickel cobalt mixed oxides Li1−x(Ni1−y−zCoyMz)O2 (M = Al, Mg). *Journal of Power Sources* **119–121**, 178–183 (2003).

44. Yazami, R. & Touzain, P. A reversible graphite-lithium negative electrode for electrochemical generators. *Journal of Power Sources* **9**, 365–371 (1983).

45. Ferg, E., Gummow, R. J., Dekock, A. & Thackeray, M. M. Spinel Anodes for Lithium-Ion Batteries. *Journal of The Electrochemical Society* **141**, L147 (1994).

46. Thackeray, M. M., Wolverton, C. & Isaacs, E. D. Electrical energy storage for transportation - Approaching the limits of, and going beyond, lithium-ion batteries. *Energy and Environmental Science* **5**, 7854–7863 (2012).

47. Lima, P. CATL achieves 304 Wh/kg in new battery cells. *PushEVs.com* https://pushevs.com/2019/03/30/catl-achieves-304-wh-kg-in-new-battery-cells/ (2019).

48. Muldoon, J., Bucur, C. B. & Gregory, T. Quest for Nonaqueous Multivalent Secondary Batteries: Magnesium and Beyond. *Chemical Reviews* **114**, 11683–11720 (2014).

49. Wang, Y. *et al.* Emerging non-lithium ion batteries. *Energy Storage Materials* **4**, 103–129 (2016).

50. Massé, R. C., Uchaker, E. & Cao, G. Beyond Li-ion: electrode materials for sodium- and magnesium-ion batteries. *Science China Materials* **58**, 715–766 (2015).

51. Slater, M. D., Kim, D., Lee, E. & Johnson, C. S. Sodium-Ion Batteries. *Advanced Functional Materials* **23**, 947–958 (2013).

52. Gregory, T. D., Hoffman, R. J. & Winterton, R. C. Nonaqueous Electrochemistry of Magnesium. *Journal of The Electrochemical Society* **137**, 775–780 (1990).

53. Aurbach, D. *et al.* Prototype systems for rechargeable magnesium batteries. *Nature* **407**, 724–727 (2000).

54. Aurbach, D. *et al.* Progress in Rechargeable Magnesium Battery Technology. *Advanced Materials* **19**, 4260–4267 (2007).

55. Yoo, H. D. *et al.* Mg rechargeable batteries: an on-going challenge. *Energy & Environmental Science* **6**, 2265–2279 (2013).

56. Aurbach, D., Schechter, A., Moshkovich, M. & Cohen, Y. On the Mechanisms of Reversible Magnesium Deposition Processes. *Journal of The Electrochemical Society* **148**, A1004 (2001).

57. Matsui, M. Study on electrochemically deposited Mg metal. *Journal of Power Sources* **196**, 7048–7055 (2011).

58. Ling, C., Banerjee, D. & Matsui, M. Study of the electrochemical deposition of Mg in the atomic level: Why it prefers the non-dendritic morphology. *Electrochimica Acta* **76**, 270–274 (2012).

59. Davidson, R. *et al.* Formation of Magnesium Dendrites during Electrodeposition. *ACS Energy Letters* **4**, 375–376 (2019).

60. Jeff S. Bartlett. GM Announces Fix for Chevrolet Bolt EVs to Address Fire Risk. *Consumer Reports* https://www.consumerreports.org/car-recalls-defects/chevrolet-bolt-recalled-again-due-to-fire-concerns-a3566085147/ (2021).

61. Ward, L. *et al.* Principles of the Battery Data Genome. (2021).

62. Lu, Z., Schechter, A., Moshkovich, M. & Aurbach, D. On the electrochemical behavior of magnesium electrodes in polar aprotic electrolyte solutions. *Journal of Electroanalytical Chemistry* **466**, 203–217 (1999).

63. Shterenberg, I., Salama, M., Gofer, Y. & Aurbach, D. Hexafluorophosphate-based Solutions for Mg Batteries and the Importance of Chlorides. (2017) doi:10.1021/acs.langmuir.7b01609.

64. Cheng, Y. *et al.* Highly Active Electrolytes for Rechargeable Mg Batteries Based on [Mg2(μ-Cl)2]2+ Cation Complex in Dimethoxyethane. *Phys. Chem. Chem. Phys.* **17**, 13307–13314 (2015).

65. Kim, H. S. *et al.* Structure and compatibility of a magnesium electrolyte with a sulphur cathode. *Nature communications* **2**, 427 (2011).

66. Liebenow, C., Yang, Z. & Lobitz, P. The electrodeposition of magnesium using solutions of organomagnesium halides, amidomagnesium halides and magnesium organoborates. *Electrochemistry Communications* **2**, 641–645 (2000).

67. Aurbach, D. *et al.* Electrolyte Solutions for Rechargeable Magnesium Batteries Based on Organomagnesium Chloroaluminate Complexes. *Journal of The Electrochemical Society* **149**, A115–A121 (2002).

68. Gofer, Y. *et al.* Improved Electrolyte Solutions for Rechargeable Magnesium Batteries. *Electrochemical and Solid-State Letters* **9**, A257–A260 (2006).

69. Pour, N., Gofer, Y., Major, D. T. & Aurbach, D. Structural analysis of electrolyte solutions for rechargeable Mg batteries by stereoscopic means and DFT calculations. *Journal of the American Chemical Society* **133**, 6270–6278 (2011).

70. Bucur, C. B., Gregory, T. & Muldoon, J. Why Grignard's Century Old Nobel Prize Should Spark Your Curiosity. in 611–635 (2015). doi:10.1007/978-3-319-15458-9_22.

71. Muldoon, J., Bucur, C. B. & Gregory, T. Fervent Hype behind Magnesium Batteries: An Open Call to Synthetic Chemists - Electrolytes and Cathodes Needed. *Angewandte Chemie International Edition* (2017) doi:10.1002/anie.201700673.

72. Tutusaus, O. *et al.* An Efficient Halogen-Free Electrolyte for Use in Rechargeable Magnesium Batteries. *Angewandte Chemie International Edition* **201412202**, n/a-n/a (2015).

73. Nelson, E. G., Kampf, J. W. & Bartlett, B. M. Enhanced oxidative stability of non-Grignard magnesium electrolytes through ligand modification. *Chemical communications (Cambridge, England)* **50**, 5193–5 (2014).

74. Esbenshade, J. L. *et al.* Improving Electrodeposition of Mg through an Open Circuit Potential Hold. *The Journal of Physical Chemistry C* **119**, 23366–23372 (2015).

75. See, K. A. *et al.* The Interplay of Al and Mg Speciation in Advanced Mg Battery Electrolyte Solutions. *Journal of the American Chemical Society* **138**, 328–337 (2016).

76. Tutusaus, O., Mohtadi, R., Singh, N., Arthur, T. S. & Mizuno, F. Study of Electrochemical Phenomena Observed at the Mg Metal/Electrolyte Interface. *ACS Energy Letters* 224–229 (2016) doi:10.1021/acsenergylett.6b00549.

77. Son, S. B. *et al.* An artificial interphase enables reversible magnesium chemistry in carbonate electrolytes. *Nature Chemistry* **10**, 532–539 (2018).

78. Li, X. *et al.* Reducing Mg Anode Overpotential via Ion Conductive Surface Layer Formation by Iodine Additive. *Advanced Energy Materials* **1701728**, 1701728 (2017).

79. Attias, R., Salama, M., Hirsch, B., Goffer, Y. & Aurbach, D. Anode-Electrolyte Interfaces in Secondary Magnesium Batteries. *Joule* (2019) doi:10.1016/j.joule.2018.10.028.

80. Gofer, Y., Turgeman, R., Cohen, H. & Aurbach, D. XPS investigation of surface chemistry of magnesium electrodes in contact with organic solutions of organochloroaluminate complex salts. *Langmuir* **19**, 2344–2348 (2003).

81. Canepa, P. *et al.* Understanding the Initial Stages of Reversible Mg Deposition and Stripping in Inorganic Non-Aqueous Electrolytes. *Chemistry of Materials* 150408142223009 (2015) doi:10.1021/acs.chemmater.5b00389.

82. Connell, J. G. *et al.* Tuning the Reversibility of Mg Anodes via Controlled Surface Passivation by H_2O/Cl^- in Organic Electrolytes. *Chemistry of Materials* **28**, acs.chemmater.6b03227 (2016).

83. Pan, B. *et al.* MgCl $_2$: The Key Ingredient to Improve Chloride Containing Electrolytes for Rechargeable Magnesium-Ion Batteries. *Journal of The Electrochemical Society* **163**, A1672–A1677 (2016).

84. Sa, N. *et al.* Role of Chloride for a Simple, Non-Grignard Mg Electrolyte in Ether-Based Solvents. *ACS Applied Materials and Interfaces* **8**, 16002–16008 (2016).

85. Shterenberg, I. *et al.* Evaluation of (CF 3 SO 2) 2 N − (TFSI) Based Electrolyte Solutions for Mg Batteries. *Journal of The Electrochemical Society* **162**, A7118–A7128 (2015).

86. Muldoon, J. *et al.* Corrosion of magnesium electrolytes: chlorides – the culprit. *Energy & Environmental Science* **6**, 482 (2013).

87. Lv, D. *et al.* A Scientific Study of Current Collectors for Mg Batteries in Mg(AlCl2EtBu)2/THF Electrolyte. *Journal of the Electrochemical Society* **160**, A351–A355 (2012).

88. Tutusaus, O. & Mohtadi, R. Paving the Way towards Highly Stable and Practical Electrolytes for Rechargeable Magnesium Batteries. *ChemElectroChem* **2**, 51–57 (2015).

89. Muldoon, J. *et al.* Electrolyte roadblocks to a magnesium rechargeable battery. *Energy & Environmental Science* **5**, 5941 (2012).

90. Mizrahi, O. *et al.* Electrolyte Solutions with a Wide Electrochemical Window for Rechargeable Magnesium Batteries. *Journal of The Electrochemical Society* **155**, A103–A109 (2008).

91. Guo, Y. *et al.* Boron-based electrolyte solutions with wide electrochemical windows for rechargeable magnesium batteries. *Energy & Environmental Science* **5**, 9100 (2012).

92. Nelson, E. G., Brody, S. I., Kampf, J. W. & Bartlett, B. M. A magnesium tetraphenylaluminate battery electrolyte exhibits a wide electrochemical potential window and reduces stainless steel corrosion. *J. Mater. Chem. A* **2**, 18194–18198 (2014).

93. Bucur, C. B., Gregory, T., Oliver, A. G. & Muldoon, J. Confession of a Magnesium Battery. *The Journal of Physical Chemistry Letters* **6**, 3578–3591 (2015).

94. Li, B. *et al.* Kinetic surface control for improved magnesium-electrolyte interfaces for magnesium ion batteries. *Energy Storage Materials* (2019) doi:10.1016/j.ensm.2019.06.035.

95. Lv, R., Guan, X., Zhang, J., Xia, Y. & Luo, J. Enabling Mg Metal Anodes Rechargeable in Conventional Electrolytes by Fast Ionic Transport Interphase. *National Science Review* (2019) doi:10.1093/nsr/nwz157.

96. Zhang, J. *et al.* Rechargeable Mg metal batteries enabled by a protection layer formed in vivo. *Energy Storage Materials* (2019) doi:10.1016/j.ensm.2019.11.012.

97. Tang, K. *et al.* A Stable Solid Electrolyte Interphase for Magnesium Metal Anode Evolved from a Bulky Anion Lithium Salt. *Advanced Materials* **1904987**, 1–7 (2019).

98. Lee, H., Kim, S. & Park, Y. Enhanced electrochemical properties of fluoride-coated LiCoO2 thin films. *Nanoscale Research Letters* **7**, 16 (2012).

99. Park, K.-S. *et al.* Enhanced Charge-Transfer Kinetics by Anion Surface Modification of $LiFePO_4$. *Chemistry of Materials* **24**, 3212–3218 (2012).

100. Xu, K. & von Cresce, A. Interfacing electrolytes with electrodes in Li ion batteries. *Journal of Materials Chemistry* **21**, 9849 (2011).

101. Li, B., Xu, M., Li, T., Li, W. & Hu, S. Prop-1-ene-1,3-sultone as SEI formation additive in propylene carbonate-based electrolyte for lithium ion batteries. *Electrochemistry Communications* **17**, 92–95 (2012).

102. Li, B. *et al.* A novel electrolyte with the ability to form a solid electrolyte interface on the anode and cathode of a LiMn2O4/graphite battery. *Journal of Materials Chemistry A* **1**, 12954 (2013).

103. Jeong, S. *et al.* Surface film formation on a graphite negative electrode in lithium-ion batteries: atomic force microscopy study on the effects of film-forming additives in propylene carbonate. *Langmuir* **27**, 8281–8286 (2001).

104. Aurbach, D. *et al.* On the use of vinylene carbonate (VC) as an additive to electrolyte solutions for Li-ion batteries. *Electrochimica Acta* **47**, 1423–1439 (2002).

105. Ryou, M. H. *et al.* Effect of fluoroethylene carbonate on high temperature capacity retention of LiMn2O4/graphite Li-ion cells. *Electrochimica Acta* **55**, 2073–2077 (2010).

106. Li, B. *et al.* Improving high voltage stability of lithium cobalt oxide/graphite battery via forming protective films simultaneously on anode and cathode by using electrolyte additive. *Electrochimica Acta* **141**, 263–270 (2014).

107. Xu, M., Li, W. & Lucht, B. L. Effect of propane sultone on elevated temperature performance of anode and cathode materials in lithium-ion batteries. *Journal of Power Sources* **193**, 804–809 (2009).

108. Li, B. *et al.* Properties of solid electrolyte interphase formed by prop-1-ene-1,3-sultone on graphite anode of Li-ion batteries. *Electrochimica Acta* **105**, 1–6 (2013).

109. Zhao, J. *et al.* Surface Fluorination of Reactive Battery Anode Materials for Enhanced Stability. *Journal of the American Chemical Society* **139**, 11550–11558 (2017).

110. Lang, J. *et al.* One-pot solution coating of high quality LiF layer to stabilize Li metal anode. *Energy Storage Materials* **16**, 85–90 (2019).

111. Suo, L. *et al.* "Water-in-salt" electrolyte enables high-voltage aqueous lithium-ion chemistries. *Science* **350**, 938–943 (2015).

112. Zhang, Q. *et al.* Synergetic Effects of Inorganic Components in Solid Electrolyte Interphase on High Cycle Efficiency of Lithium Ion Batteries. *Nano Letters* **16**, 2011–2016 (2016).

113. Bai, Y. *et al.* Performance improvement of LiCoO2 by MgF2 surface modification and mechanism exploration. *Electrochimica Acta* **134**, 347–354 (2014).

114. Chen, T., Ceder, G., Gautam, G. S. & Canepa, P. Evaluation of Mg compounds as coating materials in Mg batteries. *Frontiers in Chemistry* **7**, (2019).

115. Chen, T., Sai Gautam, G. & Canepa, P. Ionic Transport in Potential Coating Materials for Mg Batteries. *Chemistry of Materials* **31**, 8087–8099 (2019).

116. Matsui, M., Kuwata, H., Mori, D., Imanishi, N. & Mizuhata, M. Destabilized passivation layer on magnesium-based intermetallics as potential anode active materials for magnesium ion batteries. *Frontiers in Chemistry* **7**, (2019).

117. Lee, H. J. & Park, Y. J. Interface characterization of MgF2-coated LiCoO2 thin films. *Solid State Ionics* **230**, 86–91 (2013).

118. Cho, Y., Eom, J. & Cho, J. High Performance LiCoO[sub 2] Cathode Materials at 60°C for Lithium Secondary Batteries Prepared by the Facile Nanoscale Dry-Coating Method. *Journal of The Electrochemical Society* **157**, A617 (2010).

119. Liu, X. Y. *et al.* Novel bismuth nanotube arrays synthesized by solvothermal method. *Chemical Physics Letters* **374**, 348–352 (2003).

120. Nandiyanto, A. B. D., Iskandar, F., Ogi, T. & Okuyama, K. Nanometer to submicrometer magnesium fluoride particles with controllable morphology. *Langmuir* **26**, 12260–12266 (2010).

121. Arthur, T. S., Singh, N. & Matsui, M. Electrodeposited Bi, Sb and Bi 1-xSb x alloys as anodes for Mg-ion batteries. *Electrochemistry Communications* **16**, 103–105 (2012).

122. Shao, Y. *et al.* Highly reversible Mg insertion in nanostructured Bi for Mg ion batteries. *Nano Letters* **14**, 255–260 (2014).

123. Huie, M. M., Bock, D. C., Takeuchi, E. S., Marschilok, A. C. & Takeuchi, K. J. Cathode materials for magnesium and magnesium-ion based batteries. *Coordination Chemistry Reviews* **287**, 15–27 (2015).

124. Murgia, F., Stievano, L., Monconduit, L. & Berthelot, R. Insight into the electrochemical behavior of micrometric Bi and Mg3Bi2 as high performance negative electrodes for Mg batteries. *Journal of Materials Chemistry A* **3**, 16478–16485 (2015).

125. Tchitchekova, D. S. *et al.* On the Reliability of Half-Cell Tests for Monovalent (Li+, Na+) and Divalent (Mg2+, Ca2+) Cation Based Batteries. *Journal of The Electrochemical Society* **164**, A1384–A1392 (2017).

126. Orazem, M. E. & Tribollet, B. *Electrochemical Impedance Spectroscopy*. *Analysis* vol. 48 (2008).

127. Keyzer, E. N. *et al.* Mg(PF6)2-Based Electrolyte Systems: Understanding Electrolyte-Electrode Interactions for the Development of Mg-Ion Batteries. *Journal of the American Chemical Society* **138**, 8682–8685 (2016).

128. Børresen, B., Haarberg, G. M. & Tunold, R. Electrodeposition of magnesium from halide melts—charge transfer and diffusion kinetics. *Electrochimica Acta* **42**, 1613–1622 (1997).

129. Zhang, Z. *et al.* Novel Design Concepts of Efficient Mg-Ion Electrolytes toward High-Performance Magnesium-Selenium and Magnesium-Sulfur Batteries. *Advanced Energy Materials* **201602055**, 1–10 (2017).

130. Levi, E., Gofer, Y. & Aurbach, D. On the Way to Rechargeable Mg Batteries: The Challenge of New Cathode Materials †. *Chemistry of Materials* **22**, 860–868 (2010).

131. Amatucci, G. G. *et al.* Investigation of Yttrium and Polyvalent Ion Intercalation into Nanocrystalline Vanadium Oxide. *Journal of The Electrochemical Society* **148**, A940 (2001).

132. Novák, P., Novák, P. & Desilvestro, J. Electrochemical Insertion of Magnesium in Metal Oxides and Sulfides from Aprotic Electrolytes. *Journal of The Electrochemical Society* **140**, 140 (1993).

133. Wan, L. F., Perdue, B. R., Apblett, C. A. & Prendergast, D. Mg Desolvation and Intercalation Mechanism at the Mo 6 S 8 Chevrel Phase Surface. *Chemistry of Materials* **27**, 5932–5940 (2015).

134. Nam, K. W. *et al.* The High Performance of Crystal Water Containing Manganese Birnessite Cathodes for Magnesium Batteries. *Nano Letters* **15**, 4071–4079 (2015).

135. Aurbach, D., Weissman, I., Gofer, Y. & Levi, E. Nonaqueous magnesium electrochemistry and its application in secondary batteries. *Chemical Record* **3**, 61–73 (2003).

136. Levi, E., Gershinsky, G., Aurbach, D., Isnard, O. & Ceder, G. New insight on the unusually high ionic mobility in chevrel phases. *Chemistry of Materials* **21**, 1390–1399 (2009).

137. Levi, E., Levi, M. D., Chasid, O. & Aurbach, D. A review on the problems of the solid state ions diffusion in cathodes for rechargeable Mg batteries. *Journal of Electroceramics* **22**, 13–19 (2009).

138. Aurbach, D. *et al.* A short review on the comparison between Li battery systems and rechargeable magnesium battery technology. *Journal of Power Sources* **97–98**, 28–32 (2001).

139. Song, J., Sahadeo, E., Noked, M. & Lee, S. B. Mapping the Challenges of Magnesium Battery. *The Journal of Physical Chemistry Letters* **7**, 1736–1749 (2016).

140. Tran, T. T., Lamanna, W. M. & Obrovac, M. N. Evaluation of Mg[N(SO2CF3)2]2/Acetonitrile Electrolyte for Use in Mg-Ion Cells. *Journal of the Electrochemical Society* **159**, A2005–A2009 (2012).

141. Chen, Q., Nuli, Y. N., Yang, J., Kailibinuer, K. & Wang, J. L. Effects of current collectors on the electrochemical performance of electrolytes for rechargeable magnesium batteries. *Wuli Huaxue Xuebao/ Acta Physico - Chimica Sinica* **28**, 2625–2631 (2012).

142. Cheng, Y. *et al.* Electrochemically stable cathode current collectors for rechargeable magnesium batteries. *Journal of Materials Chemistry A* **2**, 2473 (2014).

143. Wall, C., Zhao-Karger, Z. & Fichtner, M. Corrosion Resistance of Current Collector Materials in Bisamide Based Electrolyte for Magnesium Batteries. *ECS Electrochemistry Letters* **4**, C8–C10 (2014).

144. Yagi, S., Tanaka, A., Ichikawa, Y., Ichitsubo, T. & Matsubara, E. Electrochemical Stability of Magnesium Battery Current Collectors in a Grignard Reagent-Based Electrolyte. *JOURNAL OF THE ELECTROCHEMICAL SOCIETY* **160**, C83–C88 (2013).

145. Yagi, S., Tanaka, A., Ichitsubo, T. & Matsubara, E. Electrochemical Stability of Metal Electrodes for Reversible Magnesium Deposition/Dissolution in Tetrahydrofuran Dissolving Ethylmagnesium Chloride. *ECS Electrochemistry Letters* vol. 1 D11–D14 (2012).

146. Okoshi, M., Yamada, Y., Yamada, A. & Nakai, H. Theoretical Analysis on De-Solvation of Lithium, Sodium, and Magnesium Cations to Organic Electrolyte Solvents. *Journal of the Electrochemical Society* **160**, A2160–A2165 (2013).

147. Levi, M. D. *et al.* Kinetic and Thermodynamic Studies of Mg2 + and Li + Ion Insertion into the Mo6 S 8 Chevrel Phase. *Journal of The Electrochemical Society* **151**, A1044–A1051 (2004).

148. Su, S. *et al.* A novel rechargeable battery with a magnesium anode, a titanium dioxide cathode, and a magnesium borohydride/tetraglyme electrolyte. *Chem. Commun.* **51**, 2641–2644 (2015).

149. Ling, C., Zhang, R., Arthur, T. S. & Mizuno, F. How General is the Conversion Reaction in Mg Battery Cathode: A Case Study of the Magnesiation of α-MnO 2. *Chemistry of Materials* **27**, 5799–5807 (2015).

150. Zhang, R. & Ling, C. Unveil the Chemistry of Olivine FePO 4 as Magnesium Battery Cathode. *ACS Applied Materials & Interfaces* **8**, 18018–18026 (2016).

151. Liang, Y. *et al.* Rechargeable Mg batteries with graphene-like MoS 2 cathode and ultrasmall Mg nanoparticle anode. *Advanced Materials* **23**, 640–643 (2011).

152. Ichitsubo, T., Adachi, T., Yagi, S. & Doi, T. Potential positive electrodes for high-voltage magnesium-ion batteries. *Journal of Materials Chemistry* **21**, 11764 (2011).

153. Sano, H., Senoh, H., Yao, M., Sakaebe, H. & Kiyobayashi, T. Mg2+ Storage in Organic Positive-electrode Active Material Based on 2,5-Dimethoxy-1,4-benzoquinone. *Chemistry Letters* **41**, 1594–1596 (2012).

154. Sasaki, I., Murase, K., Ichii, T., Uchimoto, Y. & Sugimura, H. Anodic Dissolution Behavior of Magnesium in Hydrophobic Ionic Liquids. *ECS Transactions* **33**, 65–70 (2011).

155. Kratochvil, Byron., Lorah, Esther. & Garber, Carl. Silver-silver nitrate couple as reference electrode in acetonitrile. *Analytical Chemistry* **41**, 1793–1796 (1969).

156. Snook, G. a., Best, a. S., Pandolfo, a. G. & Hollenkamp, a. F. Evaluation of a Ag|Ag+ reference electrode for use in room temperature ionic liquids. *Electrochemistry Communications* **8**, 1405–1411 (2006).

157. Ruch, P. W., Cericola, D., Hahn, M., Kötz, R. & Wokaun, A. On the use of activated carbon as a quasi-reference electrode in non-aqueous electrolyte solutions. *Journal of Electroanalytical Chemistry* **636**, 128–131 (2009).

158. Gershinsky, G., Yoo, H. D., Gofer, Y. & Aurbach, D. Electrochemical and spectroscopic analysis of Mg2+ intercalation into thin film electrodes of layered oxides: V2O5 and MoO3. *Langmuir* **29**, 10964–10972 (2013).

159. Song, J. *et al.* Activation of a MnO2 cathode by water-stimulated Mg2+ insertion for a magnesium ion battery. *Phys. Chem. Chem. Phys.* **17**, 5256–5264 (2015).

160. Chen, Y. Examination of the Corrosion Behavior of Aluminum Current Collectors in Lithium/Polymer Batteries. *Journal of The Electrochemical Society* **146**, 1310 (1999).

161. Myung, S.-T., Hitoshi, Y. & Sun, Y.-K. Electrochemical behavior and passivation of current collectors in lithium-ion batteries. *Journal of Materials Chemistry* **21**, 9891 (2011).

162. Ha, S. Y. *et al.* Magnesium(II) bis(trifluoromethane sulfonyl) imide-based electrolytes with wide electrochemical windows for rechargeable magnesium batteries. *ACS Applied Materials and Interfaces* **6**, 4063–4073 (2014).

163. Lewandowski, A., Waligora, L. & Galinski, M. Ferrocene as a reference redox couple for aprotic ionic liquids. *Electroanalysis* **21**, 2221–2227 (2009).

164. Gagné, R. R., Koval, C. A. & Lisensky, G. C. Ferrocene as an Internal Standard for Electrochemical Measurements. *Inorganic Chemistry* **19**, 2854–2855 (1980).

165. Wang, Y., Shang, H., Chou, T. & Cao, G. Effects of thermal annealing on the Li(+) intercalation properties of V(2)O(5) x nH(2)O xerogel films. *The journal of physical chemistry. B* **109**, 11361–11366 (2005).

166. Lipson, A. L. *et al.* Practical Stability Limits of Magnesium Electrolytes. *Journal of The Electrochemical Society* **163**, A2253–A2257 (2016).

167. Livage, J. Vanadium Pentoxide Gels. *Chemistry of Materials* vol. 3 578–593 (1991).

168. Dugas, R., Forero-Saboya, J. D. & Ponrouch, A. Methods and Protocols for Reliable Electrochemical Testing in Post-Li Batteries (Na, K, Mg, and Ca). *Chemistry of Materials* acs.chemmater.9b02776 (2019) doi:10.1021/acs.chemmater.9b02776.

169. Sun, X., Duffort, V., Mehdi, B. L., Browning, N. D. & Nazar, L. F. Investigation of the Mechanism of Mg Insertion in Birnessite in Non-aqueous and Aqueous Rechargeable Mg-ion Batteries. *Chemistry of Materials* acs.chemmater.5b03983 (2015) doi:10.1021/acs.chemmater.5b03983.

170. Uchaker, E. *et al.* Enhanced intercalation dynamics and stability of engineered micro/nano-structured electrode materials: Vanadium oxide mesocrystals. *Small* **9**, 3880–3886 (2013).

171. Uchaker, E. & Cao, G. The Role of Intentionally Introduced Defects on Electrode Materials for Alkali-Ion Batteries. *Chemistry - An Asian Journal* **10**, 1608–1617 (2015).

172. Wan, L. F., Incorvati, J. T., Poeppelmeier, K. R. & Prendergast, D. Building a fast lane for Mg diffusion in α-MoO3 by fluorine doping. *Chemistry of Materials* **28**, 6900–6908 (2016).

173. Incorvati, J. T. *et al.* Reversible Magnesium Intercalation into a Layered Oxyfluoride Cathode. *Chem. Mater.* **28**, 1–4 (2015).

174. Gu, Y., Katsura, Y., Yoshino, T., Takagi, H. & Taniguchi, K. Rechargeable magnesium-ion battery based on a TiSe2-cathode with d-p orbital hybridized electronic structure. *Scientific Reports* **5**, 12486 (2015).

175. Taniguchi, K., Gu, Y., Katsura, Y., Yoshino, T. & Takagi, H. Rechargeable Mg battery cathode TiS3 with d-p orbital hybridized electronic structures. *Applied Physics Express* **9**, 2–6 (2016).

176. Rong, Z. *et al.* Materials Design Rules for Multivalent Ion Mobility in Intercalation Structures. *Chemistry of Materials* **27**, 6016–6021 (2015).

177. Blanc, L. E., Sun, X., Shyamsunder, A., Duffort, V. & Nazar, L. F. Direct Nano-Synthesis Methods Notably Benefit Mg-Battery Cathode Performance. **2000029**, 1–8 (2020).

178. Okoshi, M., Yamada, Y., Komaba, S., Yamada, A. & Nakai, H. Theoretical Analysis of Interactions between Potassium Ions and Organic Electrolyte Solvents: A Comparison with Lithium, Sodium, and Magnesium Ions. *Journal of The Electrochemical Society* **164**, A54–A60 (2017).

179. Attias, R., Bublil, S., Salama, M., Goffer, Y. & Aurbach, D. How solution chemistry affects the electrochemical behavior of cathodes for Mg batteries, a classical electroanalytical study. *Electrochimica Acta* **334**, (2020).

180. Wang, L. *et al.* Solvent-Controlled Charge Storage Mechanisms of Spinel Oxide Electrodes in Mg Organohaloaluminate Electrolytes. *Nano Letters* acs.nanolett.7b03978 (2017) doi:10.1021/acs.nanolett.7b03978.

181. Wan, L. F. & Prendergast, D. Ion-Pair Dissociation on α−MoO_3 Surfaces: A Focus on the Electrolyte-Cathode Compatibility Issue in Mg Batteries. *The Journal of Physical Chemistry C* **122**, acs.jpcc.7b09124 (2017).

182. Shneider, A. M. Mental inertia in the biological sciences. *Trends in Biochemical Sciences* **35**, 125–128 (2010).

183. Voltaiq. https://www.voltaiq.com/.

184. Herring, P. *et al.* BEEP: A Python library for Battery Evaluation and Early Prediction. *SoftwareX* **11**, 100506 (2020).

185. Buteau, S. Universal Battery Database. https://github.com/Samuel-Buteau/universal-battery-database.

186. Maehlen, J. P., Abdelhamid, M., Raniseth, A. M. & Ulvestad, A. cellpy. https://cellpy.readthedocs.io/en/latest/.

187. de Angelis, V., Preger, Y. & Chalamala, B. R. *Battery Lifecycle Framework: A Flexible Repository and Visualization Tool for Battery Data from Materials Development to Field Implementation*. www.BatteryArchive.org.

188. Lewis-Douglas, A., Pitt, L. & Howey, D. A. Galvanalyser: A Battery Test Database. (2020).

189. Project Jupyter. https://jupyter.org/.

190. Dubarry, M., Svoboda, V., Hwu, R. & Yann Liaw, B. Incremental Capacity Analysis and Close-to-Equilibrium OCV Measurements to Quantify Capacity Fade in Commercial Rechargeable Lithium Batteries. *Electrochemical and Solid-State Letters* **9**, A454–A457 (2006).

191. van der Walt, S., Colbert, S. C. & Varoquaux, G. The NumPy array: A structure for efficient numerical computation. *Computing in Science and Engineering* **13**, 22–30 (2011).

192. Virtanen, P. *et al.* SciPy 1.0: fundamental algorithms for scientific computing in Python. *Nature Methods 2020 17:3* **17**, 261–272 (2020).

193. Hunter, J. D. Matplotlib: A 2D Graphics Environment. *Computing in Science & Engineering* **9**, 90–95 (2007).

194. Pedregosa, F. *et al.* Scikit-learn: Machine Learning in Python. *Journal of Machine Learning Research* **12**, 2825–2830 (2012).

195. Mckinney, W. pandas: a Foundational Python Library for Data Analysis and Statistics.

196. VanderPlas, J. *et al.* Altair: Interactive Statistical Visualizations for Python. *Journal of Open Source Software* **3**, 1057 (2018).

197. Sulzer, V., Marquis, S. G., Timms, R., Robinson, M. & Chapman, S. J. Python Battery Mathematical Modelling (PyBaMM). *Journal of Open Research Software* **9**, 1–8 (2021).

198. Masse, R. Astrolabe Onboarding Demo. https://www.youtube.com/watch?v=H1aika-ol_0.

199. Berecibar, M., Dubarry, M., Villarreal, I., Omar, N. & Mierlo, J. van. Degradation Mechanisms Detection for HP and HE NMC Cells Based on Incremental Capacity Curves. (2016).

200. Matthieu Dubarry, A. D. and B. Y. L. The Value of Battery Diagnostics and Prognostics. *Journal of Energy and Power Sources* **1**, 242–249 (2014).

201. Severson, K. A. *et al.* Data-driven prediction of battery cycle life before capacity degradation. *Nature Energy* **4**, 383–391 (2019).

202. Dubarry, M., Truchot, C. & Liaw, B. Y. Synthesize battery degradation modes via a diagnostic and prognostic model. *Journal of Power Sources* **219**, 204–216 (2012).

203. Sulzer, V. *et al.* The challenge and opportunity of battery lifetime prediction from field data. *Joule* **5**, 1934–1955 (2021).

204. Aykol, M. *et al.* Perspective—Combining Physics and Machine Learning to Predict Battery Lifetime. *Journal of The Electrochemical Society* **168**, 030525 (2021).

205. Hu, X., Xu, L., Lin, X. & Pecht, M. Battery Lifetime Prognostics. *Joule* **4**, 310–346 (2020).

206. Attia, P. M. *et al.* Closed-loop optimization of fast-charging protocols for batteries with machine learning. *Nature* **578**, 397–402 (2020).

207. Fermín-Cueto, P. *et al.* Identification and machine learning prediction of knee-point and knee-onset in capacity degradation curves of lithium-ion cells. *Energy and AI* **1**, 100006 (2020).

208. Greenbank, S. & Howey, D. A. Automated feature extraction and selection for data-driven models of rapid battery capacity fade and end of life. *IEEE Transactions on Industrial Informatics* (2021) doi:10.1109/TII.2021.3106593.

209. Chahbaz, A., Meishner, F., Li, W., Ünlübayir, C. & Uwe Sauer, D. Non-invasive identification of calendar and cyclic ageing mechanisms for lithium-titanate-oxide batteries. *Energy Storage Materials* **42**, 794–805 (2021).

210. Preger, Y. *et al.* Degradation of Commercial Lithium-Ion Cells as a Function of Chemistry and Cycling Conditions. *Journal of The Electrochemical Society* **167**, 120532 (2020).

211. Lecun, Y. *et al.* Handwritten digit recognition with a back-propagation network. *Advances in Neural Information Processing Systems (NIPS 1989)* (1990) doi:10.2/JQUERY.MIN.JS.

212. Lecun, Y., Bottou, L., Bengio, Y. & Haffner, P. Gradient-based learning applied to document recognition. *Proceedings of the IEEE* **86**, 2278–2324 (1998).

213. Rawat, W. & Wang, Z. Deep Convolutional Neural Networks for Image Classification: A Comprehensive Review. *Neural Computation* **29**, 2352–2449 (2017).

214. Attia, P. M., Severson, K. A. & Witmer, J. D. Statistical learning for accurate and interpretable battery lifetime prediction. *Journal of The Electrochemical Society* **168**, 090547 (2021).

215. dos Reis, G., Strange, C., Yadav, M. & Li, S. Lithium-ion battery data and where to find it. *Energy and AI* **5**, 100081 (2021).

216. Roman, D., Saxena, S., Robu, V., Pecht, M. & Flynn, D. Machine learning pipeline for battery state of health estimation. (2021).

217. Gramfort, A. & Pedregosa, F. Outlier detection with Local Outlier Factor (LOF). Available at: https://scikit-learn.org/stable/auto_examples/neighbors/plot_lof_outlier_detection.html.

218. Pedregosa, F. *et al.* Scikit-learn: Machine Learning in Python. *J. Mach. Learn. Res.* **12**, 2825–2830 (2012).

219. Virtanen, P. *et al.* SciPy 1.0: fundamental algorithms for scientific computing in Python. *Nat. Methods 2020 173* **17**, 261–272 (2020).

220. Integration and ODEs (scipy.integrate). Available at: https://docs.scipy.org/doc/scipy-0.10.1/reference/generated/scipy.integrate.trapz.html.

221. United States Advanced Battery Consortium. Electric Vehicle Battery Test Procedures Manual. http://www.uscar.org/guest/article_view.php?articles_id=74.

Appendix

Chapter 6.

For reference, the *Projects* table referenced in Chapter 6.2.2. has the following columns:

Id
ActiveMaterialFraction
Area
Channel
Comments
CreatedAt
Error
Failed
FileName
FileSize
InternalFileName
IsAveragePlot
IsPartialGathering
IsReady
JobId
Mass
Name
StitchedFrom
StitchedFromNames
Tag
TestName
TestType
TheoreticalCapacity
TraceId
UpdatedAt
UserId
NumCycles
TestDate
PAMMass
NAMMass
IsRealTime
ProcessDate
IsProcessing
ProcessingMessage
DataPointStartDate
Shard_Id
Organization_OrganizationId
ExtraDataNameJSON
ErrorDetailed

DataPointExtraData: Some formats contain auxiliary data. An example is VARx, FLGx columns in Maccor. This is where we store that data. There could be multiple aux data values for each data point (i.e. VARx1, VARx2, etc.). In order to save on database space, we only store aux data on the data point in which the value has changed compared to the previous value for this aux data. Columns are:

Id
DataPoint_Id
Name
Value

Columns for the *DataPoints* table include:

Id
Capacity
Current
CycleIndex
CycleStep
Energy
Index
Power
ProjectId
Temperature
Time
Voltage
StepIndex
WallTime
Resistance

Columns for the *Cycles* table include:

ProjectId
Index
ChargeCapacity
ChargeCapacityRetention
ChargeEnergy
DischargeCapacity
DischargeCapacityRetention
DischargeEndCurrent
DischargeEndVoltage
DischargeEnergy
DischargePower
DischargeResistance
EndCurrent
EndRestVoltage

EndVoltage
FirstPointIndex
MidVoltage
PointCount
Power
ResistanceOhms
StartChargeVoltage
StartCurrent
StartDischargeCurrent
StartDischargeVoltage
StatisticMetaData
Temperature
MinimumPower
MaximumPower
MinimumDischargePower
MaximumDischargePower
AverageDischargePower
AveragePower

An additional note on StatisticMetaData: This is JSON text that contains some additional data. There are a number of columns in this JSON. They are:

ChargeCapacityAverage
ChargeCapacityFirst
ChargeCapacityLast
ChargeCapacityMax
ChargeCapacityMin
ChargeCapacityRetentionStdDev
ChargeCapacityStdDev
ChargeCapacityStdError
ChargeCapacityVariance
ChargeEnergyStdDev
ChargeVoltageAverage
ChargeVoltageMax
ChargeVoltageMin
ChargeVoltageStdDev
ChargeVoltageStdError
ChargeVoltageVariance
CoulombicEfficiencyAverage
CoulombicEfficiencyStdDev
DischargeCapacityAverage
DischargeCapacityFirst
DischargeCapacityLast
DischargeCapacityMax
DischargeCapacityMin
DischargeCapacityRetentionStdDev

DischargeCapacityStdDev
DischargeCapacityStdError
DischargeCapacityVariance
DischargeEndCurrentStdDev
DischargeEndVoltageStdDev
DischargeEnergyStdDev
DischargePowerStdDev
DischargeResistanceStdDev
DischargeVoltageAverage
DischargeVoltageMax
DischargeVoltageMin
DischargeVoltageStdDev
DischargeVoltageStdError
DischargeVoltageVariance
EndCurrentStdDev
EndVoltageStdDev
MidVoltageStdDev
PowerStdDev
ResistanceOhmsStdDev
VoltageAverage
VoltageFirst
VoltageLast
VoltageMax
VoltageMin
VoltageStdDev
VoltageStdError
VoltageVariance

Chapter 8.

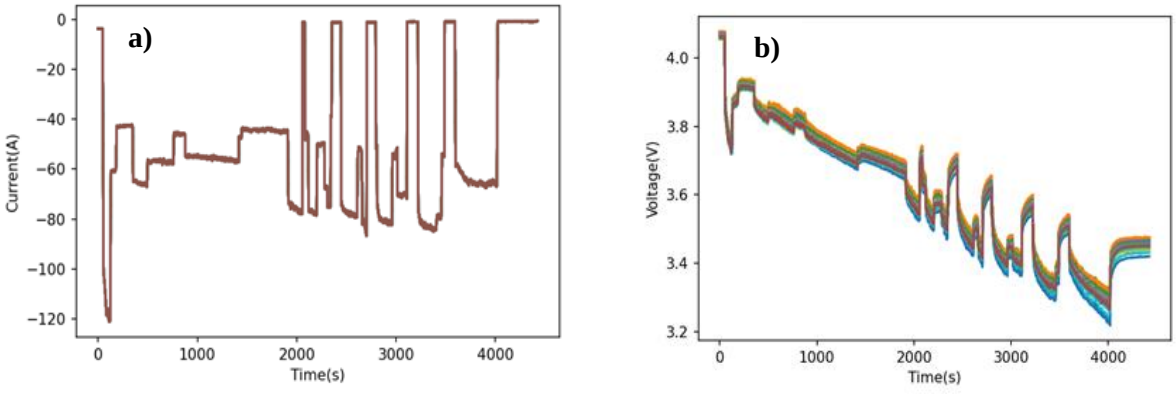

Figure S1. a) Current profile of the flight test. b) Representative voltage profile of all 196 cell blocks in a pack under the load shown in a).

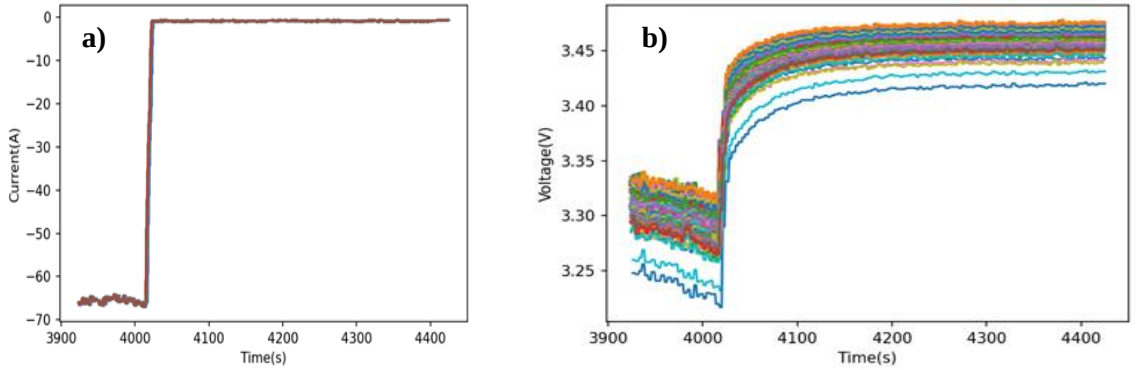

Figure S2. Example end-of-test data a) current and b) voltage for a battery pack.

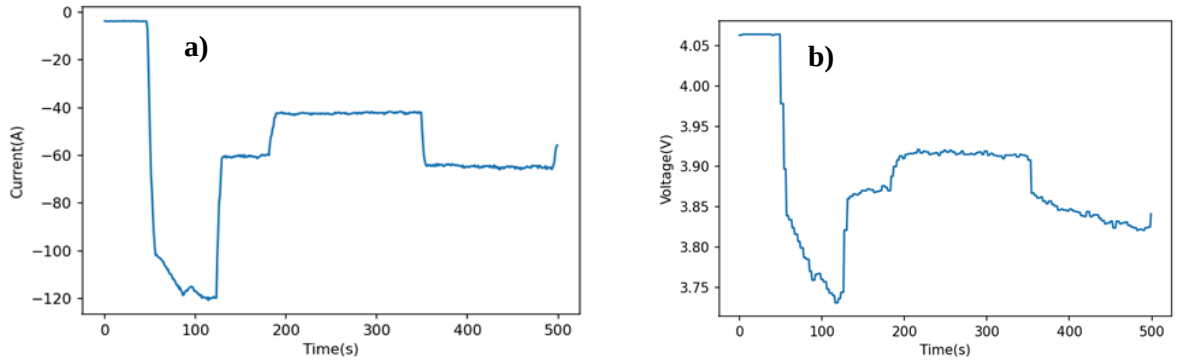

Figure S3. Example initial test data from the first 500 seconds for both a) current and b) voltage.

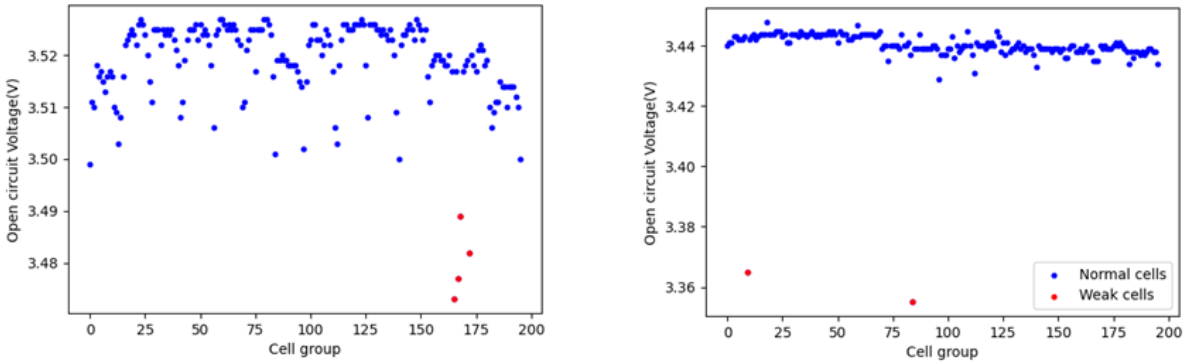

Figure S4. Two examples of flight test data where the weakest cell blocks (red) are visually apparent.

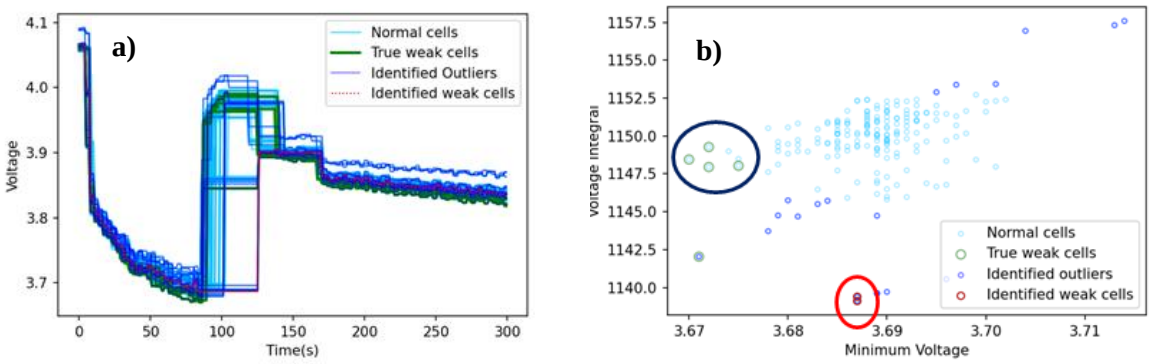

Figure S5. a) Offsets in data acquisition were present in some datasets. b) This in turn propagated through the algorithm to misidentify weak cell blocks.

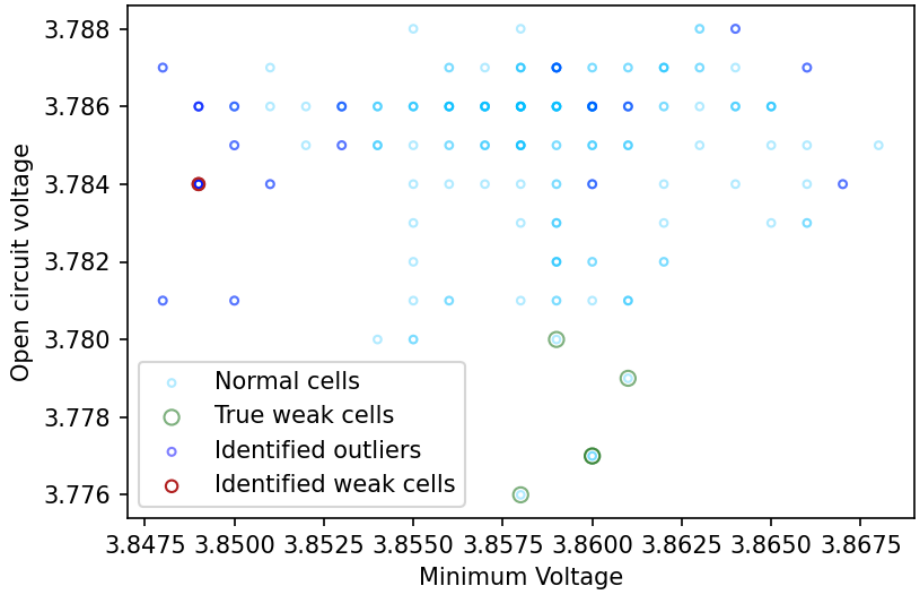

Figure S6. One "failure" mode of the weak cell block identification algorithm arose where the ensemble of battery cell blocks was composed of cells whose OCV fell within a tight voltage range.